I. The Heterogeneities at the Core-Mantle and Inner-Core Boundaries from PKP Phases

II. The Static and Dynamic Behavior of Silica at High Pressures

Thesis by

Sheng-Nian Luo

In Partial Fulfillment of the Requirements
for the Degree of
Doctor of Philosophy

California Institute of Technology
Pasadena, California

2003
(Submitted June 10, 2003)

Acknowledgements

It was my mathematics teacher in junior high school, Mr. Changjin Jiang, who first led me to appreciate the mesmerizing beauty of mathematics, and of science in general later on. I have been lucky to be educated at both USTC (University of Science and Technology of China) and Caltech, for which I am most grateful.

It is definitely an intellectually pleasant experience here at the Seismological Laboratory and Caltech. My research advisors, T. J. Ahrens and D. V. Helmberger, have demonstrated great professionalism and scholarship as well as sense of humor, kindness and patience. They have been totally supportive by letting me pursuing new ideas freely. I am also grateful to P. D. Asimow, in particular for challenging me critically on one hand but being resonant with me on the other hand during our research. R. Clayton as my academic advisor has supplied kind help in academic affairs. I have profited from other Caltech professors, among whom are D. L. Anderson, W. A. Goddard III (Chemistry), H. Kanamori, G. Ravichandran (Aeronautics), G. R. Rossman and D. Stevenson. Besides the wonderful research experience, I have enjoyed being present in the classes of P. Goldreich (Solar System), W. L. Johnson (States of Matter), A. Rosakis (Continuum Mechanics) and W. A. Goddard III (Quantum Chemistry) among many others. The intellectual interaction with R. Clayton in his classes is certainly one of my best memories on Caltech professors.

I would like to acknowledge the indispensable inputs from my talented collaborators in various projects: T. J. Ahrens (shock wave), P. D. Asimow (high-pressure synthesis), T. Çağın (molecular dynamics simulations), G. Chen (thermal physics, MIT), W. A. Goddard III (molecular dynamics simulations), D. V. Helmberger (wave propagation), J. L. Mosenfelder (high-pressure synthesis), S. Ni (wave propagation),

A. Strachan (molecular dynamics simulations), D. Swift (laser and magnetic shock waves, and *ab initio* simulations, LANL), O. Tschauner (condensed matter physics, UNLV), W. Liu (thermal physics, UCLA), and S. Zhuang (shock waves).

An ensemble of scientists outside Caltech have supplied kind supports in various ways: D. Andrault (IPGP, France), R. Boehler (Max-Planck, Germany), C. Bradley (LANL), D. Dreger (Berkeley), T. Duffy (Princeton), E. Gaffney (LANL), R. J. Hemley (Geophys. Lab, CIW), R. Jeanloz (Berkeley), A. Koskelo (LANL), H.-K. Mao (Geophys. Lab, CIW), C. Mailhiot (LLNL), X.-D. Song (UIUC), D. Swift (LANL), Z.-P. Tang (USTC) and C. Thomas (Liverpool, UK). I have also benefited from many other individuals at Caltech, in particular, J. Akins, E. Arredondo, L. Eisner, X. L. Huang, C. Ji, E. Johnson, W. Keller, H.-J. Lee, Q. Liu, S. Ni, J. Polet, B. Savage, A. H. Shen, Z. R. Wang and K. Xia. The work at the Shock Wave Laboratory would have been impossible without the professional support from P. Gelle, M. Long, C. McCaughey and S. Yamada.

I am grateful for financial supports from the National Science Foundation (Ahrens, Asimow and Helmberger) and the Seismological Laboratory for my research and education here at Caltech. NSF (Hemley) and Socitetá Italiana di Fisica mostly supported my attendance in “Enrico Fermi School of Physics.” The computational facility for molecular dynamics simulations has been supplied by Materials and Process Simulation Center, Beckman Institute, Caltech (Goddard). A Director’s Postdoctoral Fellowship at Los Alamos National Laboratory would allow me to continue to enjoy the luxury of engaging in beautiful science.

Finally, I would like to thank my family for everything, in particular, grandma Xiuting in Heaven, my parents, my wife and friend Vivian, and our coming son, Sean.

To my dear

Grandma Xiuting and son Sean

Abstract

Waveform and differential travel-time (DTT) of various PKP phases have been utilized to study the velocity variations at the core-mantle boundary (CMB) and the inner-core boundary (ICB). The spatial concentration of events and stations, and the significant variations in PKPab-PKPdf DTT and waveform of PKPab, indicate localized sharp lateral variation of velocity at the CMB as supported by simulations. Modeling of DTT's among PKiKP, PKIKP and PKP-B-diffracted (B_{diff}) phases, and waveform of B_{diff} supports that the ratio of relative velocity variations of S- and P-wave at the CMB is larger than 2, and that hemispheric P-wave velocity variations exist at the top of the inner core, and that D" structure is related to the ICB via core dynamics.

The equation of state of stishovite is obtained by direct shock wave loading up to 235 GPa as $K_{0T} = 306 \pm 5$ GPa and $K'_{0T} = 5.0 \pm 0.2$ where K_{0T} is ambient bulk modulus and K'_{0T} its pressure derivative. Phase diagram of silica (including melting curve) up to megabar pressure regime is established based on molecular dynamics (MD) simulations and dynamic and static experiments. Calculations show that perovskite is thermodynamically stable relative to the stishovite and periclase assemblage at lower mantle conditions. A detailed and quantitative examination is conducted on the thermodynamics and phase change mechanisms (including amorphization) that occur upon shock wave loading and unloading of silica. The systematics of maximum undercooling and superheating, are established by incorporating normalized energy barrier for nucleation and heating (cooling) rate, and validated at the atomic level with systematic MD simulations. By considering superheating in shock wave experiments, high-pressure melting curves for silica, alkali halides and transition metals are constructed based on the Lindemann law and the $ln2$ rule for the entropy of melting.

Contents

List of Figures

List of Tables

Preface

> `What makes a crystal interesting is its defects and impurities;`
> `What makes the Earth's interior intriguing is its heterogeneities.`

A perfect crystal without any defect or impurity, and a perfect spherical layered Earth without any lateral variations, may be aesthetically favored. But heterogeneity is ubiquitous. It is heterogeneity that makes the physical world function in a chaotic order, and induces interesting diversities. For instances, line defect (dislocation) allows metals to deform plastically, an advantage serving human being since the very beginning of the civilization. The captivating appearance of the Earth's surface is created by the driving forces mostly due to the chemical and thermal heterogeneities inside. Investigations of the seismic, chemical and thermal heterogeneities in the Earth's deep interior are crucial to our understanding of the evolution of terrestrial planets. (The first-order compositional and thermal models of the Earth are still under debate though.)

Seismic techniques mostly involve travel time (t) and waveform of various seismic phases, *e.g.*, PKP triplications. To construct a chemical model of the Earth requires knowledge of the physical properties (*e.g.*, thermodynamic phase changes) of candidate minerals at the pressure (P) and temperature (T) comparable to those in the Earth's interior. Thermodynamic and seismic phase changes are due to distinct physics but related. Seismic phase change is defined as appearance (or disappearance) of a seismic phase (arrival) due to the changes in velocity-density model (M) for a given source-receiver pair. Although van der Waals (vdW) equation of state (EOS) is not applicable to the condensed matters inside the Earth, its $g-P$ ($g \equiv$ Gibbs free energy) triplication (Figure 1) can help the understanding of seismic phase changes

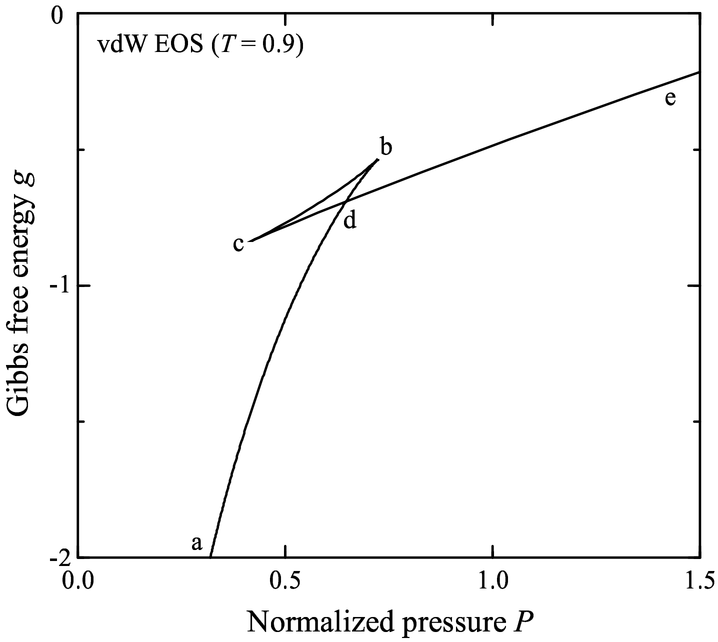

Figure 1: Isothermal $g - P$ triplication for a vdW EOS normalized by values at the critical point (P_c, T_c, V_c) and $T = 0.9T_c$. ad and de, db and cd are stable and metastable gas and liquid, respectively. bc is unstable and physically prohibited for a vdW system. $g(P)$ and $t(\Delta)$, and their first and second derivatives, are analogous to each other.

related to seismic triplication $t - \Delta$ ($\Delta \equiv$ epicenter distance). Analogy between $g - P$ and $t - \Delta$ triplications has been established [*Luo*, 2000] as $g \leftrightarrow t$, $P \leftrightarrow \Delta$, $T \leftrightarrow M$, $V \leftrightarrow p$, and $K_T \leftrightarrow K_M$, where V is volume, and bulk modulus $K_T \equiv -V\partial P/\partial V|_T$, p is ray parameter, and seismic stiffness $K_M \equiv -p\partial\Delta/\partial p|_M$. $g - P$ triplication occurs at $T < T_c$, where T_c refers to the critical point for a vdW system, and $t - \Delta$ triplication can be induced by large spatial variations in M. Catastrophes occur at caustics in both triplications. The thermodynamic phase changes, and elastic properties of Earth materials are manifested in the behavior of seismic phases.

The vast diversity of geophysical phenomena can be attributed to P, T and heat production in the Earth's interior, and the thermodynamic, elastic (and plastic) and transport properties of its constituents. The static and dynamic behavior of the Earth are governed by a few physical (quantum, Newtonian and statistical) laws spanning a colossal range of temporal (from femtosecond to geological time) and spatial (from atomic spacing ∼ Å to continuum) scales. Quantum mechanics, statistical mechanics and classical thermodynamics, and the conservation laws of mass, momentum, and energy are the physics connecting seismic observations, chemical composition, heat balance and dynamic evolution of the Earth.

This dissertation is by no means intended to construct a complete integrated picture of the Earth, which certainly requires the long-term joint efforts from several scientific communities. A few attempts have been made toward understanding the Earth's interior [*Luo et al.*, 2001, 2002a, c, d, e, f; *Luo and Ahrens*, 2003a; *Luo et al.*, 2003a; *Luo and Ahrens*, 2003b; *Luo et al.*, 2003b], and a large portion of my research is included in this thesis. Chapters 1-2 investigate the heterogeneities near the core-mantle boundary (CMB) and inner-core boundary (ICB) with PKP phases. Chapters 3-5 discuss the static and dynamic behavior of silica under high pressures. Results from static and dynamic experiments, molecular dynamics simulations and thermodynamic calculations are included. The systematics of maximum superheating and undercooling and the implications to high-pressure melting of geophysically important minerals, are presented in Chapter 6.

Chapter 1

Evidence for a Sharp Lateral Variation of Velocity at Core-mantle Boundary from Multipathed PKPab

Abstract

Rapid changes in differential travel times between the various PKP branches have been attributed to strong lateral velocity variations at the base of the mantle. Differential time PKPab-df residuals showing jumps of up to 2 seconds for paths only 100 km apart have been reported. Such extreme changes in travel times for signals with comparable wavelengths suggest ray bifurcation with multi-paths containing slow and fast contributions to PKPab. Here we report on some well-documented normal and multipathed PKPab phases along with rapidly varying differential time residuals observed for Fiji-Tonga events with paths sampling the northern edge of the mid-Pacific large slow structure (LSS) beneath Hawaii. Systematic analyses of these data with 2-D models suggest the presence of a ridge-shaped structure at the core-mantle boundary containing abrupt reductions of P-wave velocity of up to 10%. This narrow ultralow velocity zone (ULVZ) is located at the boundary between a large scale low velocity and high velocity structure, corroborating recent dynamic models which propose that ULVZs preferentially occur at the boundary between hot and cold mantle domains and could be related to plume activity at Hawaii.

1.1 Introduction

PKP triplication phases (PKPab, PKPbc and PKPdf) are due to velocity discontinuities at core-mantle boundary (CMB) and inner-core boundary (ICB). PKPab (outer-core) grazes the CMB at a large incident angle before entering the core while PKPdf (inner-core) penetrates CMB structures more steeply (Figure 1.1). The raypaths of PKPab and PKPdf approach each other near the receiver which makes their differential behavior less sensitive to the complex surface variations. At deeper depths these raypaths separate and become less symmetric in the sense that PKPab piercing points cluster on the receiver side and have more aperture on the source side at CMB and vise versa for PKPdf. Since small changes in CMB velocity structure can perturb PKPab path effectively, its travel time and waveform become sensitive to structure at CMB. Thus, the differential characteristics of these two PKP phases have been used to study the core-mantle boundary and inner-core structures, e.g., *Creager* [1992], *Breger et al.* [1999], *Song and Helmberger* [1997] and *McSweeny et al.* [1997]. In this work, we utilize 2-D waveform modeling technique to explain the variations in waveform and differential time residuals between PKPab and PKPdf observed by a dense broadband array (NARS) in Spain. The modeling results are presented with possible implications.

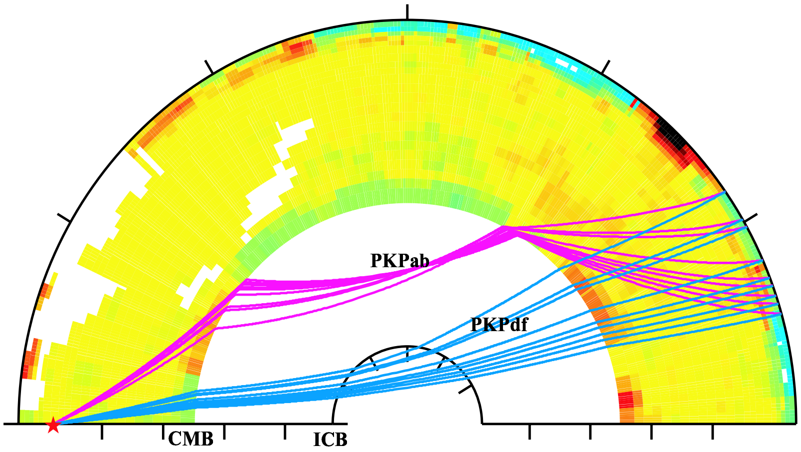

Figure 1.1: Raypaths for PKPab (purple) and PKPdf (blue) for different epicenter distances, plotted on an S tomography model [*Grand et al.*, 1997]. The cross section is chosen along Fiji-to-Spain great circle path direction. CMB indicates the core-mantle boundary, and ICB the inner-core boundary. Note that the piercing points for PKPab cover a wider range at CMB on the source side than on the receiver side and vise versa for PKPdf. The color scale is ±4% (S velocity) with red being slow and blue fast relative to PREM [*Dziewonski and Anderson*, 1981].

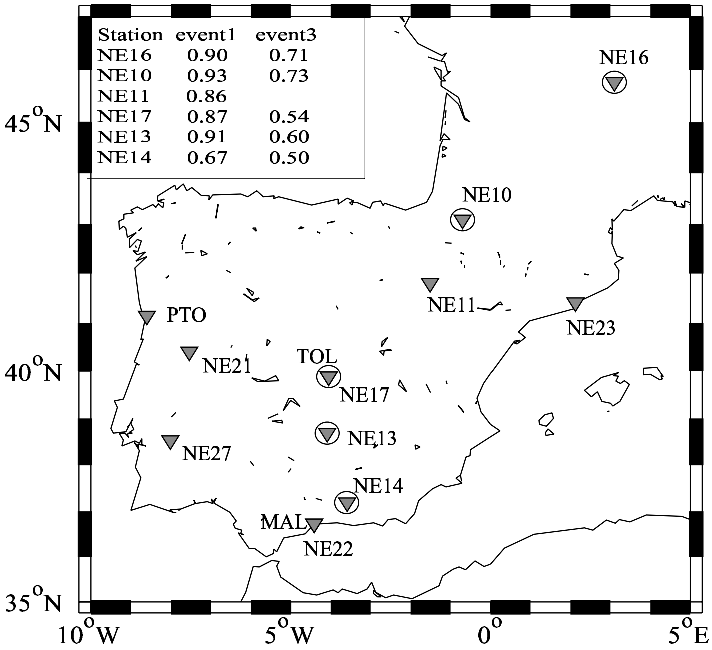

Station	event1	event3
NE16	0.90	0.71
NE10	0.93	0.73
NE11	0.86	
NE17	0.87	0.54
NE13	0.91	0.60
NE14	0.67	0.50

Figure 1.2: Map of seismic stations in NARS array (this study) and WWSSN (PTO, TOL and MAL) used by *Song and Helmberger* [1995]. Stations indicated as circled inverse triangles recorded multipathed PKPab phases (complex waveforms). The cross-correlation coefficients between PKPab and PKPdf for Event 1 and 3 are shown in the upper-left corner. Refer to Figure 1.3.

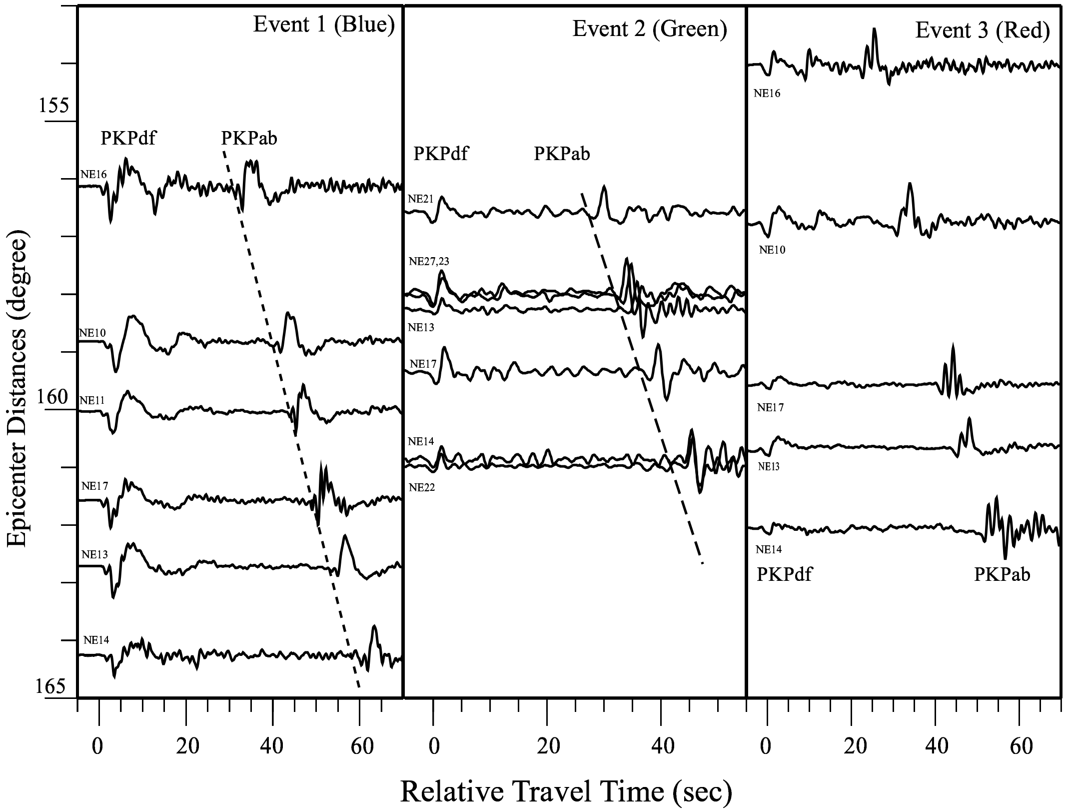

Figure 1.3: Seismic recordings at NARS array from three Fiji events (860616, 880719 and 860526) aligned on PKPdf. The focal depths are 565, 90 and 538 km for Event 1-3, respectively. Dashed lines are PKPab arrivals predicted by PREM. Note that the PKPab phase at NE14 for Event 1 is delayed relative to PKPdf as are those at NE13, 14, 17, 22 and 23 for Event 2, and that PKPab at NE14 for Event 1 and those for Event 3 are multipathed or distorted. Great circle paths are blue, green and red for Event 1-3, respectively, in Figures 1.4 and 1.5.

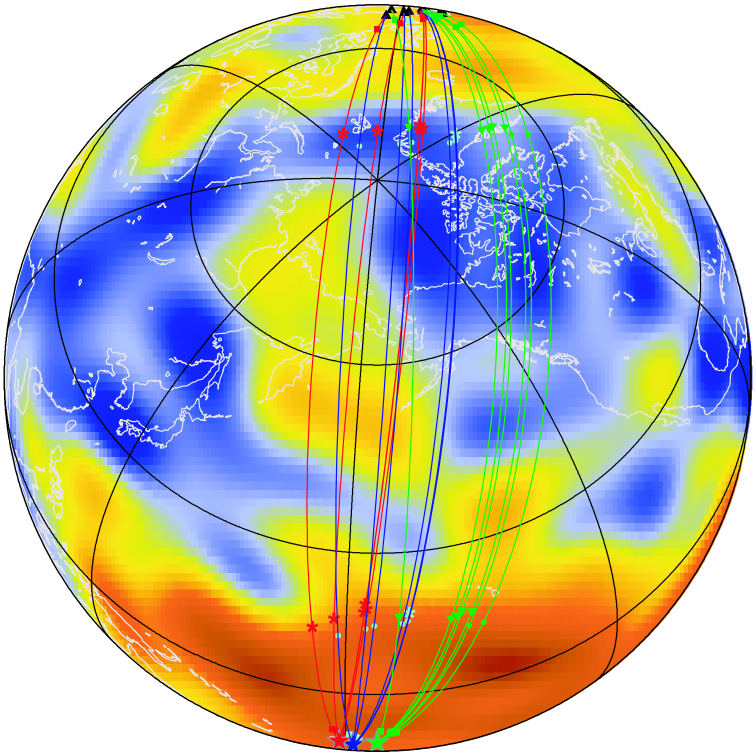

Figure 1.4: The great circle paths of event-receiver pairs and piercing points of PKPab and PKPdf at the CMB, plotted on an S tomography model *Ritsema et al.* [1999] for the lowermost mantle. Blue represents Event 1, green Event 2 and red Event 3. The color scale is ±2.5%. Red indicates slow and blue fast velocities relative to PREM. Stars indicate epicenters, black triangles receivers, solid lines great circle paths, squares piercing points of PKPdf at the CMB, other symbols indicate PKPab piercing points at the CMB and observed characteristics of PKPab relative to PREM: (1) dot denotes normal differential time and waveform; (2) inverse triangle denotes positive PKP(ab-df) residual with normal waveform and (3) asterisk denotes multi-pathed or distorted PKPab.

1.2 Observation

A useful technique for systematically determining the differential times has been proposed by *Shearer and Toy* [1991], where one uses the observed waveform directly to estimate the differential time. The PKPab phase should be ideally phase-shifted by 90° or Hilbert-transformed since it is a maximum travel time phase [*Choy and Richards*, 1975]. One such data set analyzed with this method was addressed by *Song and Helmberger* [1993]. They found that one of the most anomalous differential

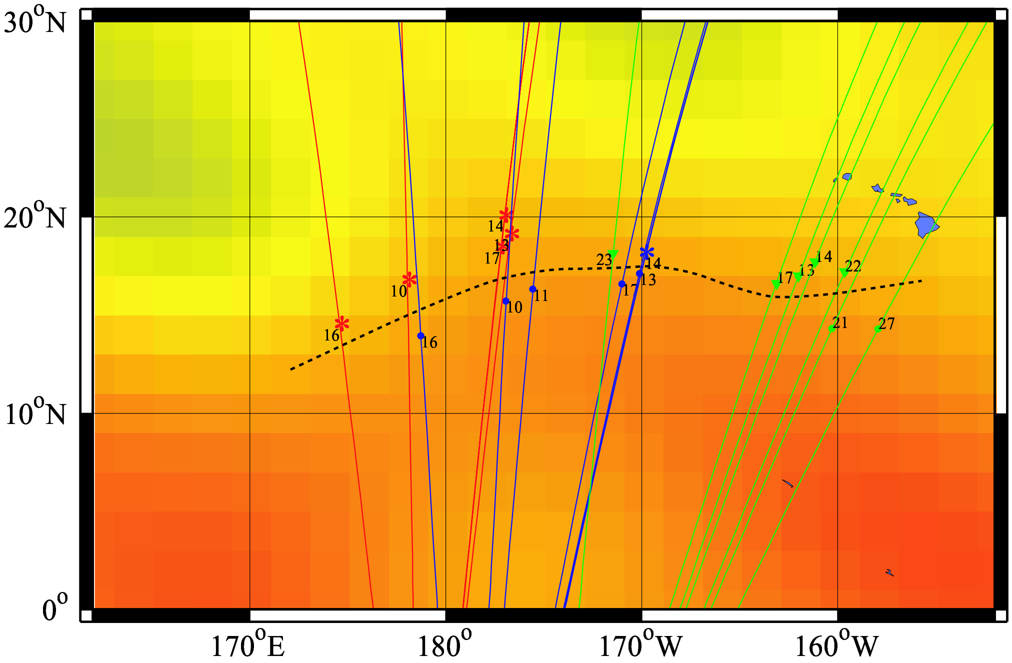

Figure 1.5: Portions of the great circle paths on the source side. The color scale is ±4%. The dashed line is a schematic drawing of the southern boundary of the ULVZ causing the waveform complexity and PKP(ab-df) residual variations (see text). Note that the blue patches are Hawaiian islands. Notations are same as in Figure 1.4. The numbers correspond to receivers at the NARS array discussed in Figure 1.2.

times observed occurred at station TOL in Spain from Fiji-Tonga events (Figure 1.2). *Helffrich and Sacks* [1994] suggested that this feature could be caused by diffraction of a slab near the source but this is disputed by *Song and Helmberger* [1997], who argue against this interpretation in that anomalous differential times are independent of source depth. *Song and Helmberger* [1995] analyzed a seismic record section which displays rapidly changing differential behavior at neighboring stations, PTO, TOL and MAL and found that PKP(ab-df) residuals for MAL are consistently 2 seconds larger than those for PTO and TOL. These rapid changes in differential travel times are also apparent in NARS observations (NE stations in Figure 1.2). Some examples of PKP observations recorded by this temporary broadband array are shown in Figure 1.3, aligned on PKPdf. The dotted lines indicate the PKPab arrivals predicted by PREM. The PKPab phase arrives about 2 seconds late relative to PREM at NE14 for Event 1 as determined by waveform correlation, although its wave shape is somewhat complex. This result is in agreement with the earlier studies with PTO, TOL and MAL and with observations in column 2 for Event 2 in Figure 1.3, where again PKPab observations in western Iberia (NE21) arrive early relative to southeastern stations (NE14 and NE22). Event 3 is recorded by most of the same stations but displays a much more complex PKPab as is apparent in column 3 of Figure 1.3 and in their cross-correlation coefficients in Figure 1.2. This result suggests that the crustal structure near the receiver is probably not the dominant cause of the observed features in seismograms since it is common to all the events. Note that PKPdf is relatively simple and a check of the focal mechanism (CMT) indicates that both PKPdf and PKPab are well-away from nodal planes. Thus, the source properties should be relatively stable and it becomes difficult to explain the rapid changes in PKPab waveform compared to PKPdf, e.g., NE10 to NE17. Although strong azimuthal variation in receiver effects cannot be completely eliminated, we will attempt to explain this feature as a propagation distortion caused by a deep localized structure.

Because PKPab is sensitive to structure in the lowermost mantle, the variations in data are expected to be associated with variations of structure near the CMB. The great circle paths for these event-station pairs are plotted against a tomography model [*Ritsema et al.*, 1999] with the piercing points of PKPab and PKPdf at the CMB (Figure 1.4). The region where PKPab hitpoints at CMB cluster on the source side is displayed in Figure 1.5. The dashed line separates the early and normal PKPab arrivals (dots) from the late (triangles and blue asterisk) and complex PKPab arrivals (red and blue asterisks). The transition is about 1-3 degrees spatially, so the lateral variation of the CMB structure must be rapid. Although the piercing points of PKPab at the CMB move a few degrees spatially on the source side along the great circle path, they remain nearly identical on the receiver side (Figure 1.1). And, since Events 1 and 3 are both deep and less susceptible to slabs, we attribute this dramatic change to rapid lateral variation at the CMB near the transition zone structure from slow to fast (Figure 1.5). Data show that waveform and differential time residuals vary along great circle path direction and azimuthally, suggesting a 3-D structure near the CMB to account for the observed features.

1.3 Modeling

Could tomographic models predict these observed features? Due to the limited data coverage and relatively poor resolution of P tomography for the lowermost mantle, we scale the shear wave models [*Grand et al.*, 1997] into P models to model the waveforms by assuming $dlnV_s/dlnV_p = k$ as utilized by many investigators (e.g., *Breger et al.* [2000]). For the case of $k = 1$, significant differential time changes can be produced without obvious waveform changes (Figure 1.6). Assuming $k = 2$, a more commonly used value, predicts even smaller effects. Thus, the relative smoothness of such tomographic models cannot produce the observed waveform complexities but help to explain the observed differential time variation.

The synthetics presented in Figure 1.6 were generated by a code based on generalized ray theory (GRT) modified to correct for laterally varying structures by *Ni et al.* [2000]. The procedure begins by tracing rays through a radially symmetric 1-D Earth model. Then the 2-D tomographic velocity variations are added and the rays regenerated to satisfy Snell's law. This approximation is roughly equivalent to

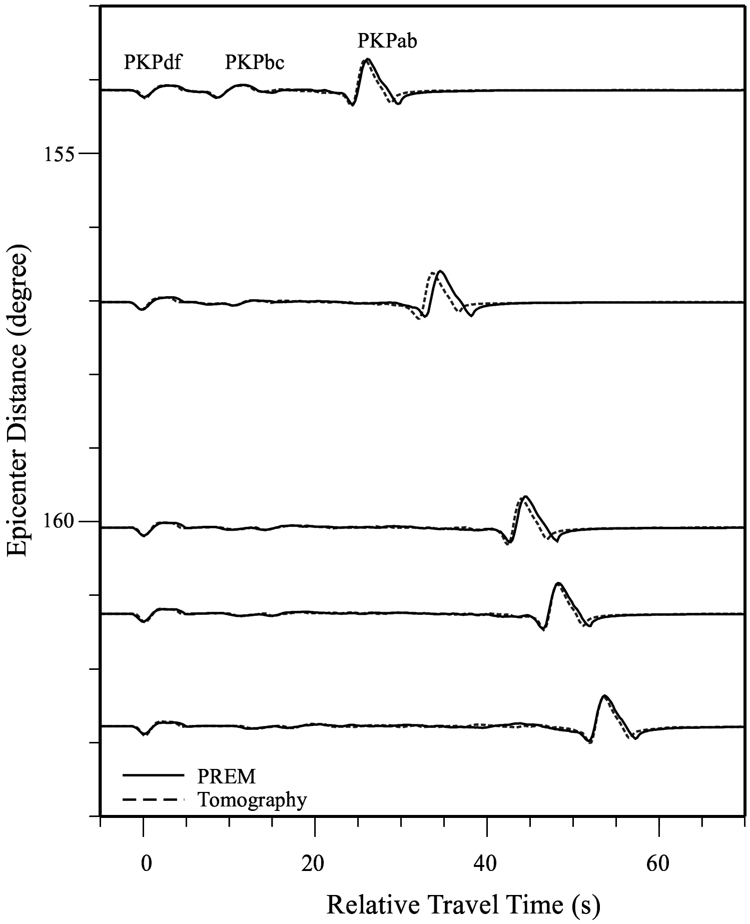

Figure 1.6: Comparison of 1-D (PREM) synthetics with those based on the model modified from an S tomography model [*Grand et al.*, 1997] where $dlnV_s/dlnV_p = 1$ was used to convert S model to P. Synthetics along great circle paths similar to those in the data show travel time changes and relatively simple PKPab waveforms. The synthetics are aligned on PKPdf.

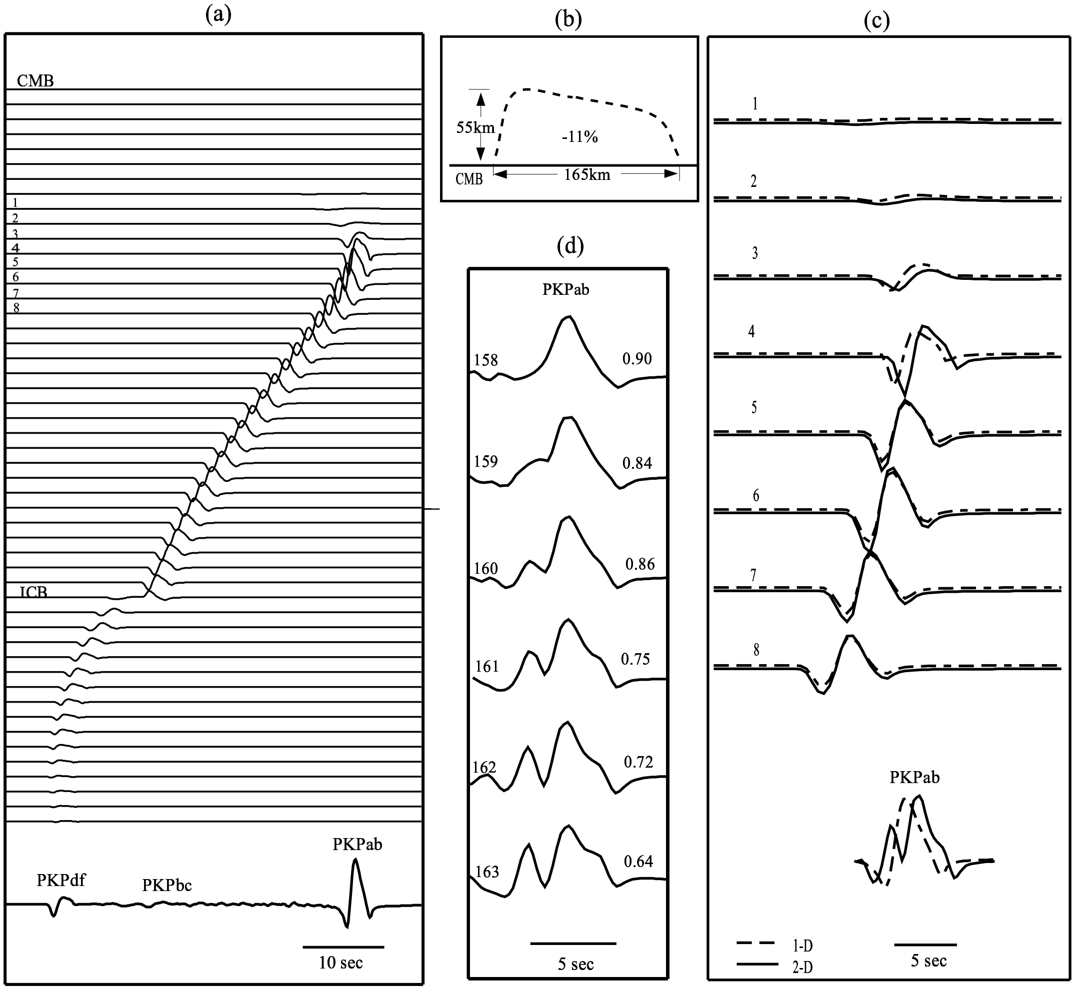

Figure 1.7: (a) Shows how GRT synthetics are constructed for a 1-D layered model where the bottom trace is the complete synthetic for Event 3 at distance of 162°. Each trace (except bottom trace which is the complete sum) represents the sum of the generalized ray contributions from 5 consecutive layers of the model (PREM). The main contribution to PKPab is from the traces labeled with 1-8. Trace 4 is nearest to the PKPab geometrical ray contribution. (b) is a 2-D model used to produce multipathed PKPab. The velocity contrast is -11% relative to PREM. (c) shows the changes of traces 1-8 and PKPab synthetic of 162° from 2-D model in (b) with respect to PREM. (d) is the synthetic PKPab profile for 2-D model in (b) from 158° to 163°. The number at the right side is the cross-correlation coefficient between PKPab and PKPdf of the synthetics and the number on the left side is the epicenter distance. The PKPdf and PKPbc are normal and not shown.

applying a local stretching methodology for mapping a complex structure into a localized layered model where the model is ray-parameter dependent [*Helmberger et al.*, 1996]. Contributions from individual layers are computed with the Cagniard-deHoop method and summed to produce a synthetic seismogram. Figure 1.7a displays the basic interaction of these ray-packets in constructing the motion. Each trace contains the sum of contributions from 5 even thinner layers. These individual traces are displayed sequentially from the inner-core (bottom) to the CMB (top). The sum of these bundles is used to construct the bottom synthetic with the main PKP phases labeled. Note that the PKPdf pulse comes from the inner-core while the PKPab pulse is produced by a delicate interference of the last arriving bundles (maximum travel time phase). The roughness in the final summation is caused by the intrinsic layered structure [*Helmberger*, 1973].

Tomographic models that have been smoothed by their construction typically produce small shifts in timing as displayed in Figure 1.6, with minor distortions of principal phases. The main energy forming the PKPab phase is produced from bundles of rays sampling a depth zone of about 50 km, centered roughly on the geometric ray as can be deduced from Figure 1.7a. This beam of rays spread out near the CMB due to the nonlinear behavior of the sine-function describing Snell's law (Figure 1.8). It consequently thins back down traveling upward to the surface. For the distance of 162°, the beam covers about 300 km horizontally at the CMB but narrows back down approaching the source and receiver, roughly 5 km at a depth of 700 km. Thus, the easy way to split this packet of rays is to place an anomaly in the beam near the CMB. A thin lens-like structure produces a stronger impact above the CMB than below because of the alignment with raypath. By varying the anomaly's geometry, dimension, location and velocity contrast relative to PREM, synthetics with multipathed PKPab can be obtained. A particularly effective structure (Figure 1.7b) proves to be an ultralow velocity zone (ULVZ) [*Wen and Helmberger*, 1998b] with height of 55 km, width of 165km, velocity decrease of 11% located where the PKPab geometric ray pierces the CMB structure.

Figure 1.7c displays the individual wavelet changes relative to the reference model

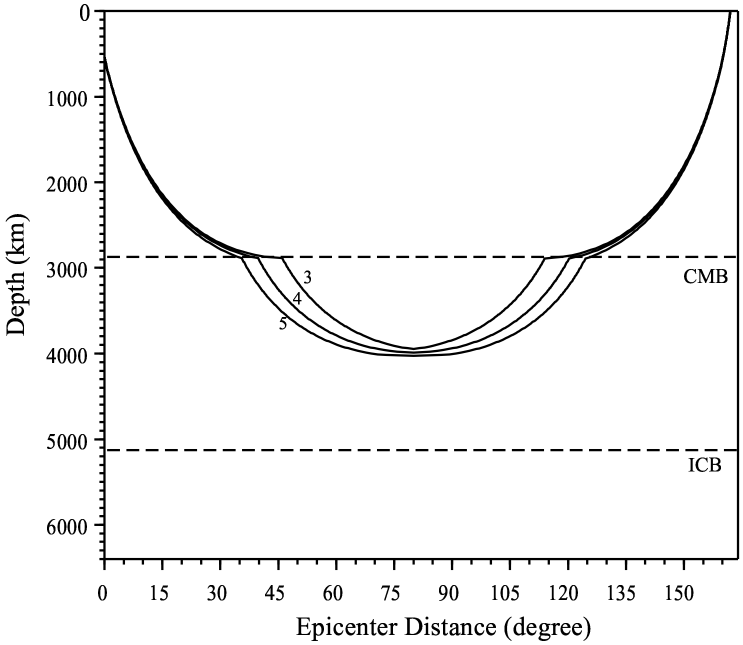

Figure 1.8: Display of a few raypaths adjacent to the geometric ray (4) described in Figure 1.7 that contribute to PKPab (depth 538km, epicenter distance 162°). Small shifts in their arrival times can cause waveform distortions. Thus the fine-scale velocity variations traversed by ray 3 and 4 but not ray 5 or the reverse can cause distortions. Note that it is particularly difficult for ray 3, 4 and 5 to encounter very different structure in the upper-mantle (say, 700 km depth) since they are separated by only a few kilometers. The most efficient location is near the CMB or in the fluid core although the latter is probably quite homogeneous. While the synthetics generated here are for 2-D, it is easy to see how 3-D structures positioned at the CMB could produce a complex wavefield.

at layers with dominant contributions to PKPab. Note that about half of the pulse is shifted back (trace 4) by about 1.5 seconds which is primarily causing the waveform complexity. Other models with thicker structures but with smaller velocity drops or thinner structures with still stronger velocity drops are possible as long as they can produce a few seconds of timing shifts. The shape displayed here is chosen to be roughly compatible with previous ULVZ studies [*Wen and Helmberger*, 1998a]. Figure 1.7d shows a profile of PKPab waveform changes from 158° to 163° epicenter distance with the same focal depth and radiation pattern as Event 3. This means that for the same azimuth, multipathed PKPab will occur at greater epicenter distance for this 2-D anomaly. Perhaps, this explains why the multipathed PKPab occurs at NE13, NE14 and NE17 for Event 3 but not as apparent at NE10 and NE11 for Event 1 in the same azimuth. The cross-correlation coefficients of the synthetics decrease as the mutlipathed PKPab develops (Figure 1.7d) which is consistent with observations. Multipathed PKPab can occur at smaller epicenter distances with corresponding geometry, dimension and velocity deficits by positioning the anomaly nearer the source. This could be the reason why the multipathed PKPab appears at NE10 and NE16 for Event 3 but not at NE16 for Event 1 as displayed in Figure 1.5. Thus we propose a 3-D ULVZ with a boundary schematically depicted as a dashed line in Figure 1.5 to account for the anomalies observed in the data (travel time, complex waveform and the reduced cross-correlation coefficient). The width of the ULVZ (in great circle path direction) is 150-300 km, height 50-100 km, and velocity deficit of 8-12%. However, due to limited data coverage, the detailed structure for this region remains uncertain but this anomaly could easily pass beneath Hawaii. The 3-D effect may complicate the waveform and also cause uncertainties in waveform modeling.

Suppose that source complexities contributed to complexities in PKPab waveform for Event 3. For a worst case, we assume that a specific source produces normal PKPdf but a double-pulse PKPab at NE16 for Event 3. Synthetics are then obtained for other stations for Event 3 by assuming PKPdf of NE16 as the source for PKPdf synthesis, and the Hilbert transform of PKPab at NE16 as the source for PKPab synthesis. As we can see from Figure 1.9 (Data and 1-D), complicated sources cannot

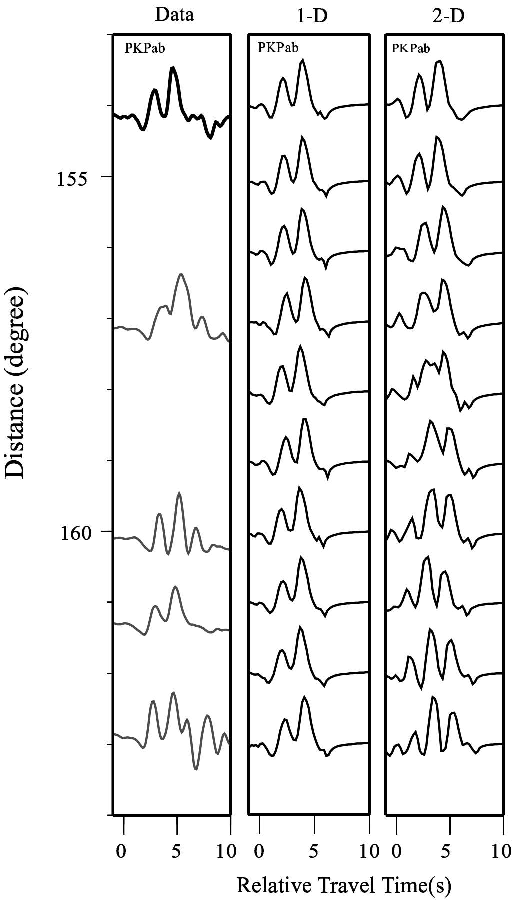

Figure 1.9: Comparison of the complicated PKPab observations for Event 3 against 1-D and 2-D synthetics. The source time function for synthetics is the top trace in the data column. The 2-D structure is the same as Figure 1.7b. The match at the top is produced primarily by construction (see text). The 1-D synthetics do not change shape with epicenter distances as expected. The 2-D synthetics become quite complicated as the interaction between the periodicities (of source and structure anomaly) changes with epicenter distance. They do not fit the data exactly since waveform depends on the choice of source and structure, but adding the complexity caused by the 2-D structure produces some of the observed attributes.

explain the differences between the records at the various stations. However, adding complexities produced by the 2-D structure along with double-pulse type source (2-D in Figure 1.9) starts to produce the rapid variations observed. Since this ULVZ structure could be quite complex and 3-D in nature, we might expect the data to be produced by some-type of interference pattern. If this is the case, we would need a dense array of stations to obtain an accurate structural representation.

1.4 Discussion and Conclusion

The tomographic studies discussed here (Figure 1.4 and 1.5) indicate that a rather large slow structure (LSS) exists at the CMB beneath the mid-Pacific. This structure extends upward to the upper-mantle with shear velocity reductions of up to 2% and seems to have an anomalous high-density region near the bottom [*Ishii and Tromp*, 1999]. It appears that the entire region is sitting on a slow basal layer with variable thickness [*Wysession et al.*, 1998; *Mori and Helmberger*, 1995; *Garnero and Helmberger*, 1995]. Adding an extra slow layer at the CMB and/or simply inflating the predicted P-velocity from S-wave tomography can significantly reduce the observed variance in PKP(ab-df) as demonstrated by *Song and Helmberger* [1997] and *Breger et al.* [2000]. Note that our results in Figure 1.6 improve the relative timing between PKPab and PKPdf in agreement with the above travel time studies. However, the position of this LSS as determined from tomography appears to be somewhat uncertain as deduced by comparing proposed models such as *Grand et al.* [1997], *Ritsema et al.* [1997], *Liu et al.* [1994], *Li and Romanowicz* [1996], and *Masters et al.* [1996]. They mostly agree that the northern edge is near the dotted line in Figure 1.5. A particularly sharp boundary along this edge is displayed by *Wysession* [1996] which could be associated with 200 m.yr. subduction indicated by *Richards and Engebreston* [1992]. This suggests that the relatively cold and fast slab material is adjacent to the LSS, probably near the dotted boundary displayed in Figure 1.5. Similarly, *Breger and Romanowicz* [1998] report on a sharp jump in S wave velocity structure of up to 10% along the northern edge to explain the differential times in S, SKS

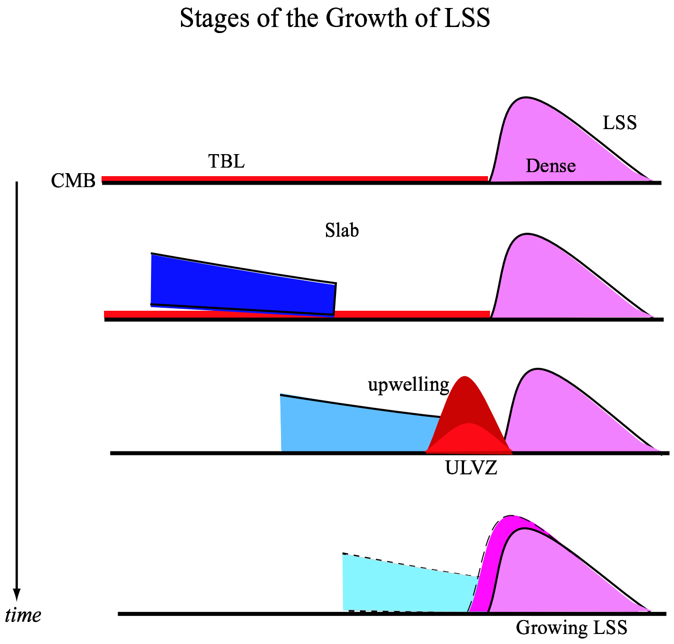

Figure 1.10: Stages of growth of a large slow structure (LSS). TBL is the thermal boundary layer at the CMB. The preexistent LSS is hot and dense. As the relatively cold slab flows due to the negative buoyancy, a thick zone composed of partially melted slab and core sediments [*Buffett et al.*, 2000] forms between the slab and the LSS, and a ULVZ develops at its base. Differentiation of this hot material could rain out dense components thus enlarging the bottom half of the LSS. The lighter components would rise and possibly form a plume too narrow to be seen by present techniques. We suppose that this process would be episodic, perhaps occurring in relatively short periods of geological time as suggested by *Thompson and Tackley* [1998] and *Brandon et al.* [1999].

and SKKS. And, *Russell and Lay* [1999] found S wave velocity and anisotropy heterogeneity at the CMB with ScS waves sampling the region near Hawaiian plume. But the southern boundary is more complex in nature as denoted by the above authors. However, several studies report on strong anomalies near this transition region [*Wen and Helmberger*, 1998a, b; *Vidale and Hedlin*, 1998]. The study by *Wen and Helmberger* [1998b] invokes a Gaussian-shaped feature not unlike the one derived above(Figure 1.7b) to explain broadband PKP precursors located near the edge.

Thus, it appears that ULVZs occur not directly beneath the LSS but near edges or transitions. Note that a similar result is developed for the great African anomaly [*Helmberger et al.*, 2000; *Ni and Helmberger*, 2001]. Recent dynamic models [*Sidorin* *et al.*, 1998; *Tan and Gurnis*, 2000] suggest that ULVZ may preferentially occur on the boundary between hot and cold regimes at the CMB. A variety of mechanisms (squeezing effect, small scale convection and chemical heterogeneity etc.) could cause a hot zone developed between the slab and the LSS (Figure 1.10). In this scheme, the zone is composed of partially melted slab and core sediments gathered at the top of the CMB (rich in core content [*Buffett et al.*, 2000]) with a possible ULVZ at its base and could develop into an upwelling. The dense components of this upwelling could differentiate and sink and enlarge the preexistent LSS [*Zhang and Yuen*, 1997; *Thompson and Tackley*, 1998]. A possible upwelling formed in this way could be rich in core content and hence provide the unique geochemistry observed at Hawaii [*Brandon et al.*, 1999].

In conclusion, we present evidence for an ultra-low velocity zone located along the northern edge of the large-scale mid-Pacific low velocity structure. This discovery is primarily based on the multi-path behavior of the PKPab observations sampling this particular transitional region. These features can be explained by introducing extreme changes in velocity as demonstrated by the 2-D modeling. The occurrence of this ULVZ at the transition of a large scale slow-to-fast structure suggests a physical connection between mantle downwelling and upwelling processes evident in recent dynamic models and may be related to plume activity at Hawaii.

Acknowledgements: We thank D. L. Anderson, X.-D. Song, M. Gurnis, J. Ritsema and P. Asimow for thoughtful comments. The comments by T. Lay and an anonymous reviewer help improve the manuscript. S. Ni and D. V. Helmberger contributed partly to this work.

Chapter 2

Relationship of D” Structure with the Velocity Variations near the Inner-core Boundary

Abstract

Variations in regional differential times between PKiKP (i) and PKIKP (I) have been attributed to hemispheric P-velocity variations of about 1% in the upper 100 km of the inner-core (referred to as HIC). The top of the inner-core appears relatively fast beneath Asia where D” is also fast. An alternative interpretation could be the lateral variation in P velocity at the lowermost outer core (HOC) producing the same differential times. To resolve this issue, we introduce the diffracted PKP phase near the B caustic (B_{diff}) in the range of 139-145° epicenter distances, and the corresponding differential times between B_{diff} and PKiKP and PKIKP as observed on broadband arrays. Due to the long-wavelength nature of B_{diff}, we scaled the S-wave tomography model with k values ($k \equiv dlnV_s/dlnV_p$) to obtain large-scale P-wave velocity structure in the lower mantle as proposed by earlier studies. Waveform synthetics of B_{diff} constructed with small k's predict complex waveforms not commonly observed, confirming the validity of large scaling factor k. With P-velocity in lower mantle constrained at large scale, the extra travel-time constraint imposed by B_{diff} helps to resolve the HOC-HIC issue. Our preliminary results suggest $k > 2$ for the lowermost mantle and support HIC hypothesis. An important implication is that there appears to be a relationship of D” velocity structures with the structures near the inner-core boundary via core dynamics.

2.1 Introduction

The structure near the inner-core boundary (ICB) is important for constraining the seismic, dynamic and mineral-physical interpretations concerned with the deep Earth. This region presents challenges to seismologists because it lies beneath the complex D" which complicates conventional seismic methods. Therefore, most studies have employed differential times between neighboring phases (*e.g.*, *Choy and Cormier* [1983]; *Cormier and Choy* [1986]) to lessen the impact of passing through the laterally varying core-mantle boundary (CMB) structure. The paths for PKIKP and PKiKP remain remarkably similar when crossing the CMB and, thus, their differential times (δ_{iI}) can be used efficiently to study this important boundary (ICB) [*Niu and Wen*, 2001]. They found conclusive evidence for regional variation (roughly hemispherical) of ±0.5 seconds in δ_{iI} residuals relative to PREM [*Dziewonski and Anderson*, 1981] predictions which they interpreted as 0.8% variations in P wave velocity at the top 100 km of the inner-core with the eastern hemisphere (40°E-180°E) faster than the western (180°W-40°E), similar to the study by *Kaneshima* [1996]. Seismologically, the interpretation of δ_{iI} itself is not unique since the variation could occur in either the fluid outer core or the solid inner-core. With a seismic array, B_{diff} can be observed along with i and I in seismograms. B_{diff} is the diffracted PKP arrivals in the shadow zone of P wave, due to the major solid-liquid boundary (CMB), and thus long-wavelength in nature. The introduction of B_{diff} supplies one more independent differential time, δ_{iB} ($i - B_{diff}$) or δ_{IB} ($I - B_{diff}$), which can help constrain the interpretation of δ_{iI} given the knowledge of the lower mantle, or vise versa. To address this issue, we analyze recordings from three broadband arrays with respect to these hemispheric differences and discuss the tradeoffs between the lower mantle, outer- and inner-core heterogeneities, and the possible geophysical implications.

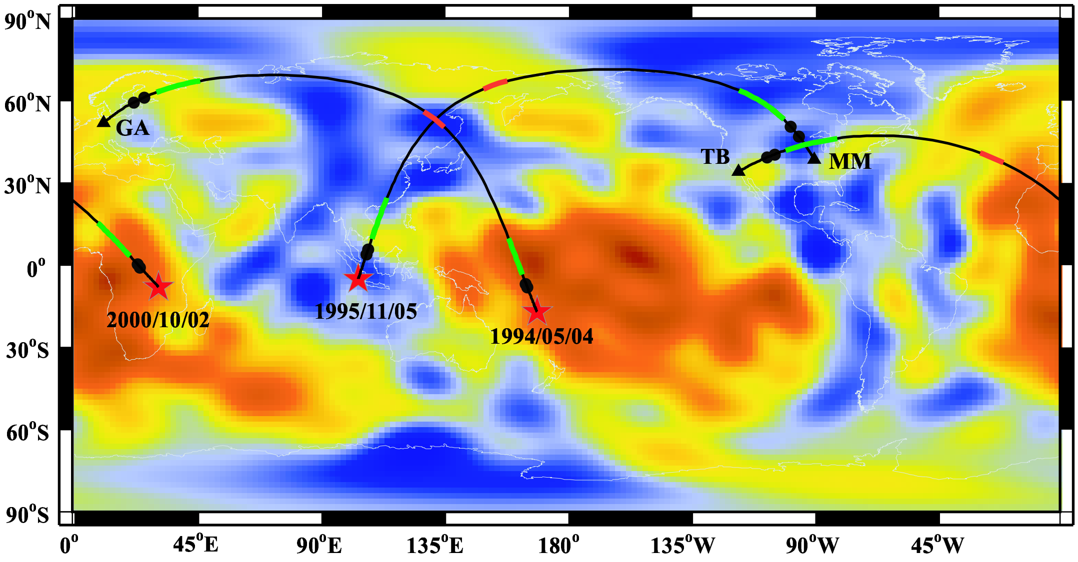

Figure 2.1: The great circle paths for event-array pairs plotted on an S tomography model for the lowermost mantle layer [*Ritsema et al.*, 1999]. Color scale is ±2.5% with blue being faster and red slower relative to PREM. Stars indicate events and triangles seismic arrays (GA, MM and TB). GA: German array; MM: MOMA array and TB: Trinet and Berkeley network. Black dots indicate the piercing points of PKIKP (I) and PKiKP (i) at the CMB, the green segments the regions sampled by B_{diff} at the CMB, and the red segments the inner-core sampled by PKIKP. Three events are: 20001002 (dep. = 10 km, mag. = 6.6), 19951105 (dep. = 58 km, mag. = 6.3) and 19940504 (dep. = 213 km, mag. = 5.8).

2.2 The observation and interpretation

We begin by reviewing some typical examples of the hemispheric nature of the observations as displayed in Figures 2.1 and 2.2. The observations at the German array (GA, Figure 2.2a) [*Thomas*, 1999] sample the eastern hemisphere where the δ_{iI} residuals are usually found to be positive relative to PREM and the mantle velocity at the CMB is relatively fast above the inner core as shown in the map view. These data can be contrasted with those observed at the MOMA array (MM, Figure 2.2b), where the δ_{iI} residuals are negative as predicted and the CMB is relatively slow. Both of these velocity record sections display a well-developed PKP caustic (near 144°) and B-diffractions at smaller distances. Since this phase (B_{diff}) is relatively long-period, it is more pronounced in displacement as shown in the observed Trinet-Berkeley (TB) profile (Figure 2.2c). These three record sections all show clear B_{diff}, I and i arrivals except that in the TB recordings i is not resolved due to the long-duration source time function. The differential time δ_{iI} residuals (R_{iI}) relative to PREM for GA and MM are distinct, positive R_{iI} for GA and negative for MM, consistent with the hemispherical observations [*Niu and Wen*, 2001], except that the inner-core region sampled by MM path is close to the transition which is not well resolved by former studies.

The most reasonable interpretation of δ_{iI} variation is the structure near the ICB, due to the fact that the raypaths of i and I phases differ the most near the ICB. Thus R_{iI} is most sensitive to the bottom of the outer core or the top of the inner-core or the ICB itself. This point is illustrated in Figure 2.3a. If the P velocity of the top 80 km of the inner-core is 0.8% faster than PREM (Figure 2.3b), R_{iI} becomes about 0.5 s. Keeping the inner-core unchanged but decreasing the P velocity of the bottom 50 km of the outer core by 0.9% (Figure 2.3c), results in comparable R_{iI}. If we increase the radius of the inner-core by 15 km instead (Figure 2.3d), R_{iI} becomes slightly positive. Thus for the case of $R_{iI} > 0$, increasing the velocity at the top of inner-core is equivalent to decreasing velocity at the bottom of the outer core except for minor waveform (*e.g.*, amplitude ratio) changes, while it is less efficient by changing the

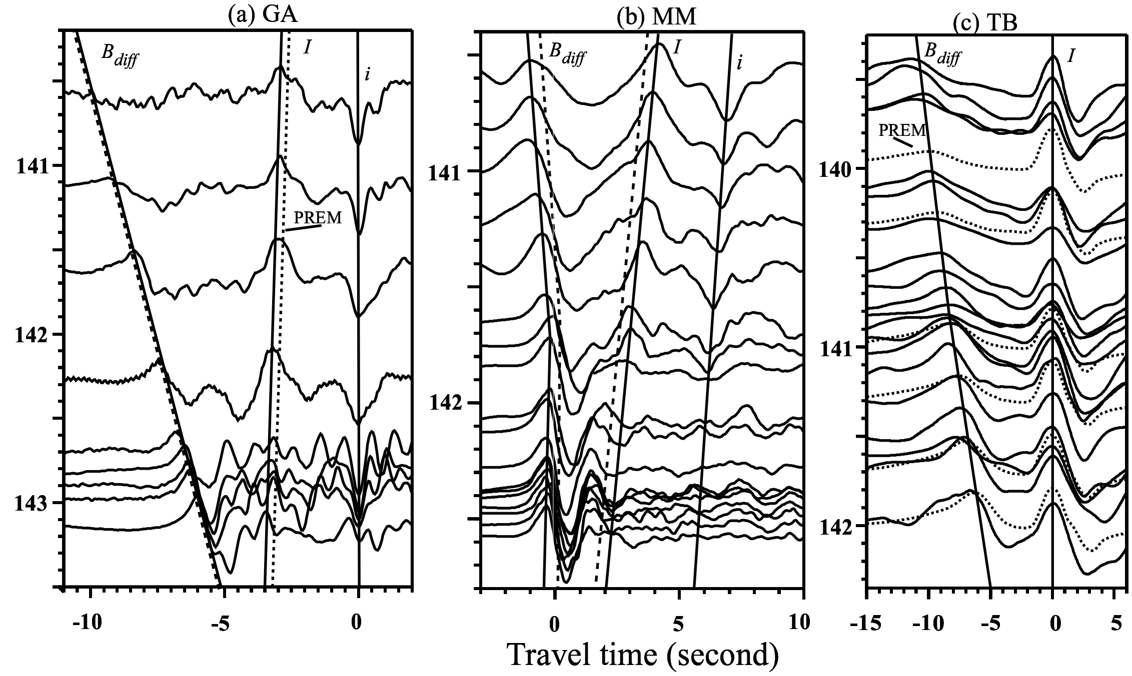

Figure 2.2: Record sections at GA, MM and TB. B_{diff}, I and i phases are picked along the solid lines. The dashed lines are PREM predictions for I and B_{diff} relative to i. The δ_{iI} residual is positive for GA where the CMB is relatively fast above the sampled ICB, and negative for MM where the CMB is relatively slow. The dotted curves in TB section are PREM synthetics. Note that the TB record section is in displacement where it is difficult to separate I from i.

radius of the inner-core. The topography of ICB could also change δ_{iI}, *e.g.*, a 15 km difference in topography for i and I could cause negative change of 0.3 s in R_{iI} (insert, Figure 2.3e). If the velocity above or below ICB or ICB topography changes in the opposite direction, R_{iI} will change sign accordingly. Different changes in the amplitude of velocity relative to PREM produce proportional changes in travel time residuals.

In short, the δ_{iI} result itself cannot rule out the possibility of the bottom fluid core being responsible for the anomalies of R_{iI}. Another important piece of information is the B_{diff}, which is easily identified in these dense broadband array record sections, providing rather accurate picks of the arrival time of B_{diff}. Thus we have one more independent differential time, δ_{iB} or δ_{IB} besides δ_{iI}, which can help clarify the interpretation of δ_{iI}. Figure 2.3a shows the relationships between B_{diff}, I and i. The differential times can be obtained by measuring the separation between the maximum-amplitude peaks [*Niu and Wen*, 2001], either in velocity or in displacement seismograms where B_{diff} is more pronounced. The corresponding residuals are obtained by subtracting PREM predictions from data (Figure 2.3e). The average R_{iI} for GA is about 0.4 s and that for MM is -0.3 s, which are close to the hemispheric results of other data sets [*Niu and Wen*, 2001]. R_{IB} for GA is about -0.4 s, 0.7 s for MM and about 0 for TB. R_{iB} for GA is almost zero and 0.35 s for MM. Of these three residuals, only two are independent. Unfortunately, we don't gain directly from B_{diff}, because although we obtain one more independent differential time, we also introduce one more unknown, namely the lowermost mantle (D"), which could affect δ_{iB} and δ_{IB}.

The scale-length of the region sampled by B_{diff} at the CMB ($500 - 1000$ km) is comparable to the resolution of tomography models. Due to the lack of a satisfactory P-wave tomographic model, some studies [*Dziewonski and Woodhouse*, 1987; *Ritsema and van Heijst*, 2000; *Robertson and Woodhouse*, 1995; *Masters et al.*, 2000] proposed to obtain P-wave model by scaling S-wave tomography models which have constraints from SKS and ScS. The scaling factor $k \equiv dlnV_s/dlnV_p$, is proposed to be close to or larger than 2 by various studies. First we will explore the k dependence of

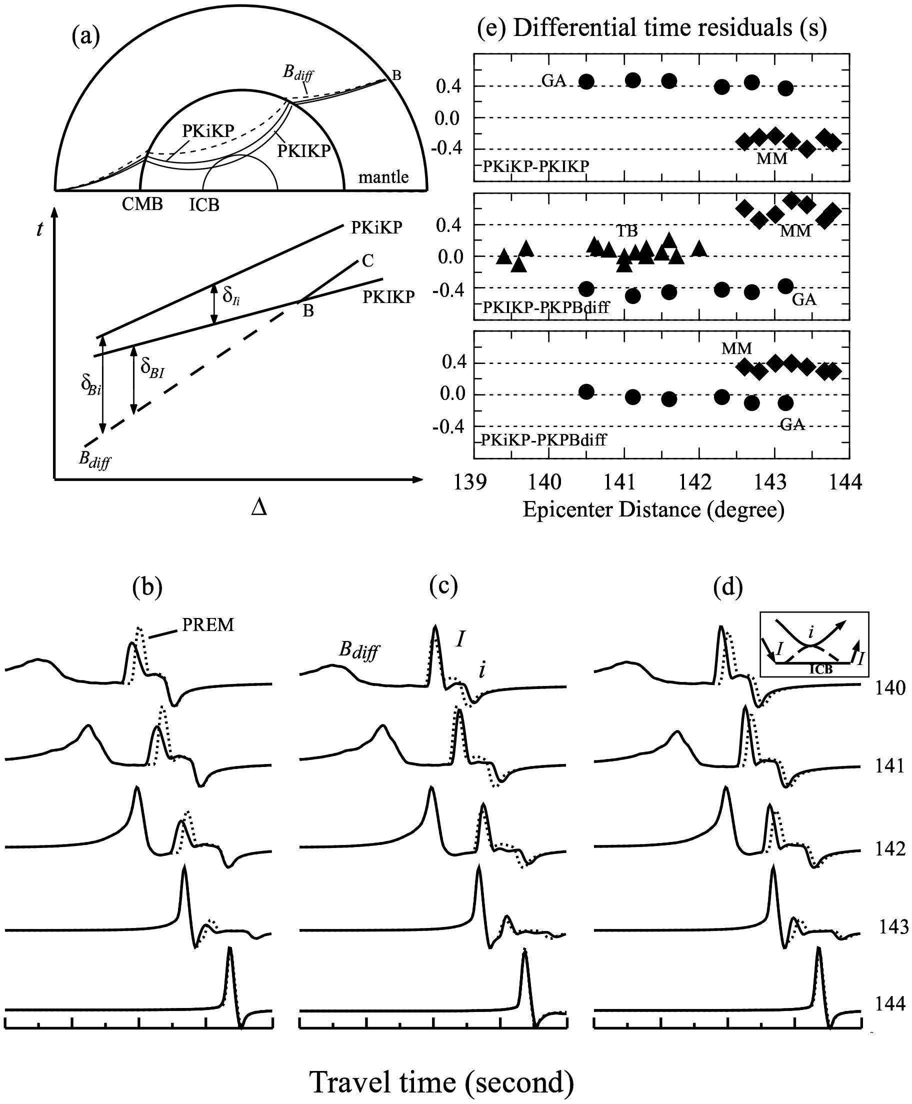

Figure 2.3: (a) Schematic raypaths (upper portion) of PKIKP (I), PKiKP (i) and B_{diff} (non-geometric ray) and travel time curve $t-\Delta$ (lower portion) of PKP near the B caustic. The δ_{iI} is the differential time PKiKP-PKIKP and so on. (b, c, d) Synthetic sections with a focal depth of 600 km using the WKM method [*Ni et al.*, 2000]. Dashed curves are PREM synthetics and solid ones are for modified PREM. Note the δ_{iI} changes when: (b) The P velocity of the top 70 km of the inner-core is increased by 0.8%, (c) The P velocity of the bottom of the fluid core is decreased by 0.9%, and (d) The radius of the inner-core is increased by 15 km. (*insert*) A simulation of laterally varying ICB. If PKIKP and PKiKP hit the ICB at different depth (keeping the piercing points of PKIKP fixed) due to the ICB topography, PKIKP remains the same while PKiKP arrives earlier so that the δ_{iI} decreases. (e) The measurement of the differential time residuals (relative to PREM) in the corresponding record sections as function of epicenter distances. The δ_{iI}'s at GA and MM are typical of those found by *Niu and Wen* [2001].

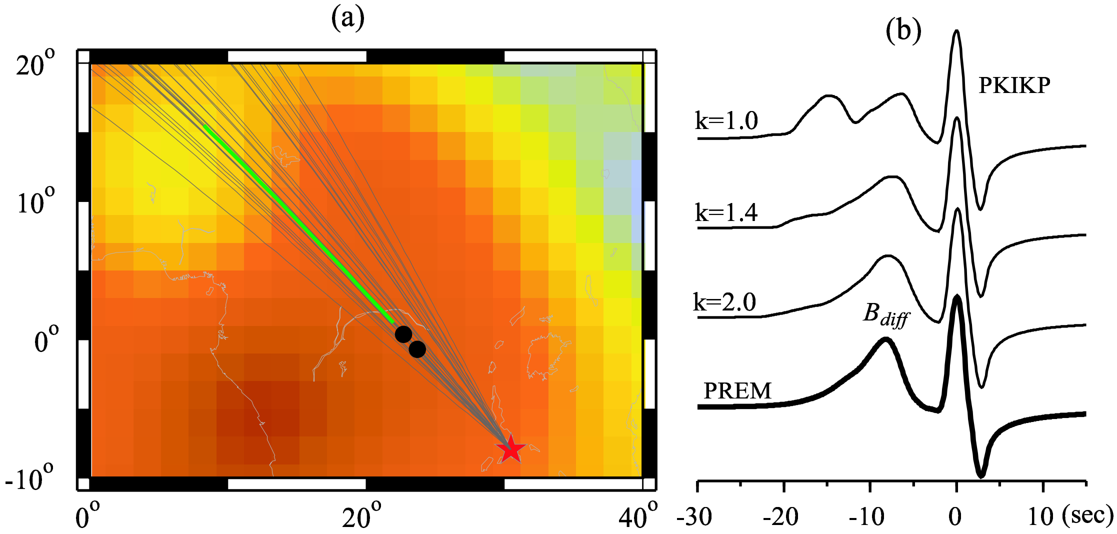

Figure 2.4: (a) Great circle paths for event (20001002) - station (TB) pairs, plotted on an S tomographic model on the source side with a sharp lateral transition at CMB sampled by B_{diff} (green segment). Other notations same as Figure 2.1. (b) 2-D waveform modeling of B_{diff} with different k values along the TB tomographic cross-section at distance of 141°. Note that the distortion of B_{diff} waveform when $k < 2$ caused by the rapid transitions from slow-to-normal structure while the recordings appear PREM-like (Figure 2.2c).

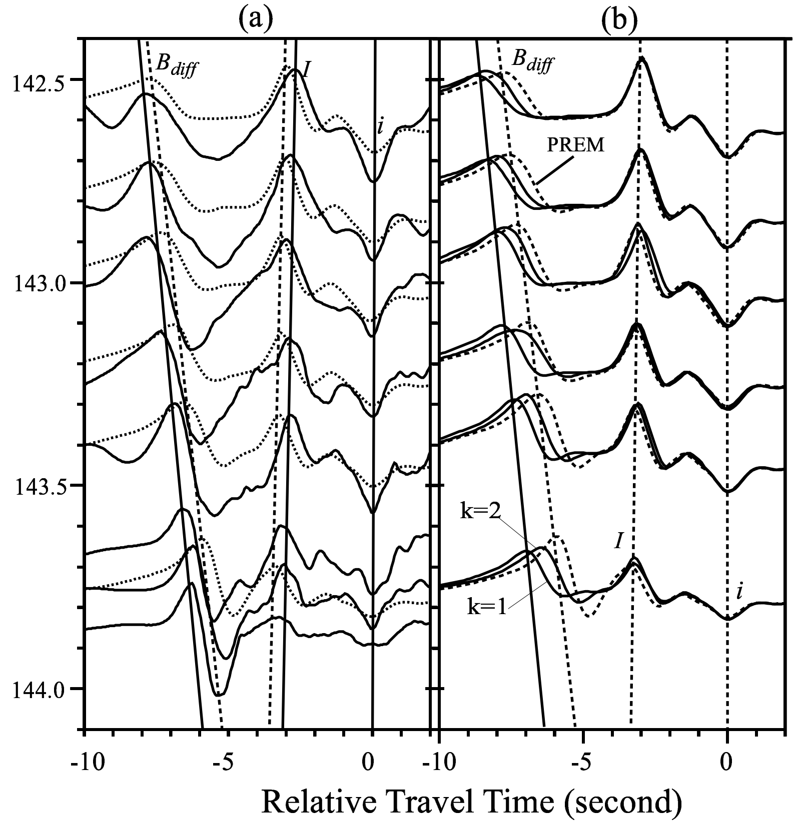

Figure 2.5: (a) Recordings at MM overlaid by PREM synthetics (dotted curve) aligned on PKiKP. These synthetics were produced with a WKM code [*Ni et al.*, 2000]. Solid lines are arrival picks in data and dashed lines PREM arrivals. (b) Dotted curves are PREM synthetics aligned on PKiKP, and solid curves are those from a converted S model [*Grand et al.*, 1997] with $k = 1$ and 2 labeled accordingly. The dashed lines are PREM arrivals and solid line is for $k = 1$.

B_{diff} waveform. The waveform of B_{diff} is fairly simple in the array observations (Figure 2.1) due to its long wavelength nature. To distort B_{diff} requires strong velocity variation over a large scale traversed by the bundle of rays at the lowermost mantle as in Figure 2.4. The entry segment of B_{diff} is distinct in that it crosses a sharp boundary from slow to normal (Figure 2.4a). Numerical experiments on the waveform of B_{diff} were conducted along the tomographic cross section for TB by varying k values (Figure 2.4b). The waveform modeling places lower bound of 2 on k (P velocity jump is less than 2% crossing the boundary) to match the PREM-like waveform as observed in the TB section. Smaller k values (larger P-velocity changes) begin to produce waveform complications as in Figure 2.4b which are not observed (Figure 2.2). In the global study, the cases are statistically rare where most of the B_{diff} segment is in low or ultra-low velocity zone (ULVZ). In other cases where the S variations are small, the P variations are expected to be small too, so that D" will have small effect on B_{diff}-related differential times . Thus it is reasonable to assume a large k. This is consistent with earlier studies where S wave tomographic models can be used to predict large scale P-velocity.

Essentially, the mantle effect on travel time can be estimated by computing travel times from scaled S tomography models. For conceptual purpose, we take MM section as an example to compute the 2-D synthetics and analyze the differential time changes (Figure 2.5). This tomographic model is similar to that shown in Figure 2.1. For MM, the rays mostly sample the fast regions at the CMB and thus the synthetic phases arrive earlier than those from PREM depending on k (Figure 2.5). If $k = 2$, the predicted R_{iB} is about 0.5 s which is similar to the observations. This result suggests that the fluid core is normal (otherwise the fluid core would change i, thus R_{iB}) and the inner-core is slow, favoring the HIC interpretation if no ULVZ's have been sampled by i or I. If $k = 1$, the synthetic δ_{iB} prediction from the tomographic model is over 1 second and PKiKP needs to move forward and thus favors the HOC interpretation.

The analyses for GA is similar except that these paths sample the slow D" and B_{diff} slows down. Since the observed R_{iB} is almost zero, we need to delay i to match the delay of B_{diff} for small k values. For example, $k = 2$ needs to invoke the HOC interpretation since R_{iB} = -0.4 s from the tomographic prediction. But large k values (the P velocity is close to PREM) yield small R_{iB} which suggests a normal fluid core and attribute the R_{iI} to a fast inner-core (HIC). In this case, a large k ($k > 2$) favors the HIC interpretation.

The waveform study places lower bound of 2 on k, comparable to former studies (*e.g.*, $k = 2.5$ [*Robertson and Woodhouse*, 1995]; $k = 2$ [*Dziewonski and Woodhouse*, 1987]). Thus we can constrain that the large-scale P velocity at the lower mantle has small variations. Accordingly, the above travel-time anomalies are readily attributed to the inner-core, thus favor the HIC hypothesis.

2.3 Discussion

The proposed method to interpret δ_{iI} with B_{diff} depends on data quality and availability of broadband data from simple events. To the first order, especially for a global study, constraining interpretation of δ_{iI} with tomographic models is viable. An accurate P tomography model for the lowermost mantle is essential. On the other hand, the differential times involving B_{diff} would help constrain the lowermost mantle. A practical use could be determining the scaling factor (k) between S and P tomographic models.

In this pilot study, we found that B_{diff} waveforms appear to be quite simple and favor large k values with lower bound of 2. Our results from combining these B_{diff} phases with δ_{iI} measurements of broadband array recordings support the HIC hypothesis. Arguments concerning the ICB topography and variations in the outer core seem unlikely as discussed by *Cormier and Choy* [1986] and *Niu and Wen* [2001]. The cause of the δ_{iI} scatter is not clear but could be due to short-wave length structures in D" which usually give rise to PKP precursors.

In conclusion, we found that the top of the inner-core is fast beneath fast D" (Asia) and slow beneath slow D" (Pacific). These lowermost mantle structures could be dynamically related to the structures at the top of the inner-core. One interpretation is that the temperature variations and heat transfer process at the CMB could affect the ICB through some complex dynamics as suggested by *Sumita and Olson* [1999].

Acknowledgements: We acknowledge the efforts of many individuals responsible for the operations of these broadband systems, in particular Jascha Polet for constructing the TRINET data set. S. Ni and D. V. Helmberger contributed partly to this work.

Chapter 3

Direct Shock-Wave Loading of Stishovite to 235 GPa: Implications for Perovskite Stability at the Lower Mantle Conditions

Abstract

Pure stishovite and coesite samples with zero porosity and dimensions appropriate for planar shock wave experiments have been synthesized with multi-anvil high-pressure techniques. The equation of state of stishovite is obtained by direct shock wave loading up to 235 GPa: $K_{0T} = 306 \pm 5$ GPa and $K_{0T}^{'} = 5.0 \pm 0.2$ where K_{0T} is ambient bulk modulus and $K_{0T}^{'}$ is its pressure derivative. The Hugoniots (shock equations of state) for stishovite, coesite and quartz achieve widely differing internal energy states at equal volume and therefore allow us to determine the Grüneisen parameter of stishovite. On the basis of the resulting $P-V-T$ equation of state for stishovite and previous studies on other phases on the MgO-SiO$_2$ binary, the breakdown reaction of MgSiO$_3$-perovskite to MgO and SiO$_2$ was calculated. Our calculations show that perovskite is thermodynamically stable relative to the stishovite and periclase assemblage at lower mantle conditions. We obtain similar results for a range of models, despite the appreciable differences among these experiment-based thermodynamic parameters.

3.1 Introduction

SiO$_2$ is an abundant oxide component of the Earth's mantle, and its thermochemical and mechanical properties are crucial to our understanding of the Earth's deep interior. Although SiO_2 is thought to exist only in compounds with other oxide components in the mantle, the properties of the pure end member are needed to verify the thermodynamic stability of SiO_2-bearing phases. The polymorphs of silica have been the subject of extensive experimental and theoretical studies with various techniques, including *ab initio* and molecular dynamics modeling [*Karki et al.*, 1997; *Luo et al.*, 2002c] and diamond anvil cell (DAC) [*Hemley et al.*, 2000; *Panero et al.*, 2001; *Andrault et al.*, 1998, 2002; *Ono*, 2001] and shock wave experiments [*Wackerle*, 1962; *Al'tshuler et al.*, 1965; *Podurets et al.*, 1981; *Marsh*, 1980; *Furnish and Ito*, 1995]. The high pressure polymorph of silica, stishovite, is particularly important due to its implications for the Earth's lower mantle, and its possible engineering applications as the hardest oxide known [*Leger et al.*, 1996]. Shock wave loading is a unique tool for studying thermal and mechanical properties in that shock-loaded materials are compressed and heated simultaneously. Thus, the equation of state (EOS) and thermal parameters such as, the Grüneisen parameter, can be obtained. A previous effort at direct shock wave loading on stishovite [*Furnish and Ito*, 1995] was undermined by sample impurity and porosity due to the challenges in synthesizing large specimens of stishovite with conventional multi-anvil techniques. Here we report our work on the synthesis and direct shock wave loading of pure polycrystalline stishovite, and the geophysical implications.

3.2 Static synthesis and dynamic loading of coesite and stishovite

To avoid edge effects and ensure accuracy in planar shock-wave measurements with streak camera diagnostics (the camera used can record 80-100 ns shock propagation times with ~1% precision), the minimum required dimensions of a disk-shaped sample are ~1 mm in thickness and ~3 mm in diameter. This presents a challenge for the synthesis of stishovite, which requires pressures above ~10 GPa. Typical dimensions of the recovered sample in multi-anvil cells that reach 10 GPa are ~1.5 mm in diameter [*Rubie*, 1999]. A new technique was adopted to radically simplify the assembly to maximize space: the ZrO_2 insulator, $LaCrO_3$ heater, MgO spacer, and sample capsule typically used in modern multi-anvil experiments were dispensed with and only a Re foil was used as both heating element and sample container. The starting material is a cylinder of pure silica glass. The stishovite samples were synthesized at nominal conditions of 14 GPa and 1000°C using 14 mm sintered MgO octahedra, 8 mm truncation-edge-length tungsten carbide anvils and pyrophyllite gaskets. The recovered samples are well-shaped cylinders with bulk density (ρ_0) of 4.31±0.04 g/cm^3, diameter of ~4 mm and thickness of ~2.5 mm. These samples are pure stishovite with zero porosity as evidenced by density measurement, optical microscopy and X-ray diffraction pattern. A typical synthesized stishovite sample is shown in Figure 3.1. The Hugoniot of coesite shocked into the stishovite regime was previously determined up to 112 GPa [*Podurets et al.*, 1981] and can serve as a reference state for measurements on stishovite if verified and extended to higher pressure. Therefore we also synthesized pure coesite samples for shock-wave loading with a cubic multi-anvil device at approximately 4 GPa and 900°C. The final bulk density (ρ_0) of these samples is 2.92±0.03 g/cm^3. The synthesized coesite and stishovite samples are sectioned into disks of ~1 mm thickness and polished for shock-wave experiments. Planar shock-wave experiments were conducted on a two-stage light gas gun with projectile velocity (u_{fp}) measured by flash X-rays and shock-wave velocity (U_S) by streak camera, from which the particle velocity (u_p), pressure (P) and specific volume (V) at shocked states are determined with the impedance match method [*McQueeen*, 1991]. The results are listed in Table 3.1. Figure 3.2 shows the $U_S - u_p$ relationships for coesite and stishovite. The new coesite data are in agreement with the previous study [*Podurets et al.*, 1981]. A linear fit to both coesite data sets in the high pressure (stishovite or post-stishovite) regime gives

$$U_S(\mathrm{km/s}) = 2.52 + 1.70u_p; \rho_0 = 2.92 \pm 0.03(\mathrm{g/cm^3}) \tag{3.1}$$

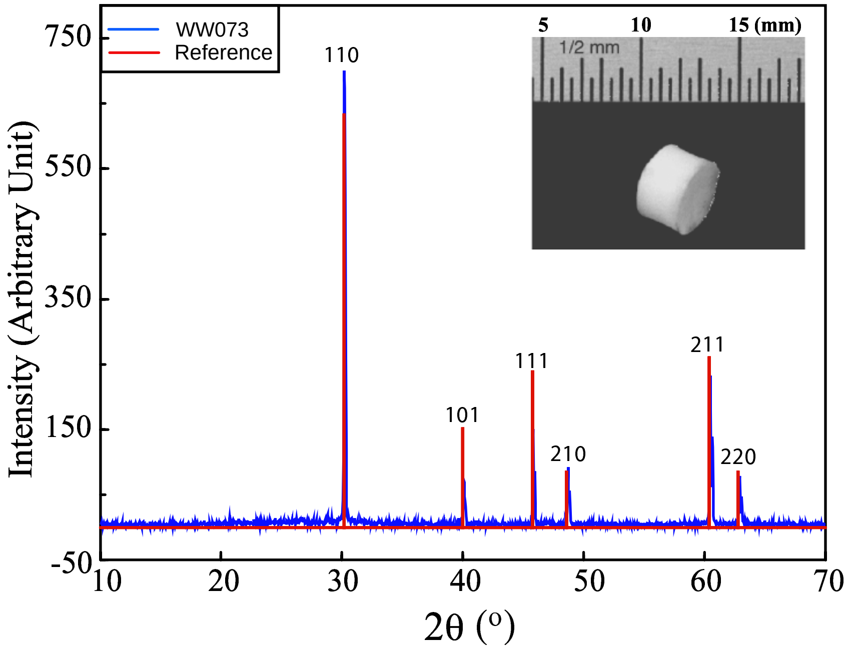

Figure 3.1: A typical stishovite sample (WW073, insert) synthesized using the multi-anvil techniques detailed in the text, with the (hkl) labeled XRD peaks (Cu $K\alpha_1$) matching the reference data (JCPDS-International Center for Diffraction Data, 1992)

A linear fit to the shock-wave data starting from stishovite yields

$$U_S(\mathrm{km/s}) = 9.08 + 1.23u_p;\, \rho_0 = 4.31 \pm 0.04(\mathrm{g/cm^3}) \tag{3.2}$$

Hugoniots centered at stishovite, coesite and quartz are shown in Figure 3.3 (the fused quartz data are scattered and not included). Although post-stishovite phases could have formed on the stishovite principal Hugoniot, we observed no direct evidence for such a transition. This could be due to the pressure range over which we conducted the experiments, sluggish kinetics at low shock temperature resulting from the low compressibility of stishovite, or the relatively small changes in structure and energy attending phase transition. In other words, it could be stishovite or post-stishovite phase on the stishovite Hugoniot. For comparison, it is proposed that a post-stishovite phase exists on the principal quartz and coesite Hugoniots [*Akins and Ahrens*, 2002]. This could be explained by the temperature differences between quartz (or coesite) and stishovite Hugoniots.

Table 3.1: shock-wave experiment parameters for coesite and stishovite. Numbers in parentheses denote uncertainties in the last 1 or 2 digits.

Shot #	Flyer-driver material	u_{fp} (km/s)	ρ_0 (g/cm^3)	U_s (km/s)	u_p (km/s)	P (GPa)	ρ (g/cm^3)
			Stishovite				
329	Ta	6.18	4.33	13.89(15)	3.92(1)	235.7(2.4)	6.03(10)
331	Al1100	5.73	4.26	11.63(12)	2.06(1)	102.2(1.2)	5.18(5)
332	Ta	4.84	4.32	12.76(14)	3.05(1)	168.1(1.7)	5.67(8)
333	Ta	5.36	4.30	13.30(14)	3.38(1)	193.6(2.0)	5.76(9)
			Coesite				
325	Ta	4.99	2.94	8.90(9)	3.78(1)	98.8(1.0)	5.10(11)
329	Ta	6.18	2.91	10.37(12)	4.61(1)	139.3(1.4)	5.24(13)
331	Al1100	5.73	2.94	7.62(7)	2.99(1)	67.0(0.6)	4.84(9)
332	Ta	4.84	2.92	8.82(9)	3.66(1)	94.4(1.0)	4.99(10)

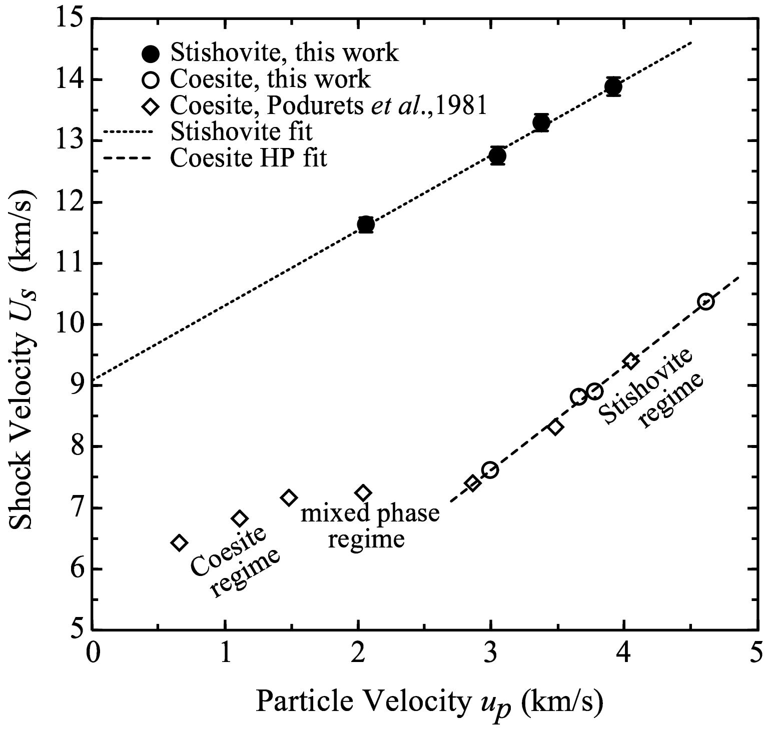

Figure 3.2: Planar shock-wave experiments on coesite and stishovite. Stishovite experiments were conducted at high pressures above the Hugoniot elastic limit. The $U_S - u_p$ relationships are shown as dotted line for stishovite and dashed line for coesite in high pressure (HP) regime.

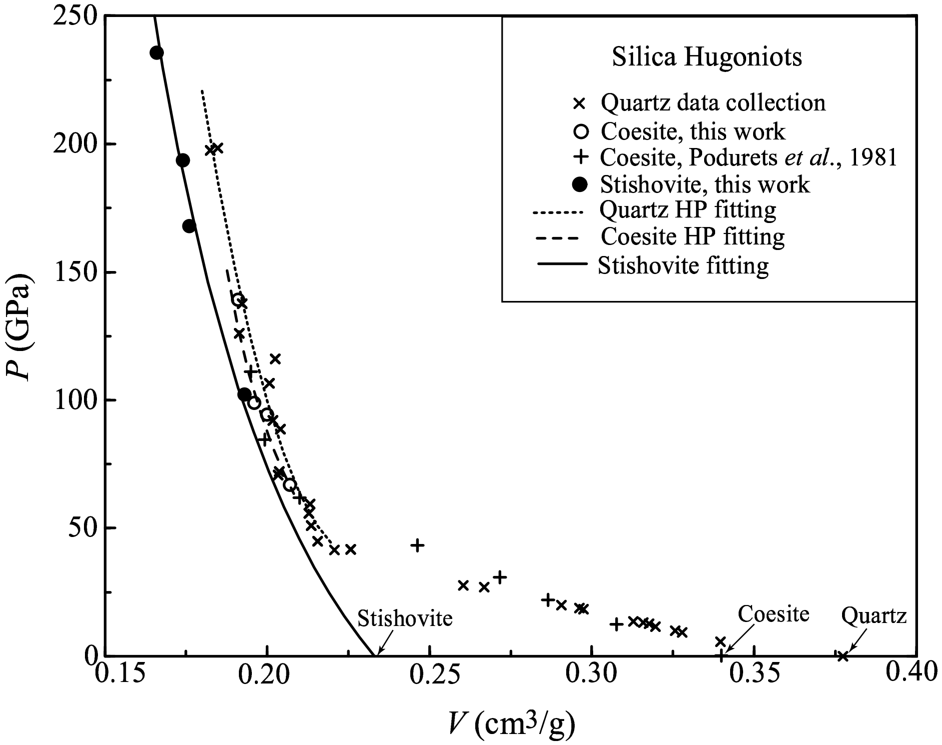

Figure 3.3: shock-wave data of silica in $P-V$ space. Quartz data are from [*Wackerle*, 1962; *Al'tshuler et al.*, 1965; *Marsh*, 1980]. Hugoniots for quartz, coesite and stishovite have initial density of 2.65, 2.92 and 4.31 g/cm^3 respectively.

At high pressures, where all three Hugoniots are in the stishovite-type phase, the internal energy and pressure differences at fixed volume allow estimation of the Grüneisen parameter (γ) of stishovite by finite difference, assuming the Mie-Grüneisen equation of state, *i.e.*, $\gamma = V(\partial P/\partial E)_V$, where E is internal energy. The Hugoniots in the stishovite/post-stishovite regime for quartz and coesite are obtained by fitting to the available data (Figure 3.4). The Grüneisen parameter for stishovite, $\gamma(V)$, is obtained from the quartz-stishovite and coesite-stishovite Hugoniot pairs. Fitting to

$$\gamma = \gamma_0 (V/V_0)^q; \gamma_0 = 1.35 \tag{3.3}$$

yields $q = 2.6 \pm 0.2$, where V_0 is the ambient specific volume and γ_0 the ambient Grüneisen parameter [*Watanabe*, 1982]. The functional form of $\gamma(V)$ follows *Anderson* [1995] and *McQueeen* [1991]. In the absence of experimental constraints it is common to assume $q = 1$. The Grüneisen parameter of stishovite at lower mantle conditions has not previously been determined from experiments. Thus, our result obtained directly from shock-wave experiments provides an important constraint on thermodynamic calculations and geotherm modeling [*Stacey*, 1992]. The Grüneisen parameter of stishovite also allows the determination of the Anderson-Grüneisen parameter as $\delta_T = 6.6$ (given K'_{0T} determined next), which provides a basis for extrapolation of thermal expansivity of stishovite to high pressures [*Anderson*, 1995; *Birch*, 1952].

To construct the equation of state of stishovite to high pressures, we correct the shock-wave data to a 300 K isotherm by subtracting the thermal pressure from the shocked state at fixed volume. This pressure correction is obtained by calculating the temperatures along the Hugoniot and the pressure difference between the Hugoniot and 300 K isotherm assuming the Mie-Grüneisen equation of state [*McQueeen*, 1991], given our new value for the Grüneisen parameter. Figure 3.4 shows the 300 K isotherm obtained by jointly fitting the corrected shock-wave data and recent lower pressure DAC data [*Hemley et al.*, 2000; *Panero et al.*, 2001; *Andrault et al.*, 2002] to the Vinet equation of state [*Vinet et al.*, 1989]. The fit yields $K_{0T} = 306 \pm 5$ GPa and $K'_{0T} =$

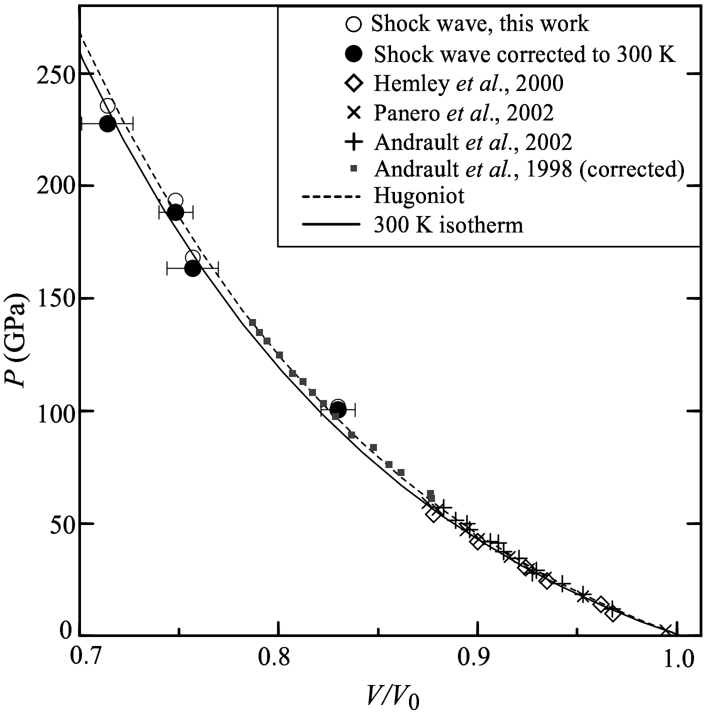

Figure 3.4: The 300 K isotherm and Hugoniot of stishovite at 0 - 250 GPa. Solid curve is the Vinet universal EOS fit to the corrected shock-wave data and low pressure DAC data at 300 K [*Hemley et al.*, 2000; *Panero et al.*, 2001; *Andrault et al.*, 2002]. The data in *Andrault et al.* [1998] were corrected in *Andrault et al.* [2002]. The shock data points on the Hugoniot and on the isotherm have the same error bars in volume, and the pressure error bars are within the symbol size.

5.0±0.2 in the range of 0-250 GPa, comparable to previous studies at lower pressures [*Panero et al.*, 2001; *Andrault et al.*, 2002; *Li et al.*, 1996]. Although a previous study on stishovite [*Andrault et al.*, 1998] proposed an appreciably denser and softer stishovite EOS up to 120 GPa, the data have been revised and reinterpreted along with the new data below 60 GPa [*Andrault et al.*, 2002]. Given the uncertainties in pressure calibration in DAC and those in volume determination in shock-wave experiments, all these data sets are in reasonable agreement (Figure 3.4).

3.3 Discussion and conclusion

The breakdown of $MgSiO_3$-perovskite at lower mantle conditions has been a subject of extensive investigation and debate [*Meade et al.*, 1995; *Saxena et al.*, 1996; *Serghiou et al.*, 1998; *Mao et al.*, 1997; *Shim et al.*, 2001]. We tackled this issue based on the Gibbs free energy of perovskite relative to that of the assemblage of periclase and stishovite. As previous studies did not predict dramatic structural and energetic changes of perovskite and stishovite under lower mantle conditions, we assume that perovskite as well as stishovite can be described with a single set of EOS and thermodynamic parameters. Our new results for stishovite, along with recent studies on $MgSiO_3$-perovskite [*Saxena et al.*, 1999], allow a more precise calculation of phase equilibria of the perovskite (denoted as Pv), periclase (Pe) and stishovite (St) system, *i.e.*, the Gibbs free energy and volume of the reaction

$$\mathrm{MgSiO_3\ (Pv) \leftrightarrow MgO\ (Pe) + SiO_2\ (St)}$$

The thermodynamic parameters we used are from *Fei et al.* [1990] and *Fei* [1995] unless stated otherwise. Using our new results on stishovite and a recent study on $MgSiO_3$-perovskite (model 1 in *Saxena et al.* [1999]) (denoted as Model 1), we computed the Gibbs free energy and specific volume for each phase at 300-3700 K and 0-150 GPa, from which the Gibbs free energy and volume of reactions (ΔG and ΔV respectively) were obtained. We adopted a widely used method to compute these reactions (*e.g.*, *Song and Ahrens* [1994]). Figure 3.5a shows that for 300-3700

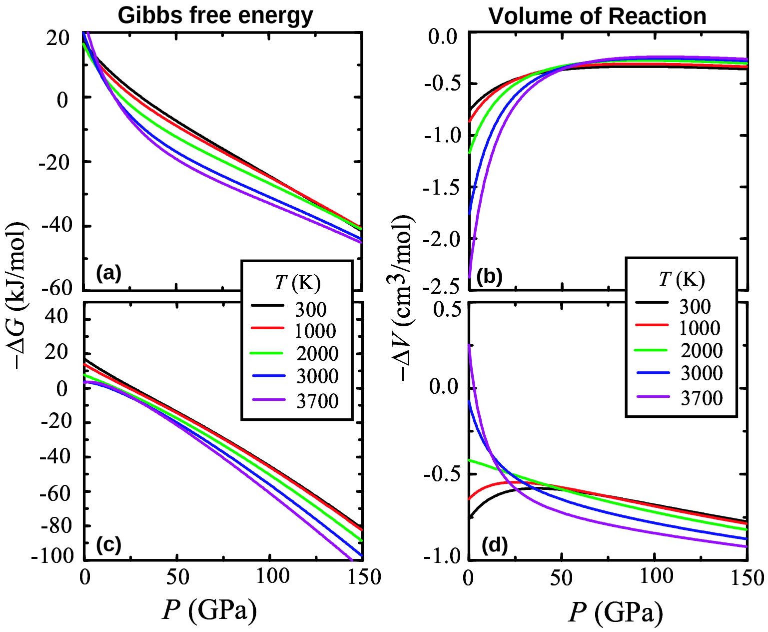

Figure 3.5: Gibbs free energy and volume of reaction Pv = Pe + St for Model 1 (a, b) and Model 2 (c, d).

K isotherms, perovskite has lower Gibbs free energy than the assemblage of stishovite and periclase at pressures higher than 25-31.5 GPa. Thus for any reasonable geotherm [*Brown and Shankland*, 1981], perovskite is thermodynamically stable relative to the assemblage of stishovite and periclase at lower mantle pressures. Besides the lower Gibbs free energy, perovskite also has smaller molar volume than the Pe-St assemblage by 0.5 cm^3/mol (Figure 3.5b), *i.e.*, perovskite is about 2% denser than its oxide counterparts at lower mantle conditions. This implies that the relative stability of $MgSiO_3$-perovskite increases to higher pressures.

To explore the sensitivity of this calculation to the choice of thermodynamic parameters, we conducted similar calculations with alternative parameters for St and Pv. The parameters of Model 2 (*i.e.*, not using our EOS and δ_T for stishovite) from *Fei et al.* [1990] and *Fei* [1995] yielded results as shown in Figure 3.5c-d. We conclude that Pv is stable with respect to the assemblage of St and Pe. We also examined Model 3 (*Andrault et al.* [1998] for St and *Fei et al.* [1990] for Pv), Model 4 (this work for St and *Fei et al.* [1990] for Pv) and Model 5 (this work for St and model 2 in

Saxena et al. [1999] for Pv). All these models predict similar results. This is significant if we consider the appreciable differences among the parameters in the reported different models, such as K_0, $K^{'}_{0T}$, δ_T, thermal expansivity and specific heat, *e.g.*, for stishovite, K_T varies from 291 to 314 GPa and $K^{'}_{0T}$ from 4.3 to 6. Although it was shown that the decomposition of perovskite is possible if the EOS parameters of stishovite are chosen specifically to obtain this result with $K^{'}_{0T} < 3.5$ [*Pankov et al.*, 1996], the present experimental results exclude this possibility. Our calculations apply strictly only to the rutile structure of SiO_2 and orthorhombic structure of $MgSiO_3$ at depths of 670-2300 km [*Ono*, 2001; *Shim et al.*, 2001], but a large ΔG accumulates over their stability regime. Hence, although both stishovite [*Hemley et al.*, 2000; *Andrault et al.*, 2002] and perovskite [*Shim et al.*, 2001] phases may invert to slightly denser forms in the lowermost mantle, we do not expect the oxides to become stable relative to $MgSiO_3$ phases within the mantle pressure regime (*i.e.*, up to 136 GPa).

Detailed investigation of the stability of perovskite relative to the oxide assemblage in the real lower mantle requires consideration of the influence of other components; most importantly Fe, FeO, CaO and Al_2O_3. CaO enters the separate phase Ca-perovskite. Al_2O_3 substitutes into Mg-perovskite and expands its stability field relative to Pe and St. Although FeO substitutes into both Pe and Pv and can shift the equilibrium either way, a recent study did not observe different behavior of $(Mg_{0.9}Fe_{0.1})SiO_3$ perovskite at lower mantle conditions [*Shim et al.*, 2001]. At the core-mantle boundary (as opposed to within the bulk of the lower mantle), the involvement of metallic Fe in the reaction of (Mg, Fe)-perovskite, magnesiowüstite and stishovite-type phases could induce the decomposition of (Mg, Fe)-perovskite to mixed oxides and the sequestration of Fe into the outer core [*Song and Ahrens*, 1994]. These reactions could be expected to contribute to the anomalous seismic observations in the D" region [*Knittle and Jeanloz*, 1991]. In natural multicomponent assemblages, however, stishovite and its higher pressure $CaCl_2$ and α-PbO_2 forms remain essentially pure SiO_2, so experiments on the EOS and thermal properties of SiO_2 remain directly relevant to calculating stability relations in the presence of other components. Unless experiments reveal dramatically different thermochemical and mechanical parameters for the poorly known higher pressure polymorphs, we expect the thermodynamic stability of perovskite or its related structures relative to the oxide assemblage through the lower mantle except at the core-mantle boundary.

Acknowledegment: We appreciate the professional technical support by M. Long, P. Gelle and C. McCaughey. J. L. Mosenfelder, P. D. Asimow and T. J. Ahrens contributed partly to this work.

Chapter 4

Molecular Dynamics Modeling of Stishovite

Abstract

A Morse-stretch potential charge equilibrium force field (MS-Q FF) for silica system has been employed to simulate the thermodynamics of stishovite with molecular dynamics (MD) method. The equation of state (EOS), thermal expansivity and melting curve of stishovite have been obtained. This simple force field yielded results in accord with the static and dynamic experiments. The stishovite melting simulation appears to validate the interpretation of superheating of the solid along the Hugoniot in the shock melting experiments. MD simulations show that the thermal expansivity of stishovite at lowermost mantle conditions is a weak function of temperature. The phase diagram of silica up to mega bar regime is proposed based on the experimental and theoretical studies. The related physical and geophysical implications are addressed.

4.1 Introduction

Silica is important not only as a main constituent of the Earth and other terrestrial planets but also as a model system to study the fundamental physics of material properties, such as phase changes and interatomic potentials. Stishovite-type phase is geophysically important due to its wide range of stability in the mantle, the possible chemical reactions of silicates with liquid Fe at the core-mantle boundary (CMB) [*Knittle and Jeanloz*, 1991] and its presence in impact craters [*Chao et al.*, 1962] and meteorites [*ElGoresy et al.*, 2000]. To interpret the seismic structure of the Earth in terms of chemical composition, and understand the transport processes (*e.g.*, heat and mass) associated with the issues such as Earth dynamics and evolution, the knowledge of thermodynamics of SiO_2 as an end number of the MgO-SiO_2 system is crucial. Various experimental studies such as diamond-anvil cell (DAC) and shock wave experiments have shown that silica undergoes polymorphic phase changes and amorphization when subjected to high pressure (P) and temperature (T) [*Hemley et al.*, 1994], but its properties at P, T conditions of the Earth's interior and during impact are not well constrained. Complementary to experiments, first-principle and molecular dynamics (MD) methods have been applied to the silica system (*e.g.*, *Cohen* [1994]; *Belonoshko and Dubrovinsky* [1995]; *Karki et al.* [1997]), while the latter has the advantage to handle longer dynamic simulations and larger system sizes required by processes such as phase changes. One interesting challenge in MD modeling is to develop simple theories that accurately describe interatomic interactions and hence material properties. The Morse-stretch potential charge equilibrium force field (MS-Q FF) has been developed to predict the phase changes in ionic insulators such as minerals and ceramics. The proposed MS-Q FF for silica system describes both the 4-fold and 6-fold coordinated systems, silica glass and pressure-induced phase changes [*Demiralp et al.*, 1999]. In this paper, we will apply the MS-Q FF for silica to simulate the equation of state, thermal expansivity and melting of stishovite and discuss the possible physical and geophysical implications.

4.2 MD simulation method

Molecular dynamics methods utilize a parameterized analytical force field obtained by fitting to either experimental or first-principle results, from which the atomic motions are calculated from Newtonian physics and thermodynamic properties from statistical mechanics [*Cygan*, 2001; *Allen and Tildesley*, 1987; *Frenkel and Smit*, 1996; *Strachan et al.*, 1999]. Various potentials for SiO_2 system have been proposed (e.g., *Belonoshko and Dubrovinsky* [1995]) and cross-checking is necessary. The application of MS-Q FF to silica describes well the general behavior of SiO_2 system [*Demiralp et al.*, 1999] despite of its simplicity. The MS-Q FF includes nonelectrostatic (Morse-stretch potential) and electrostatic (evaluated from instantaneous charge equilibrium) contributions.

The nonelectrostatic interactions are represented by a simple two-body Morse-stretch (MS) potential

$$U_{ij}^{MS}(R_{ij}) = D_0[e^{-\gamma(1-R_{ij}/R_0)} - 2e^{\frac{\gamma}{2}(1-R_{ij}/R_0)}] \tag{4.1}$$

where R_{ij} is the interatomic distance and the MS parameters D_0, R_0 and γ for Si-Si, O-O and Si-O were optimized from experimental results and listed in Table 4.1. The electrostatic contribution to force field is evaluated from the charges on the atoms of the instantaneous configuration, *i.e.*, the charges are not fixed during dynamics. For different geometric configuration, the charge equilibrium (QEq) procedure is applied to compute charges by requiring that the chemical potential χ_A be equal on all A atoms (similar for B) [*Demiralp et al.*, 1999; *Rappe and Goddard*, 1991]. χ_A is a function of the charges (Q_i) on all the atoms of the system and the distance R_{AB} between A and B:

$$\chi_A(Q_1, ..., Q_N) = \chi_A^0 + J_{AA}^0 Q_A + \sum_{B \neq A} J_{AB}(R_{AB}) Q_B \tag{4.2}$$

and $J_{AB}(R)$ is described as a shielded Coulomb potential for a normalized ns Slater orbital with the orbital exponent given by R_A and R_B, the atomic radii at the standard state [*Rappe and Goddard*, 1991]. The atomic parameters χ^0, J^0, R_A and R_B for Si and O are listed in Table 4.1. Thus, the electrostatic contribution can be evaluated from the charges by QEq procedure at each time step of the dynamics.

Given the MS-Q FF, classical molecular dynamics can be employed to simulate the mechanical and thermodynamic properties of materials subjected to various P and T with different statistical ensembles [*Frenkel and Smit*, 1996].

Table 4.1: MS-Q force field parameters for SiO_2 [*Demiralp et al.*, 1999]

Morse-Stretch parameters:	R_0(Å)	D_0 (kcal/mol)	γ
O-O	3.7835	0.5363	10.4112
Si-Si	3.4103	0.2956	11.7139
Si-O	1.6148	45.9970	8.8022
QEq parameters for O and Si:	χ^0 (eV)	J^0 (eV)	R (Å)
O	8.741	13.364	0.669
Si	4.168	6.974	1.176

4.3 Simulation results

4.3.1 Equation of state of stishovite

The isothermal equation of state for stishovite is calculated with isothermal-isobaric MD (NPT ensemble) with a Hoover thermostat [*Hoover*, 1985] and a Rahman-Parinello barostat [*Parrinello and Rahman*, 1981]. In NPT MD simulations, the Coulombic interactions were evaluated using Ewald summation with real space cutoffs 5-8 Å and reciprocal space cutoffs 0.8-0.5 1/Å while the Morse interactions were truncated at R=0.9 Å. The integration time step was 1 fs. As pointed out before, the atomic charges depend on the instantaneous configuration of the system and were updated every 50 time steps. For 300 K isotherm, we conducted a continuous NPT run with progressive pressure increase on a super-cell of 672 atoms ($4 \times 4 \times 7 = 112$ unit cells) with 3-D periodic boundaries. The loading rate is 0.25 GPa/ps in the range of 0-100 GPa and 1 GPa/ps in the range of 100-220 GPa. For a 20-ps run at each pressure, the first 6 ps were taken as thermalization and the remaining 14 ps for statistical averages of lattice parameters and volume. The results are shown in Figure 4.1. At given P, the density difference between MD and DAC results [*Hemley et al.*, 2000; *Panero et al.*, 2001] up to 55 GPa is within 1%. The MD simulation points were fitted to Vinet universal EOS [*Vinet et al.*, 1989; *Cohen et al.*, 2000]

$$P(x) = 3K_{T0}(1-x)x^{-2}exp[\frac{3}{2}(K'_{T0}-1)(1-x)] \tag{4.3}$$

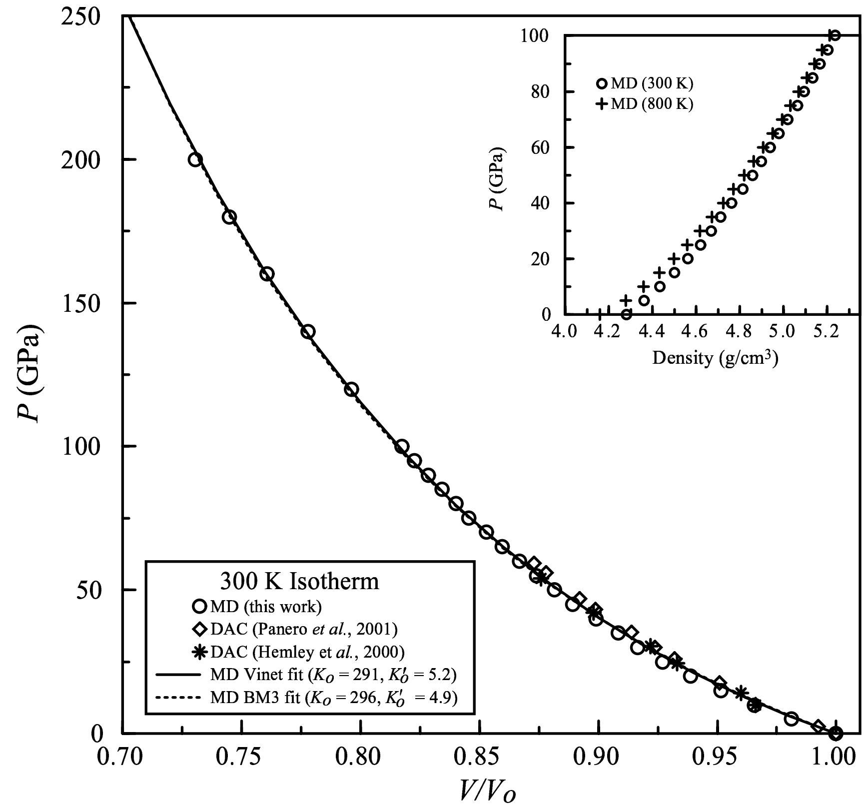

Figure 4.1: The 300 K isotherms of stishovite from NPT MD simulation and diamond-anvil cell (DAC) experiment. V_0 is the ambient specific volume (46.61 Å^3 per unit cell). The MD results are fitted to Vinet EOS (K_{T0}=291 GPa and K'_{T0}=5.2) and the 3rd order Birch-Murnagham EOS (BM3, K_{T0}=296 GPa and K'_{T0}=4.9). (*insert*) The 300 K and 800 K isotherms from MD simulations.

and the 3rd order Birch-Murnagham (BM3) EOS [*Birch*, 1978]

$$P(f) = 3K_{T0}f(1+2f)^{\frac{5}{2}}[1+\frac{3}{2}(K'_{T0}-4)f] \tag{4.4}$$

where P is pressure, the Eulerian strain $f = \frac{1}{2}[(V/V_0)^{-2/3}-1]$, $x = (V/V_0)^{1/3}$, V_0, K_{T0} and K'_{T0} are the ambient volume, isothermal bulk modulus and its pressure derivative. The values of K_{T0} and K'_{T0} fitted to Vinet EOS and BM3 EOS are very similar and close to experimental results (Table 4.2). Similarly, the 800 K isotherm is also obtained (Figure 4.1 insert and Table 4.2) and we can see the softening of the bulk modulus when T is increased from 300 K to 800 K.

We calculated the elastic constants C_{ij} of stishovite with the MS-Q FF using

Table 4.2: EOS parameters for stishovite ($P = 0$).(a) Vinet fit; (b) BM3 fit; (c) *Weidner et al.* [1982]; (d) Equivalent volume converted from reported density; (e) *Li et al.* [1996]; (f) *Panero et al.* [2001]; (g) *Hemley et al.* [1994] and references therein; (h) Corrected to 300 K, *Luo et al.* [2002d].

	V_0 (Å^3)	K_{T0} (GPa)	K'_{T0}
This work, 300 K	46.611	291.1±3.2^a; 296.4±3.7^b	5.2±0.1^a; 4.9±0.1^b
This work, 800 K	47.987	222.0±3.8^a; 225.6±4.4^b	6.1±0.2^a; 5.8±0.2^b
Brillouin scat.^{c}, 300 K	46.581^d	313±4	-
Ultrasonic^e, 300 K	-	305±5	5.3±0.1
DAC^f, 300 K	-	312.9±3.4	4.8±0.2
DAC^g, 300 K	46.615	298±8	3.98±0.46
Shock wave^h	46.366	306±5	5.0±0.2

Table 4.3: Elastic constants of stishovite ($P = 0$). † *Karki et al.* [1997]; ‡ *Weidner et al.* [1982].

C_{ij} (GPa)	This Work	*ab initio*†	Brillouin scattering‡
C_{11}	478.7	462	453±4
C_{33}	748.0	734	776±5
C_{44}	208.6	255	252±2
C_{66}	157.9	324	302±3
C_{12}	135.9	210	211±5
C_{13}	220.2	195	203±4
K	306.2	312	316±4
μ	191.5	226	220±3

analytical second derivatives of the energy with respect to strain at zero temperature and pressure. Table 4.3 compares our calculated values with *ab initio* [*Karki et al.*, 1997] and experimental results [*Weidner et al.*, 1982]. The C_{ij}'s from the MS-Q force field, *ab initio* calculations and Brillouin scattering are in reasonable agreement. The bulk modulus (K) and shear modulus (μ) were obtained from the stiffness and compliance matrices with Voigt-Reuss-Hill method *Hill* [1952].

From Figure 4.1, Tables 4.2 and 4.3, we can see that the MS-Q force field for silica accurately predicts the equation of state of stishovite.

4.3.2 Thermal expansivity of stishovite

While the direct measurement of thermal expansivity is nontrivial, thermal expansivity α can becalculated from MD simulations. To calculate $\alpha(P)$, we performed NPT MD simulations at $P = 0$ GPa and $P = 120$ GPa, the latter pressure chosen to address the lowermost mantle conditions. The system size is 672 atoms and the heating rate is 2 K/ps. For each T, the first 5 ps were used for thermalization and the last 20 ps for calculating the statistical average of lattice parameters. The linear (α_l) and volume expansivity (α_v) can be computed with

$$\alpha_X = \frac{1}{X}\frac{\partial X}{\partial T}|_P \tag{4.5}$$

where X is either a lattice parameter or volume (V).

Figure 4.2a shows the lattice parameters along $P = 0$ isobar from MD simulations as well as experimental data for comparison. While the lattice parameter c from MD is slightly smaller than that from the experiment, the corresponding linear expansivities (α_c) agree. Along a and b axis, MD simulations yielded larger lattice parameters and linear expansivities. Hence, there is a factor of 2 difference in the volume thermal expansivity for P=0 at 300 K between MD simulation and experiments, and larger at higher temperatures (Figure 4.2b). This could be due to the overestimated anharmonicity in the force field, or the experimental uncertainties caused by the metastability of stishovite at zero pressure. Similarly, the volume thermal expansivity at $P = 120$ GPa is obtained as a weak function of temperature (Figure 4.2c). At higher pressures, the anharmonicity is less pronounced and the estimation of α_V at $P = 120$ GPa is reasonable.

4.3.3 The melting curve of stishovite

Stishovite melting at high pressures has been investigated with techniques such as shock temperature measurements [*Lyzenga et al.*, 1983] and diamond-anvil cell experiments [*Shen and Lazor*, 1995]. It is still challenging to determine the phase

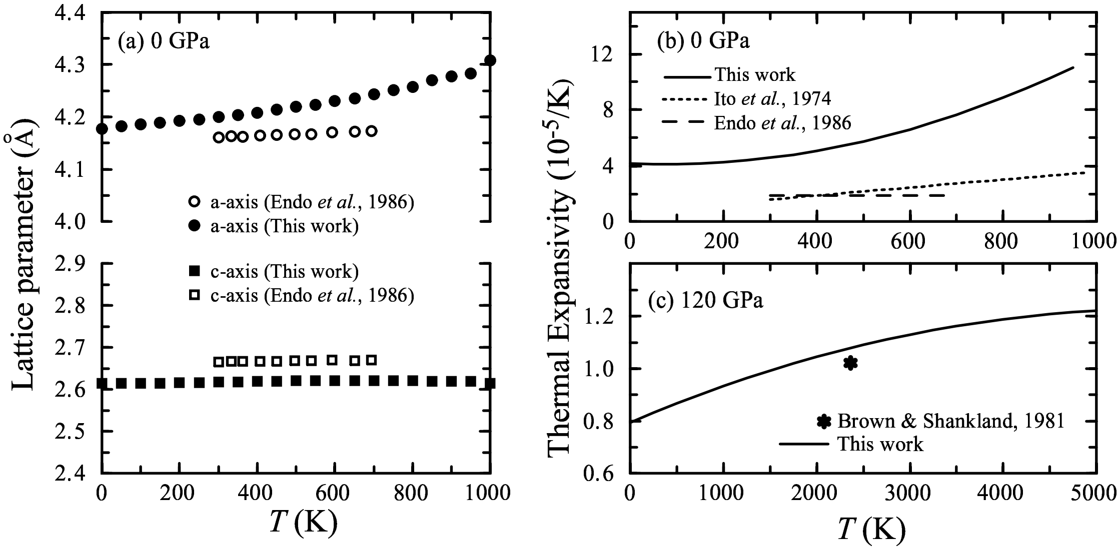

Figure 4.2: (a) Comparison of stishovite lattice parameter as a function of T from MD (this work) with experimental work at 0 GPa [*Endo et al.*, 1986]. (b) The volume thermal expansivity of stishovite at 0 GPa from this work and experiments [*Endo et al.*, 1986; *Ito et al.*, 1974]. (c) The volume thermal expansivity of stishovite at 120 GPa from this work and the calculations for the lower mantle based on seismic observations (asterisk, *Brown and Shankland* [1981]).

diagram at high pressures from static and dynamic experiments. Complementary to experiments, molecular dynamics simulations have been employed to tackle this issue [*Belonoshko and Dubrovinsky*, 1995] but uncertainties remain. Accurate determination of a phase boundary by MD simulations is non-trivial. There are several methods employed to serve this end: single- and two-phase methods [*Belonoshko and Dubrovinsky*, 1995; *Morris et al.*, 1994], the thermodynamic integration method [*Frenkel and Smit*, 1996] and integration of the Clausius-Clapeyron equation [*Strachan et al.*, 1999]. Each method has its own disadvantages and advantages. In this study, we will explore single- and two-phase simulations.

Continuous MD single-phase simulations were conducted on a system of 112 unit cells (672 atoms) with NPT ensemble at different pressures. For each run, the 3-D periodic boundary conditions were applied. The heating and cooling rates were in the range of 12.5−40 K/ps with finer rates at high temperatures. The run time is 20 ps and volume is obtained from the last 15 ps of the single-phase dynamics. Figure 4.3 is

Table 4.4: Melting point of stishovite. ◇ Two-phase simulation; † Single-phase simulation, with uncertainties between 250-500 K; ‡ Calculated from single-phase simulation.

P (GPa)	$T_m^\diamond$ (K)	$T_m^\dagger$ (K)	$\Delta H^\ddagger$ (eV)	$\Delta V^\ddagger$ (Å^3)	$dT/dP^\ddagger$ (K/GPa)
20	3125±125	3625	3.20	7.3901	50.5
40	4125±125	4500	3.51	4.2025	33.6
60	4625±125	5500	3.34	2.4743	25.4
80	4900±125	6000	3.16	1.4176	16.8
120	5437.5±75	7000	3.52	0.7523	9.3

a typical example ($P = 120$ GPa) of single-phase simulation. The volume per unit cell increases steadily during heating until 7000 K, where a sharp increase of the slope (dV/dT) occurs, indicating the initiation of melting, *i.e.*, the melting temperature T_m at 120 GPa is 7000 K. Above 7500 K, the liquid volume increases steadily. The cooling of the system from 8000 K is conducted at the same rate as the heating. The heating-cooling is reversible above 7500 K. Below 7500 K, the hysteresis effect appears: The liquid doesn't solidify, instead, decreases its volume steadily. The liquid could crystallize eventually at lower temperatures and thus a hysteresis loop may form. The corresponding enthalpy of the same system during the heating-cooling process is shown in Figure 4.3b, where a similar hysteresis effect is observed as expected. The slope of the melting curve at certain pressure, dT/dP, can be obtained from the differences of specific volume (V) and enthalpy (H) between solid and liquid at temperatures near T_m using the Clausius-Clapeyron equation:

$$\frac{dT}{dP} = \frac{T\Delta V}{\Delta H}. \tag{4.6}$$

By repeating the same procedure at different pressures, we obtained the melting point and the melting curve slope (dT/dP) at pressures 20-120 GPa from single-phase simulation (Table 4.4). Decreasing dT/dP indicates that the melting curve flattens with the increasing pressure.

Single-phase simulation could lead to hysteresis effect as in Figure 4.3, *i.e.*, superheating of solid and undercooling of liquid due to the existence of kinetics during the

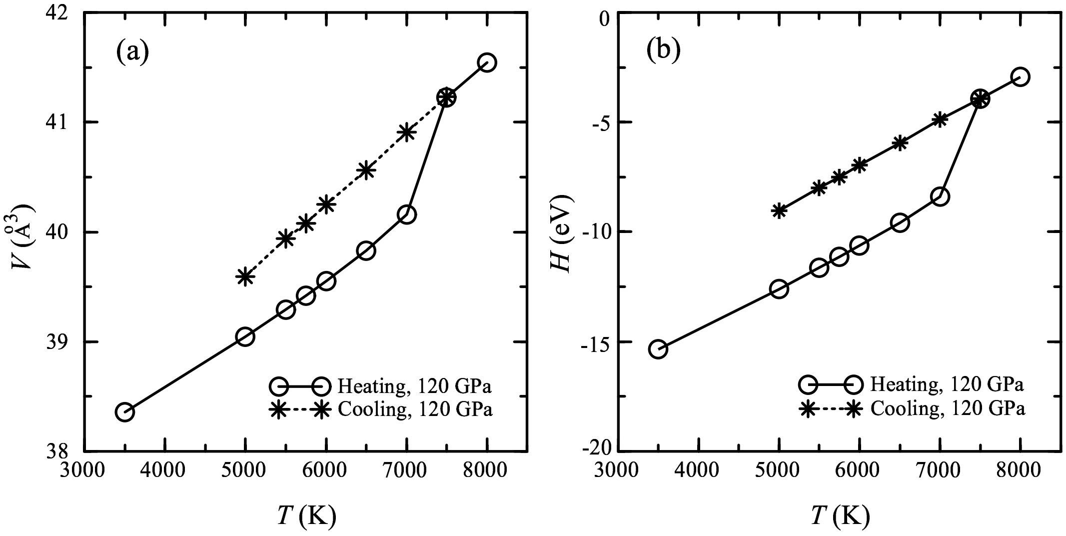

Figure 4.3: Single-phase simulations of stishovite melting at 120 GPa. (a) The unit cell (2 SiO_2 formulae) volume (V) and (b) the corresponding enthalpy (H) during the heating-cooling process.

simulation [*Allen and Tildesley*, 1987; *Strachan et al.*, 1999], especially at high pressures. Thus, the melting point T_m could be overestimated seriously at high pressures we are interested in. The superheating could be circumvented by the thermodynamic integration method [*Frenkel and Smit*, 1996] or two-phase simulation technique [*Belonoshko and Dubrovinsky*, 1995; *Morris et al.*, 1994]. The latter is simpler in physics as well as in computation and widely used. The two-phase simulation models are constructed by combining the solid and liquid models at the same pressure and temperature from the single-phase simulations. Nucleation could be a problem if one tries to crystallize (or melt) the single-phase liquid (or solid), but the two-phase simulation has the advantage that the planar initial solid-liquid interface corresponds to an infinite nucleation, much larger than the required critical radius.

To construct the starting model for the two-phase simulation, stishovite liquid and solid models at the same P and T from the single-phase simulations were placed into a supercell with 3-D periodic boundaries. The system size is 672×2 atoms, twice that for single-phase simulations. One concern in combining solid and liquid models is the solid-liquid interface: While the total free energy of the two-phase system should be minimum, the internal pressure should remain unchanged when adjusting the interface thickness to minimize the energy. The tradeoff between interface thickness and the corresponding internal pressure changes complicates the simulation: The internal pressure could vary by appreciable amount with the interface thickness thus the melting temperature could be over- or underestimated if the pressure change is not relaxed. When constructing the two-phase model, the interface thickness was adjusted to keep internal pressure equal to the nominal pressure. This issue could be bypassed with a larger system.

With the two-phase model constructed at certain temperature and fixed pressure, NPT MD runs were conducted to bracket the melting point by varying T. If the temperature is higher than the melting temperature, T_m, the two-phase system should become liquid eventually and the opposite when $T < T_m$. If the NPT run is conducted at T_m, the system should remain unchanged. Thus the melting point is bracketed. There are several ways to determine if the system is melted, crystallized or remains unchanged. One is the direct visualization by plotting the two-phase model. The temperature effect on the system can also be obtained from potential energy and radial distribution function (RDF). Figure 4.4 shows the potential energy (PE) dynamics of a two-phase system at 40 GPa simulated at different temperatures. At $T = 4250$ K, PE increases with time, suggesting that the solid is melting thus $T_m < 4250$ K. The opposite is for $T = 4000$ K. At $T = 4125$ K, PE remains almost constant for the 20 ps run, suggesting the T_m is close to 4125 K. Melting and crystallizing can also be identified from the long range order manifested in RDFs. RDF is the spherically averaged distribution of interatomic vector lengths and can be computed from the trajectory file data. Figure 4.5a shows the RDFs of all the Si and O atoms in solid (solid line) and in liquid (dashed line) at the beginning of the two-phase NPT run ($t = 0$ ps) at 40 GPa and 4000 K. The 1st peak is Si-O and 2nd Si-Si. The solid RDF has distinct peaks up to the cutoff distance (9 Å) due to the long-range order of crystalline solid, while the liquid RDF has only the first two peaks and lacks long-range order as expected. When this two-phase model evolves from $t = 0$ ps to $t = 20$ ps, long-range order becomes apparent in the liquid half of the two-phase system,

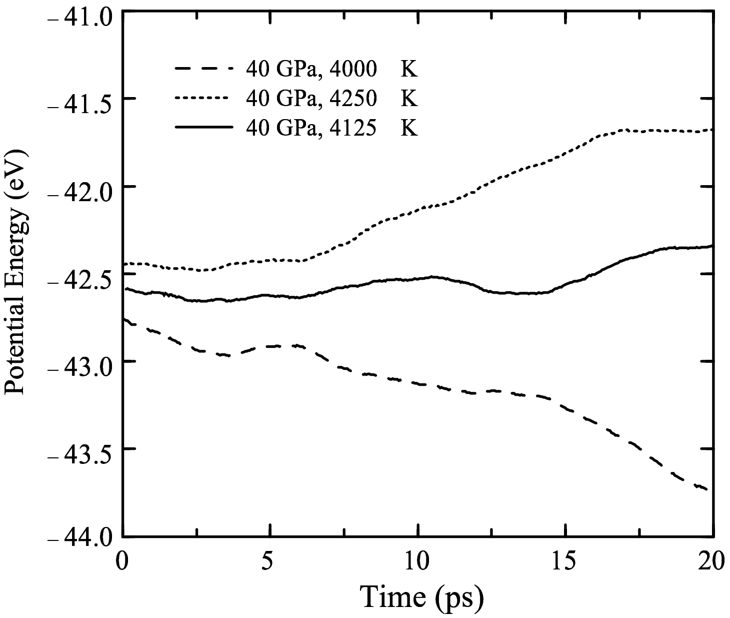

Figure 4.4: The dynamics of the potential energy (PE) of the two-phase system ($P = 40$ GPa) at different temperatures. The energy is for 2 SiO_2 formulae.

suggesting that at 4000 K the liquid crystallizes. Within 20 ps, the liquid reaches a RDF similar to the solid portion (Figure 4.5b). Thus we found that at 40 GPa, the melting temperature $T_m > 4000$ K. The opposite happens for $T = 4500$ K where the solid loses its long range order and melts, *i.e.*, T_m <4500 K (Figure 4.5c-d). Thus T_m is bracketed between 4000 K and 4500 K.

By repeating the above procedure, the melting temperature T_m at certain pressure can be bracketed, in our case, with variations less than 125 K. The melting points for stishovite at five different pressures are shown in Table 4.4. By comparing the melting temperatures T_m from the single- and two-phase simulations, we found that the latter yielded lower T_m by 500-1500 K. At high pressure, the difference is more pronounced. The melting curve flattening from the two-phase simulations is consistent with the Clausius-Clapeyron slope changes from the single-phase simulations.

Figure 4.6 shows our MD results (closed and open circles) along with the results from static and dynamic experiments and former MD simulations on stishovite. The single-phase simulations yielded results close to the DAC results [*Shen and Lazor*,

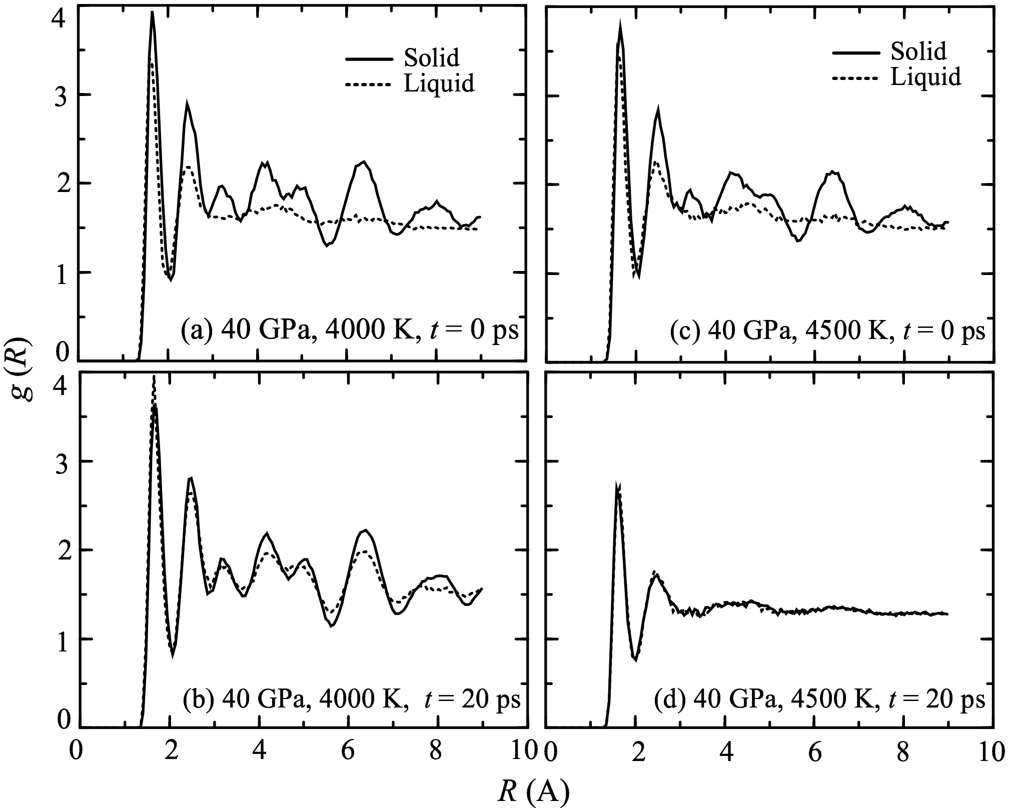

Figure 4.5: Snapshots of the radial distribution functions (RDF) for the atoms originally existing as liquid and solid respectively in the two-phase system at 40 GPa and different temperatures. (a) T = 4000 K, 0 ps; (b) T = 4000 K, 20 ps; (c) T = 4500 K, 0 ps and (d) T = 4500 K, 20 ps.

1995] at 20 and 40 GPa, but significantly higher results above 40 GPa than those from shock wave experiment [*Lyzenga et al.*, 1983] and former MD modeling [*Belonoshko and Dubrovinsky*, 1995]. This indicates that single-phase simulation could lead to more pronounced superheating at high pressures. But at low pressures, single-phase simulation might produce reasonable results. Our two-phase simulation results are in reasonably good agreement with former DAC and shock-melting studies, except at 20 GPa where the large slope of melting curve makes the simulation more sensitive to the interface effect discussed above. Comparing with former MD simulation, our two-phase simulation results are lower and closer to experiments except at 20 GPa.

The melting curve of stishovite is proposed based on our MD simulations and former DAC and shock wave experiment results from 20 to 120 GPa. The phase boundaries for silica at low pressures are established based on former static experiments [*Jackson*, 1976; *Kanzaki*, 1990; *Zhang et al.*, 1993]. Thus, the phase diagram of the silica system has been extended to the mega bar regime with sound experimental and theoretical bases.

4.4 Discussion

The MD simulations of the melting curve of stishovite with MS-Q FF are in general agreement with static and dynamic experiments. One significance is that it appears to validate the interpretation of superheating of solid along the Hugoniots from shock melting experiments (Figure 4.6 insert, the dashed portion above the solid line) on fused quartz and quartz proposed by *Lyzenga et al.* [1983]. Superheating of shocked solid might be also common to iron [*Brown and McQueen*, 1986] and other materials. The first liquid states on the Hugoniot (stars, Figure 4.6) are close to the solidus.

The silica phase diagram and equation of state will help constrain the interpretation of the seismic structure in terms of the chemical composition of the Earth's interior, such as the chemical reactions at the core-mantle boundary which might give rise to the lateral heterogeneity at D" [*Knittle and Jeanloz*, 1991]. In particular, the possibility that the ultra-low velocity zone (ULVZ, [*Garnero and Helmberger*, 1995;

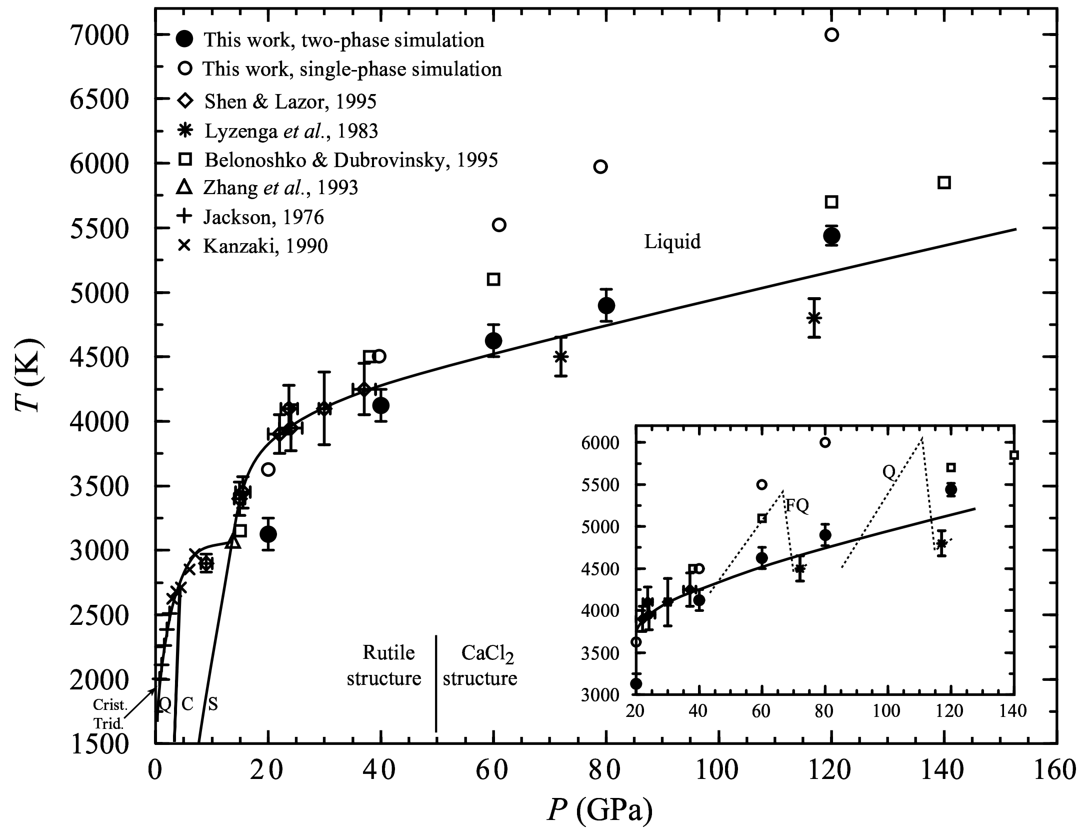

Figure 4.6: The melting curve of stishovite and phase diagram of silica system from this work and previous experimental and theoretical studies [*Belonoshko and Dubrovinsky*, 1995; *Lyzenga et al.*, 1983; *Shen and Lazor*, 1995; *Jackson*, 1976; *Kanzaki*, 1990; *Zhang et al.*, 1993]. Q: quartz; C: coesite; S: stishovite and FQ: fused quartz. (*insert*) Dashed lines are shock temperature measurement of shocked fused quartz and quartz [*Lyzenga et al.*, 1983]. The sharp drop of temperature indicates the melting of stishovite. The portion of Hugoniots above the melting curve (solid line) is the superheated stishovite solid.

Luo et al., 2001]) at the CMB is caused by partial melting [*Garnero and Helmberger*, 1995] demands that we develop a basis for modeling melting relations under such conditions. This will require melting curves and EOS data for solids and liquids in the MgO-SiO_2-FeO-Fe system, at least.

Although most cosmochemical models call for a perovskite plus magnesiowustite lower mantle, physical data permit considerable free silica. Thus, *e.g.*, it has been shown that the mean atomic weight μ is constant and close to 21 throughout the lower mantle [*Watt et al.*, 1975]. For silica, μ is 20. Seismic results show that the thermal expansivity in the lowermost mantle is close to 1×10^{-5}/K (e.g., at 2671 km depth and 2405 K [*Brown and Shankland*, 1981]), close to our simulations at 120 GPa (about 2671 km depth in the Earth, Figure 4.2c). Our results have shown that at lower mantle condition, thermal expansivity of stishovite is a weak function of temperature, which may be true more generally for lower mantle phases and for the bulk lower mantle. The knowledge of thermal expansivity can help to constrain other important parameters such as the Grüneisen parameter and Rayleigh number.

It is significant that a simple force field, the MS-Q FF for silica system, leads to results in accord with previous experimental and theoretical studies considering the fact that this force field describes the whole silica system with complex polymorphic phase changes. But discrepancies exist. This MS-Q force field predicts the $CaCl_2$ transition at ~130 GPa and α-PbO_2 transition at ~102 GPa from energy minimization simulations. While the latter transition pressure is in good agreement with *ab initio* results (compared to 98 GPa [*Karki et al.*, 1997]), our force field overestimates the free energy of the $CaCl_2$ phase leading to a high transition pressure compared with previous results (~50 GPa) from experiments and *ab initio* calculations [*Karki et al.*, 1997; *Kingma et al.*, 1995]. This could be due to the simplicity of the potential which fails to accurately describe the subtle structural and energetic differences between the rutile and $CaCl_2$ structure. Although our potential predicts the transition to the orthorhombic structure at too high a pressure, the high-pressure melting temperature calculations remain relevant since stishovite and the higher pressure phases have similar properties. *ab initio* calculations [*Karki et al.*, 1997, 2001] and experimental results [*Kingma et al.*, 1995] show that the shear modulus is only significantly reduced at the $CaCl_2$ transition pressure (~50 GPa). The comparison between elastic constants for rutile, orthorhombic and columbite (α-PbO_2) as a function of pressure show the same trend across the different phases except in a narrow pressure region around ~50 GPa [*Karki et al.*, 1997].

4.5 Conclusion

We have applied a Morse-stretch charge equilibrium force field for silica system to stishovite and obtained equation of state, thermal expansivity and melting curve of stishovite. The simulations are in general agreement with previous experimental and theoretical studies, and confirm extrapolation using standard EOS formulisms. The thermal expansivity of silica at lowermost mantle conditions is a weak function of temperature. The stishovite melting simulation appears to validate the interpretation of superheating of the solid along Hugoniot. The EOS and phase diagram of silica will help to constrain the interpretation of the seismic observations and geodynamic modeling of the mantle.

Acknowledgement: The computational facility is supplied by MSC, Beckman Institute, Caltech (WAG). The constructive comments by P. Asimow and two anonymous reviewers helped to improve the manuscript. T. Çağın , A. Strachan, W. A. Goddard III , and T. J. Ahrens contributed partly to this work.

Chapter 5

Polymorphism, Superheating and Amorphization of Silica upon Shock Wave Loading and Release

Abstract

We present a detailed and quantitative examination of the thermodynamics and phase change mechanisms (including amorphization) that occur upon shock wave loading and unloading of silica. We apply Debye-Grüneisen theory to calculate both the Hugoniot of quartz and isentropic release paths. Quartz converts to stishovite (or a stishovite-like phase) between 15 and 46 GPa, and persistence of the solid phase above its liquidus (*i.e.*, superheating) is confirmed between 77 and 110 GPa. Calculations compare favorably to measurements of shock and post-shock temperatures. For silica, the method of measuring post-shock temperature is insensitive to predicting whether phase transitions actually occur during release. Measurements of release states in pressure-particle velocity space are compared to computed frozen-phase release paths. This suggests transformation of a stishovite-like phase to lower density phases including quartz, liquid, or dense amorphous glass. Transformations to liquid or glass occur upon release from peak pressure of 26 GPa and above. The isentropic release assumption appears to be approximately valid. A shock pressure-temperature scale relating metamorphism of silica in shock-loaded quartz is proposed. Neither recovery of coesite nor substantial quantities of crystalline stishovite-like phases upon shock loading of quartz is predicted. Trace amounts of crystalline stishovite-like phases from shock loading between 15 and 26 GPa are expected.

5.1 Introduction

Silica is of great interest for geophysics and condensed-matter physics. It is a prototype system for understanding the fundamental physics of phase changes, and an end member of silicates believed to be important constituents of the terrestrial planets [*Hemley et al.*, 1994]. The phase change mechanisms and kinetics upon dynamic loading and subsequent release in laboratory impact and intense laser irradiation experiments are also of particular interest. Shock wave loading and unloading are associated with interesting phenomena such as polymorphism, superheating, amorphization upon compression and decompression, and shear melting. Models of material behavior under dynamic loading/unloading are also required for interpreting the effect of natural planetary impacts, yet the existing quartz shock pressure-temperature ($P-T$) scale [*Stöffler*, 1971] was based on earlier calculations [*Wackerle*, 1962] that did not take the quartz-stishovite transition into account. A complete description of the thermodynamic states of quartz upon shock wave loading and release is not well established, despite considerable efforts [*Grady et al.*, 1974; *Podurets et al.*, 1976; *Chhabildas and Grady*, 1984; *Chhabildas and Miller*, 1985; *Swegle*, 1990; *Langenhorst et al.*, 1992; *Akins and Ahrens*, 2002]. The accuracy of post-shock temperature measurements [*Boslough*, 1988], and the validity of the isentropic assumption for converting measured pressure-particle velocity ($P-u_p$) data into pressure-volume ($P-V$) paths [*Podurets et al.*, 1976] along release adiabats involving phase changes [*Swegle*, 1990], have been controversial.

Silica polymorphs have been extensively investigated with dynamic techniques, and the shock wave equations of state (Hugoniots) of fused quartz, α-quartz, coesite and stishovite are well defined [*Wackerle*, 1962; *Al'tshuler et al.*, 1965; *Trunin et al.*, 1971; *Podurets et al.*, 1981; *Marsh*, 1980; *Luo et al.*, 2002d]. Shock temperature measurements [*Lyzenga et al.*, 1983] on fused quartz and on quartz extended the melting curve of silica beyond the pressure-temperature range of existing diamond-anvil cell experiments (*e.g.*, *Shen and Lazor* [1995]). The phase diagram of silica has been established up to megabar regime based on the joint efforts from static and dynamic experiments, and theoretical simulations such as *ab initio* [*Karki et al.*, 1997] and molecular dynamics techniques [*Luo et al.*, 2002c]. The unloading paths of shocked quartz were carefully measured in $P - u_p$ space but have not been fully utilized [*Podurets et al.*, 1976]. These advances in knowledge of the equation of state and other thermodynamic properties of silica (especially stishovite) now permit a detailed quantitative examination of thermodynamic state and mechanisms of phase changes upon shock wave loading and unloading, as well as post-shock temperature measurement and isentropic release assumption.

We begin by reviewing the methodology of calculating both Hugoniot states and release isentropes in both single-phase and mixed-phase states using Debye-Grüneisen theory. For release, we examine the frozen and non-frozen phase release paths and their relation to the equilibrium phase diagram of silica and measurements of $P - u_p$ upon release. Based on calculated thermodynamic states and phase assemblages upon shock loading and unloading, we discuss superheating, melting, polymorphism and amorphization in silica. We also evaluate the validity of the isentropic assumption for mixed-phase and reacting release paths. Finally we establish a revised shock $P - T$ scale for impact events involving quartz.

5.2 Thermodynamics of quartz upon shock wave loading and release

5.2.1 Formulation for single-phase properties

To determine the complete thermodynamic state upon shock wave loading (Hugoniot) and release paths, we will adopt classical Debye-Grüneisen theory. The detailed derivations can be found in the literature [*Morse*, 1964; *Swegle*, 1990]. For the convenience of the reader and because of some typographical errors in previous work, we will briefly review the physics and list the equations needed. For non-metal materials under the pressure and temperature conditions of interest, we need only consider the lattice contribution to specific heat (C_V) and neglect electronic contribution. The

Grüneisen parameter (γ) is assumed to be an explicit function of volume V only (specific volume $V = 1/\rho$ where ρ is density). From Debye theory,

$$C_V(T, V) = C_{vm}[4D(\frac{\theta}{T}) - \frac{3\theta/T}{e^{\theta/T} - 1}] \tag{5.1}$$

where

$$D(x) = \frac{3}{x^3}\int_0^x \frac{y^3 dy}{e^y - 1} \tag{5.2}$$

is the Debye function. C_{vm} is the Dulong-Petit high temperature limit of C_V, *i.e.*, normally $3R$ per gram-atom for solids where R is the gas constant. θ is Debye's temperature at corresponding V, and is related to T-independent γ as

$$\gamma(T, V) = \gamma(V) = -\frac{dln\theta}{dlnV} \tag{5.3}$$

Thus, given $\gamma(V)$,

$$\theta(V) = \theta(V_0)exp\{-\int_{V_0}^{V} \frac{\gamma(v)}{v} dv\} \tag{5.4}$$

where subscript 0 denotes the reference state, normally standard temperature and pressure (STP). By thermodynamic integration, we can obtain entropy S, P, and internal energy E as

$$S(T, V) = S(T_0, V_0) + C_{vm}\{\frac{4}{3}[D(\frac{\theta}{T}) - D(\frac{\theta_0}{T_0})] - ln(\frac{1 - e^{-\theta/T}}{1 - e^{-\theta_0/T_0}})\} \tag{5.5}$$

$$P(T, V) = P(T_0, V) + \frac{\gamma C_{vm}}{V}[TD(\frac{\theta}{T}) - T_0 D(\frac{\theta_0}{T_0})] \tag{5.6}$$

$$E(T,V) = E(T_0,V_0) - \int_{V_0}^{V} P(T_0,v)dv + C_{vm}[\frac{1}{3}A(\theta,T_0) + TD(\frac{\theta}{T})] \tag{5.7}$$

where

$$A(\theta,T) = T[D(\frac{\theta}{T}) - 3ln(\frac{1-e^{-\theta/T}}{1-e^{-\theta_0/T_0}}) - 4D(\frac{\theta_0}{T_0})] \tag{5.8}$$

The expressions for enthalpy H, Helmholtz free energy F and Gibbs free energy G can be readily obtained from the definitions $H = E+PV$, $F = E-TS$ and $G = F+PV$. Thus, given two of the thermodynamic quantities, for a single-phase the complete thermodynamic state can be determined.

$P(T_0,V)$, $\gamma(V)$ and associated parameters are assumed to be known *a priori*. The cold pressure $P(T_0,V)$ is most available at $T_0 = 300$ K, in the form of finite-strain Birch-Murnaghan or Vinet universal equation of state (EOS) [*Cohen et al.*, 2000]. For third-order Birch-Murnaghan EOS,

$$P(f) = 3K_{T0}f(1+2f)^{\frac{5}{2}}[1+\frac{3}{2}(K_{T0}^{'}-4)f] \tag{5.9}$$

where the Eulerian strain $f = \frac{1}{2}[(V/V_0)^{-2/3}-1]$, K_{T0} and $K_{T0}^{'}$ are the ambient isothermal bulk modulus and its pressure derivative respectively. A common expression for $\gamma(V)$ is

$$\gamma/\gamma_0 = (V/V_0)^q \tag{5.10}$$

although it could be written in a more general form to accommodate cases of extreme compression and expansion [*Swegle*, 1990]. The reference values S_0 and E_0 at STP for various phases of SiO_2 are available in the literature [*Robie et al.*, 1978; *Saxena et al.*, 1993; *Malcolm*, 1998]. E_0 for quartz is arbitrarily chosen as 0, and other phases are referenced to quartz. The Debye temperature at STP, θ_0, can be determined from elastic constants (acoustic θ) [*Anderson*, 1963] or fitting to specific heat C_V (thermal

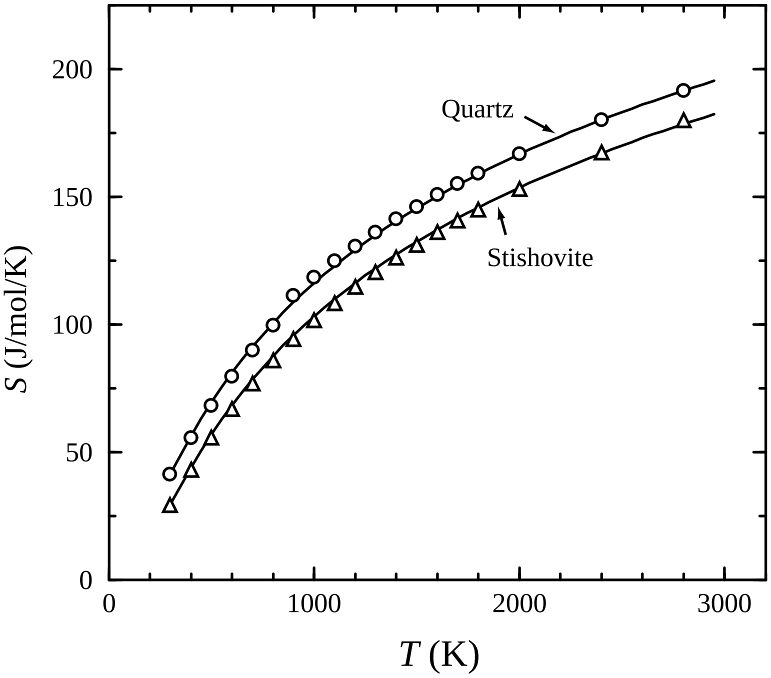

Figure 5.1: Entropy (S) of quartz and stishovite as a function of temperature (T) at ambient pressure. Symbols, *Saxena et al.* [1993]; solid curves, calculations from Debye-Grüneisen theory.

θ). In our calculations, the latter value is adopted. With the fitted values of θ_0 [*Swegle*, 1990], we calculated entropy as a function of temperature at ambient pressure for quartz and stishovite (Figure 5.1). The values from the Debye-Grüneisen theory are in good agreement with tabulated handbook values [*Robie et al.*, 1978; *Saxena et al.*, 1993]. We take this as indication that the Debye-Grüneisen theory, though approximate, is adequate for our purposes. Table 5.1 lists the input parameters needed for the calculation of complete thermodynamic states of quartz and stishovite. We also included static yield strength Y of quartz. The strength effect of quartz at high pressures is still under debate, and we will correct the measured peak stress (σ_H) for strength. Note that this correction is not crucial, as it will not affect the results significantly. Because of the apparently subtle thermo-mechanical and energetic differences between stishovite and post-stishovite phases, we will make no distinction between these two [*Luo et al.*, 2002c] in the shock loading/unloading calculations.

Table 5.1: Thermodynamic parameters for quartz and stishovite. θ_0 is thermal Debye's temperature, and θ_0^{ac} the calculated acoustic Debye's temperature at STP. Y: static yield strength. S_0 and E_0 are from *Saxena et al.* [1993]. Other data for stishovite are from *Luo et al.* [2002d], and for quartz, *Swegle* [1990].

	K_0 (GPa)	$K_0^{'}$	V_0 (cm^3/g)	γ_0	q	C_{vm} (J/K/g)	θ_0 (K)	θ_0^{ac} (K)	S_0 (J/K/g)	E_0 (J/g)	Y (GPa)
α−quartz	37.7	6.4	0.3773	0.70	2.0	1.245	999	571	0.69	0.0	4.4
Stishovite	306.0	5.0	0.2331	1.35	2.6	1.245	1037	1190	0.49	777.2	-

5.2.2 Treatment of two-phase aggregates

If phase change occurs along the Hugoniot or during release, we will assume that only a maximum of two phases are present at any time. We further assume that the assemblage of the parent and new phases maintains a series of states in (possibly metastable) thermal and mechanical equilibrium, *i.e.*, T and P are common to both phases. Then in the case of a mixture of phase 1 and 2, the total internal energy, specific volume, and entropy are given by

$$E = (1 - \lambda)E_1 + \lambda E_2 \tag{5.11}$$

$$V = (1 - \lambda)V_1 + \lambda V_2 \tag{5.12}$$

$$S = (1 - \lambda)S_1 + \lambda S_2 \tag{5.13}$$

where λ is the mass fraction of phase 2. For each phase i=1, 2, $S_i = S_i(P,T)$, $E_i = E_i(P,T)$ and $V_i = V_i(P,T)$ satisfy Equations 5.5, 5.6 and 5.7 with appropriate parameters (Table 5.1). For mixtures of two phases, we now need to specify three independent variables to constrain the complete state of the system. For Hugoniot state calculations we take P, E and V from the Rankine-Hugoniot conservation equations and solve Equations 5.5, 5.11, 5.12 and 5.13 iteratively to obtain T, S, and λ. For frozen-phase release calculations we take fixed P, S, and λ, in which case we can solve to obtain T and V. Finally, for release paths where we have obtained a $P - V$ path as explained below, we can relax the assumption of fixed λ and at fixed P, S, and V we solve to obtain T and λ. Thus the complete thermodynamic state on mixed-phase Hugoniots and certain release paths can be resolved.

5.2.3 Shock wave loading

The Hugoniot of quartz has been previously determined [*Wackerle*, 1962; *Al'tshuler et al.*, 1965; *Trunin et al.*, 1971; *Marsh*, 1980] as shown in Figure 5.2, which is assumed to be hydrostatic, and fitted to analytical form for later calculations. We interpret segment M_1M_2 as a mixed-phase regime (quartz and stishovite). Segments QM_1 and M_2S are regarded as pure quartz and stishovite phases respectively. The exact locations of M_1 and M_2 can be resolved from the value of λ. Using P, V and E on the fitted Hugoniot, we solved simultaneously for shock temperature T and the mass fraction of stishovite λ; total shock state entropy S then follows from Equation 5.13. Table 5.2 lists thermodynamic parameters of shock states at several pressures along the principal Hugoniot of quartz.

The mass fraction of stishovite, λ, starts to increase at 15 GPa and reaches $\sim$1 at 46 GPa (Figure 5.3), thus the mixed phase regime of quartz and stishovite, M_1M_2, is $15 - 46$ GPa. Along the Hugoniot, as the mass fraction of stishovite becomes appreciable around 23 GPa, T_H (H denotes Hugoniot) increases steeply due to the large decrease of the total volume and concomitant increase in the internal energy. At higher pressures above 23 GPa, T_H increases steadily through the mixed-phase and pure stishovite regimes (Figure 5.4). This is consistent with the observation that the shock-front instability develops at about 23 GPa [*Zhugin et al.*, 1999]. The shock temperature was independently measured in the range of $70 - 110$ GPa [*Lyzenga et al.*, 1983]. The calculation agrees closely with experiment except calculated values are higher (about $6 - 8\%$ with experimental errors considered) at pressures of $\sim$ 100 GPa and above. This could be due to high-temperature heat capacities greater than the $3R$ limit assumed by Debye theory, although larger $\theta(V)$ could partly offset this effect at higher pressures. Stishovite remains the sole Hugoniot state phase up to 110 GPa; comparison to the phase diagram of silica (and stishovite melting curve) obtained from experiments and molecular dynamics simulations [*Luo et al.*, 2002c] (Figure 5.4) make it clear that superheating does exist between $77 - 110$ GPa along the Hugoniot of quartz. Beyond about 110 GPa, stishovite melts as demonstrated by

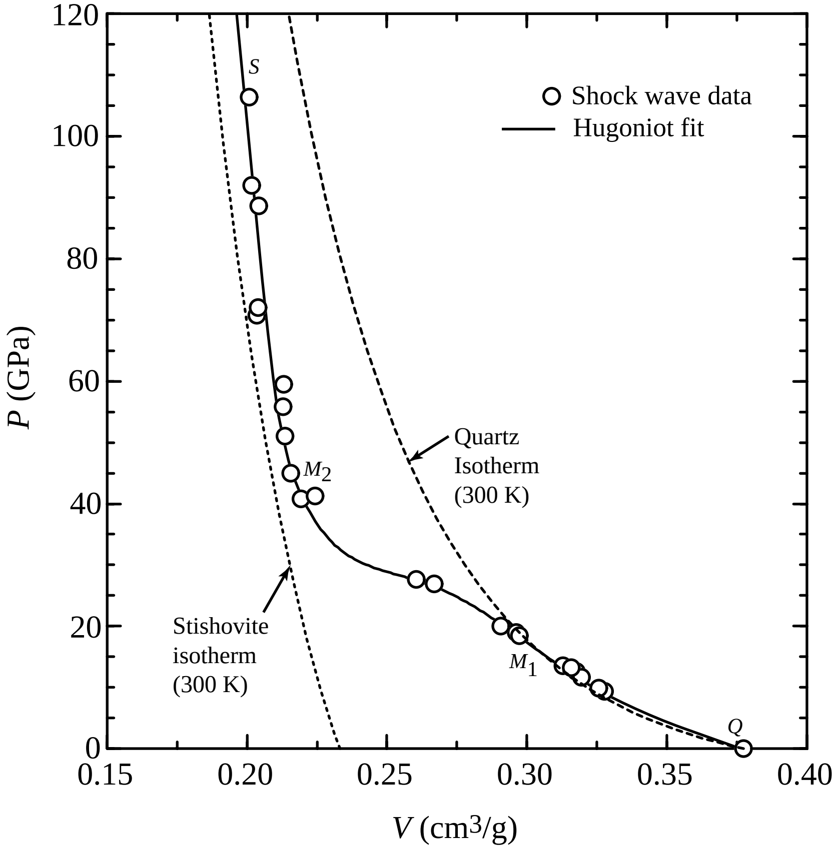

Figure 5.2: Principal Hugoniot of quartz. Data are from *Wackerle* [1962], *Trunin et al.* [1971] and *Marsh* [1980]. Segments QM_1, M_1M_2 and M_2S are regimes of pure quartz, mixed-phase of quartz and stishovite, and pure stishvoite respectively. The 300 K isotherms of quartz and stishvoite are from *Swegle* [1990] and *Luo et al.* [2002d].

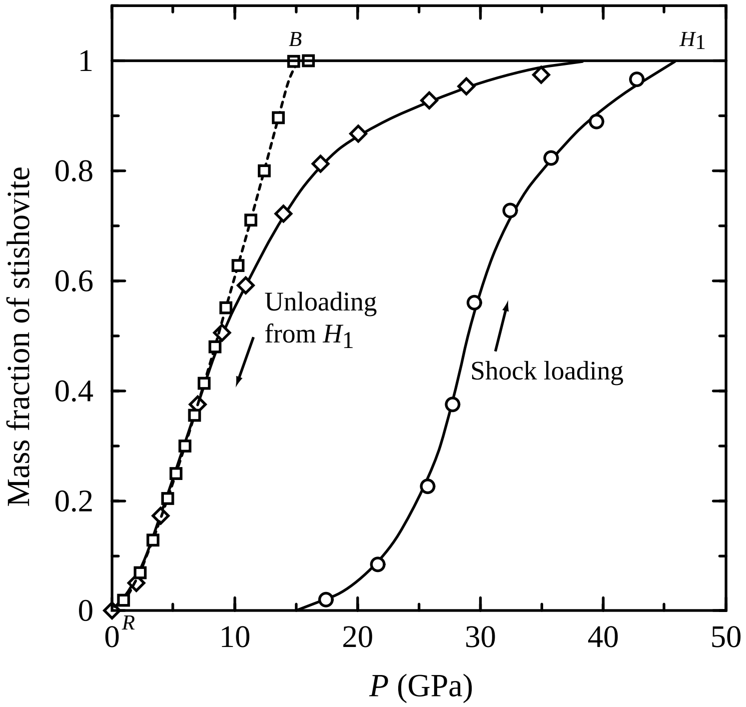

Figure 5.3: Quartz-stishovite transformation: mass fraction of stishovite λ *vs.* P upon loading, and release from H_1 (peak stress of 48.5 GPa). Symbols are points of calculation. From the mass fractions on loading path (circles), the mixed-phase regime on Hugoniot is $15 - 46$ GPa. Release paths H_1R (diamonds) and H_1BR (squares) follow the corresponding $P - V$ paths in Figure 5.6a respectively (also see text).

shock temperature [*Lyzenga et al.*, 1983] and sound speed measurements [*Chhabildas and Miller*, 1985].

5.2.4 Release

The high-pressure phases produced upon shock wave loading, stishovite or post-stishovite phases, could in principle transform into low pressure/density phases such as quartz and coesite, or become melted or amorphized during release from the peak-state pressure and temperature, depending on the kinetics involved. We make a distinction between the state when the sample is recovered and examined (recovery state, ambient pressure and temperature) and the post-shock state (ambient pressure and high temperature, denoted as R), because significant phase changes could have

Table 5.2: Shock and post-shock temperature of shocked quartz: measurement and calculation. Subscript H denotes Hugoniot, and R post-shock (ambient pressure). *a*: *Lyzenga et al.* [1983]; *b*: *Boslough* [1988]; and *c*: calculation with Debye-Grüneisen theory at given volume. $T_{R,s}$ is obtained assuming frozen-phase release. σ_H, the experimental uniaxial stress is corrected to hydrostatic stress (pressure) P_H with $P_H = \sigma_H - \frac{2}{3}Y$.

σ_H (GPa)	P_H (GPa)	P_H^c (GPa)	V_H (cm^3/g)	T_H^a (K)	T_H^c (K)	T_R^b (K)	$T_{R,s}^c$ (K)	S_H (J/K/g)
75.9	73.0	73.6	0.2065	4440±40	4425	-	3279	3.365
85.9	83.0	83.3	0.2042	4850±130	5090	3660	3589	3.527
92.5	89.6	90.3	0.2025	5430±120	5535	3920	3756	3.621
99.3	96.4	97.3	0.2009	5630±140	6000	4000	3906	3.712
107.8	104.9	106.0	0.1990	5900±200	6585	-	4048	3.817
109.7	106.8	107.6	0.1987	6100±190	6715	-	4074	3.839

occurred during cooling over a time period much longer than the shock loading or unloading duration. Thus, the recovered phases are not necessarily the same as those on the release paths.

The post-shock state can be readily calculated if we assume that no phase changes (frozen-phase) occur upon release and that the release is isentropic. It is not impossible that such a frozen path actually occurs, provided appropriate kinetics. At the peak Hugoniot state, the entropy S and phase proportions λ are obtained from the mixed-phase equations in the previous section (*e.g.*, Table 5.2 and Figure 5.3) and these values of S and λ are held fixed along the release path to define a frozen-phase isentropic path. Thus at any pressure P along the frozen release path we solve for T and V as described above. The whole frozen release $P-V-T$ paths from certain peak pressures, including post-shock temperature (T_R), were calculated. Based on the shock temperature recordings of *Lyzenga et al.* [1983], *Boslough* [1988] obtained temperatures released from several shock states which were interpreted as post-shock temperatures. Our calculations closely agree with Boslough's results (Table 5.1 and Figures 5.4).

Whether phase changes occur upon release can possibly be resolved from well-measured release paths. One common method to determine release states is to mea-

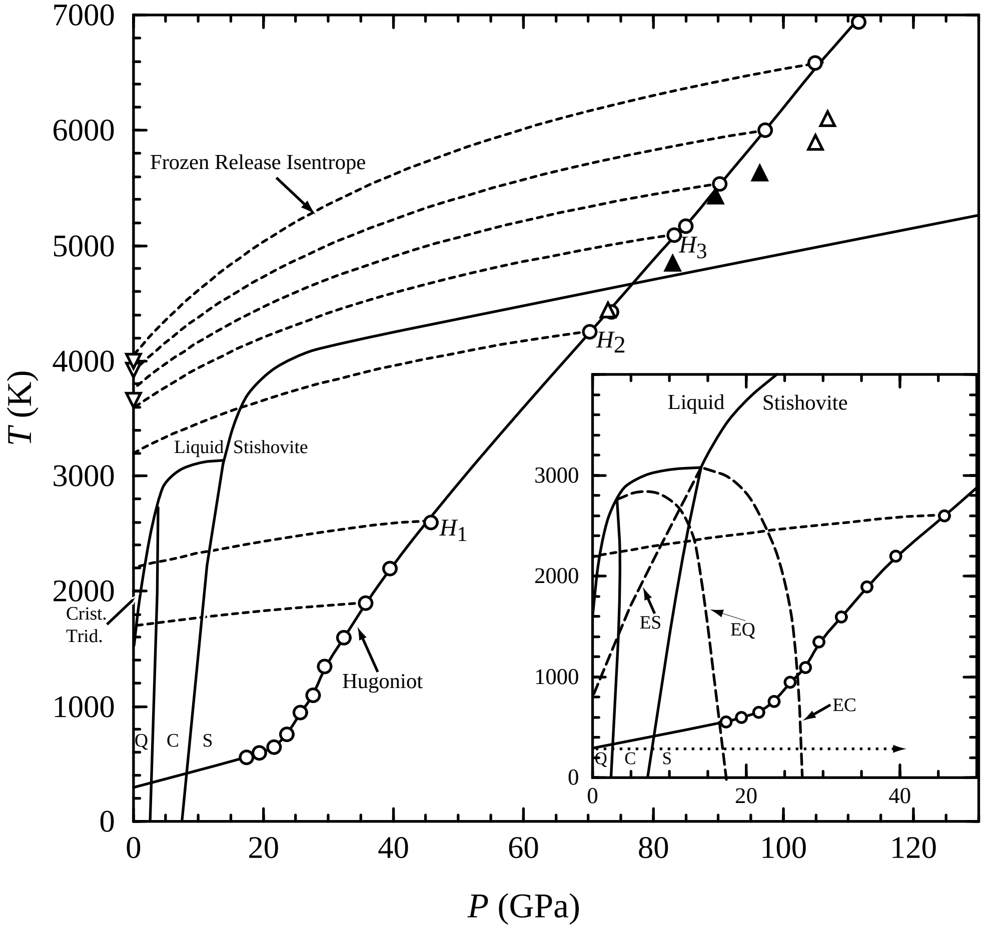

Figure 5.4: Phase diagram of silica [*Luo et al.*, 2002c], calculated quartz-Hugoniot temperature (circles), measured shock temperature (filled and open triangles) [*Lyzenga et al.*, 1983] and post-shock temperature (inverted triangles, corresponding to shock temperatures denoted as filled triangles respectively) [*Boslough*, 1988]. Dashed curves are frozen-phase release isentropes. Q: quartz, C: coesite and S: stishovite. H_1, H_2 and H_3 denote three typical states on Hugoniot. (*insert*) Same as the full figure except that: Long dashed curves are fictitious extension (metastable) of melting curve of quartz (EQ), coesite (EC) and stishovite (ES). Dotted line denotes the room temperature static compression path, where quartz and coesite become amorphous at $25-35$ GPa [*Hemley et al.*, 1988].

sure the particle velocity of the shock states achieved when the shock passes from the sample into a series of buffer materials of lower impedance than the sample (*e.g.*, polycarbonate, polystyrene, compressed Ar) as well as the free surface velocity of the sample material. By shock loading the sample to the same peak pressure and then unloading adiabatically against a series of such lower impedance buffer materials, a sequence of release states in the $P - u_p$ plane is obtained. Figure 5.5 shows three release paths unloaded from shock states H_1, H_2 and H_3 [*Podurets et al.*, 1976]. In order to transform from the $P - u_p$ to the $P - V$ plane, we assume that the release path is an isentrope. If phase changes occur on release (non-frozen release), this isentropic assumption is under debate [*Podurets et al.*, 1976]. Although independent verification of the isentropic assumption is not available, the assumption itself does not violate any thermodynamic laws. We will assume release to be isentropic in the following discussion.

For isentropic flow, the Riemann invariant [*Zel'dovich and Raizer*, 2002] is

$$J_{\pm} = u_p \pm \int \frac{dP}{\rho C} \tag{5.14}$$

where C is speed of sound ($C^2 \equiv \frac{dP}{d\rho} |_S$). Thus the volume increase ΔV along release isentrope

$$\Delta V = - \int_{V_1}^{V_2} \frac{du_p}{dP} |_S \, du_p \tag{5.15}$$

can be obtained from the release path in the $P - u_p$ plane. In some cases, only u_p at the free surface and peak shock state are known (point H and R in Figure 5.5 insert) possibly with a few intermediate states (*e.g.*, B). It can be shown by a variational method [*Lyzenga and Ahrens*, 1978] that the final volume calculated from Equation 5.15 using a piece-wise linear fit to a discrete series of $P - u_p$ points is a minimum estimate of the true release volume. $P - u_p$ measurements via other techniques such as reverberation and release-wave profile [*Chhabildas and Miller*, 1985] agree with the $P - u_p$ results from the buffer method [*Podurets et al.*, 1976].

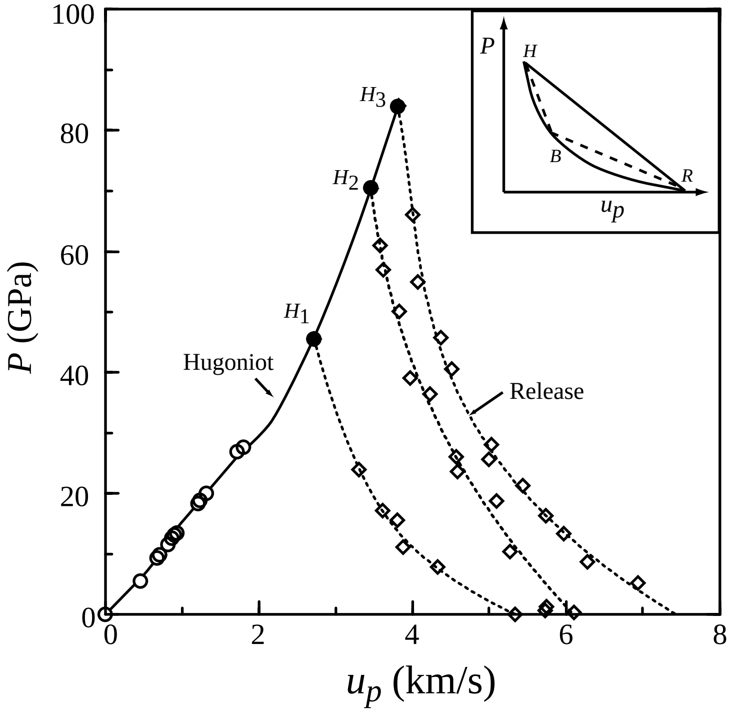

Figure 5.5: Measured $P-u_p$ upon shock loading and release: open circles, *Wackerle* [1962]; filled circles and diamonds, *Podurets et al.* [1976]. (*insert*) Schematic release paths in $P-u_p$. H, B and R denote shock state, intermediate and final release states respectively.

The measured $P-u_p$ paths [*Podurets et al.*, 1976] were fitted to analytical form (Figure 5.5), and mapped to $P-V$ space as shown in Figure 5.6.

We may now compare the release paths inferred from conversion of $P-u_p$ data with the isentropic frozen-phase releases. In $P-V$ space (Figure 5.6), the release paths converted from measured $P-u_p$ can be divided into an initial high-pressure segment that remains close to the frozen-phase calculation followed by a low-pressure segment beginning near $\sim$ 30 GPa that deviates considerably towards higher volume. This indicates that stishovite transforms to lower density phases. The post-shock density ρ_R released from low (H_1) and high (H_3) pressure are 2.29 and 2.14 g/cm^3 respectively (both close to glass density at STP 2.20 g/cm^3). In the case of intermediate pressure H_2, ρ_R is considerably denser (3.01 g/cm^3, Table 5.3). This result could be due to differences in the identities and proportions of the phases that form upon release from these three states, or perhaps to differing degrees of relaxation if a glassy phase is

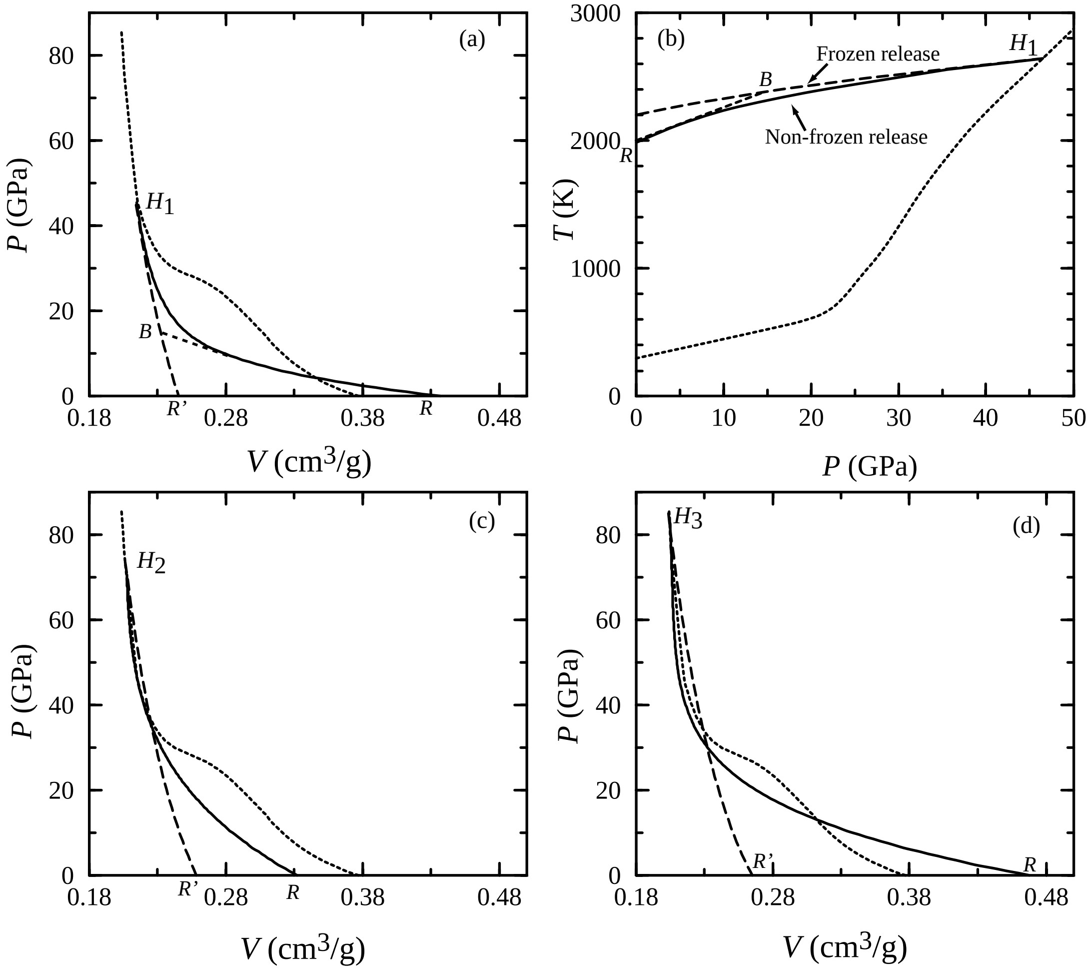

Figure 5.6: Principal Hugoniot of quartz (dotted curves), calculated frozen-release paths (long dashed curves), release paths converted from $P - u_p$ measurement [*Podurets et al.*, 1976] (solid curves) from shock states H_1 (a), H_2 (c) and H_3 (d), shown in $P - V$. For frozen release, the post-shock volume $V_{R'}$, $H_1 < H_2 < H_3$. For converted release path from $P - u_p$, $H_2 < H_1 < H_3$. In (a), B denotes a speculated stishovite-quartz transition point, and H_1BR is an approximation to solid curve H_1R. The corresponding $P - T$ paths for H_1 are shown in (b) with Hugoniot (dotted curve).

Table 5.3: Post-shock ($P = 0$) temperature for isentropic releases from typical peak shock states. s and m denote frozen and non-frozen release respectively. For non-frozen case, phase changes of stishovite (S) to quartz (Q) and liquid (L) are considered. V_R is obtained from $P - u_p$ measurement (Figure 5.6), and λ is the mass fraction of stishovite and estimated with handbook values at ambient pressure.

Shock State	S_H (J/K/g)	$T_{R,s}$ (K)	Phase Trans.	V_R (cm^3/g)	λ	$T_{R,m}$ (K)
H_1	2.768	2200	S→Q	0.4372	0	1990
H_1	2.768	2200	S→L	0.4372	0	1850
H_2	3.324	3200	S→L	0.3320	0.53	3110
H_3	3.543	3617	S→L	0.4676	0	3273

involved. The production of lower density, higher entropy phases such as quartz and glass (or melt) during release does not necessarily mean that the final temperature is significantly lower than that from frozen phase release, because the entropy of fusion of silica is small and the smaller γ_0 of low density phases would partly offset the temperature decrease induced by endothermic phase transition and volume expansion. Indeed the differences between T_R estimated for frozen-phase releases and releases with phase transitions are in the range $100 - 350$ K (Table 5.3), or comparable to the error in post-shock temperature measurements.

Amorphous phases are readily recovered from shocked quartz (*e.g.*, *Wackerle* [1962]), but this does not necessarily imply significant amorphous material at the post-shock state R, since amorphization or melting might occur afterwards. However, the appreciable decrease in density shown in $P - V$ paths converted from measured $P - u_p$ paths clearly demonstrates such phase changes do occur along release paths (Figure 5.6, Table 5.3). The thermodynamic paths upon frozen-phase release are different for H_1, H_2 and H_3, *i.e.*, different phase changes are supposed to be triggered at distinct equilibrium phase boundaries (Figure 5.4). Along frozen release path H_1, stishovite remains stable until it crosses the coesite-stishovite boundary at 12 GPa and other phase boundaries below 5 GPa, thus we might expect to see the transition of stishovite to coesite, β-quartz and liquid in sequence. For H_2, stishovite remains stable until the liquid-solid phase boundary is crossed at 16 GPa, where stishovite may melt. The release from H_3 is different in that the shock state (as well as the whole frozen release path) is superheated; thus melting could occur at any point on the release path. The $P-V$ paths converted from $P-u_p$ [*Podurets et al.*, 1976] assuming isentropic release (H_iR, i=1, 2 and 3, Figure 5.6a, c and d) in fact differ significantly both from the frozen-phase release calculations (H_iR' in Figure 5.6) and from these predicted thermodynamic equilibrium paths. The deviations are significant even when we take into account the errors in estimation of the release paths (about 6%, according to *Chhabildas and Grady* [1984]). On release from H_1, for example, (Figure 5.6a) the phase should remain stishovite until 12 GPa yet H_1R begins to deviate from H_1R' at about 30 GPa and is significantly different by 20 GPa. Likewise, release from H_2 deviates from the frozen phase path before encountering any phase boundaries (Figure 5.6c). The most plausible explanation for this curious behavior, if the $P-V$ paths converted from $P-u_p$ are accurate, is that non-hydrostatic stresses may displace the equilibrium boundaries to higher pressure (*e.g.*, *Simha and Truskinovsky* [1994]). Release from H_3, on the other hand, deviates in the sense that a phase transition is delayed relative to crossing the equilibrium boundary (Figure 5.6d), which can be explained by the kinetics of superheating of crystalline phases in liquid stability fields [*Luo et al.*, 2002b]. There is also the possibility of artifacts resulting from fitting smooth curves through series of discrete $P-u_p$ points that are not densely sampled enough to capture sharp changes in slope at phase boundaries, though such breaks are not obvious in the $P-u_p$ data (Figure 5.5).

Since the data suggest that phase transitions do occur during release, we formulate a method for computing isentropic release with phase changes. We assume that the total entropy of the system is conserved and that the phases share a common temperature at each pressure. The alternative model of allowing each phase to release along its own isentropic $P-T$ is negligibly different as shown later. Given S held constant from the peak state and V on the $P-V$ release path, the mass fraction λ and T on the release path can be solved as described above. This calculation differs from the frozen-phase release calculations, where we used the same equations but held λ constant and solved for V; here, by contrast, we take V as given and compute

λ.

For release from H_1, stishovite might invert to quartz, amorphize or melt. Let us first assume that only the stishovite-quartz transition occurs. We take the $P-V$ path H_1R literally and calculate the release $P-T$ path and mass fraction of stishovite (λ), as shown in Figure 5.6b and Figure 5.3. Another possibility is that the phase change runs rapidly once it nucleates and that the $P-u_p$ data give an overly smoothed view of the transition, so we also calculate a two-step $P-V$ path that approximates H_1R (solid line) with H_1BR (Figure 5.6a) and redo the calculation for T and λ (Figure 5.6b and Figure 5.3). There are only minor differences in temperature paths for these two cases; the estimated post-shock temperature for release to quartz is 1990 K using the Debye-Grüneisen model. At ambient pressure, tabulated data on heat capacity and entropy are available as well, and in this case the same temperature, 1990 K for quartz at 1 bar with the specific entropy of the H_1 Hugoniot state. The difference between this value for T_R and the post-shock temperature for the frozen-phase stishovite release from H_1, 2200 K, is comparable to the uncertainty in temperature measurement. In other words, the $P-u_p$ data clearly constrain the presence of phase changes on release but the post-shock temperature data do not.

Release from H_2 and H_3 clearly involve crossing of the melting curve rather than formation of quartz. We need to consider whether this is best described as a melting process or an amorphization. In either case, stishovite loses its long-range order. Whether we describe states as liquid or amorphous depends on whether the disordered structure can continue to relax and maintain equilibrium configurations during release. This issue is conventionally addressed for relaxation of shear stresses by assuming a Maxwell-like viscoelastic rheology characterized by a shear modulus G and a temperature-dependent shear viscosity $\eta(T)$, in which case the characteristic relaxation time τ is given by $\tau = \eta(T)/G$. For silicate liquids, G is on the order of 10^{10} Pa. This viscosity describes shear relaxation but it is thought to approximate volume relaxation behavior as well. Thus if we know the viscosity of the amorphous phase as a function of temperature, then for any given timescale of interest we can find a critical temperature T_g above which the system maintains relaxed states throughout the process and is deemed a liquid; otherwise, its density will be history-dependent and it is glass-like or simply amorphous. In this latter, unrelaxed case, there is the possibility of recovering a dense amorphous silica phase. At ambient pressure, the $\eta - T$ relationship of pure SiO_2, a strong liquid, can be described by an Arrhenius relationship [*Richet and Bottinga*, 1995],

$$log\eta = -7 + A(\frac{10^4}{T}) \tag{5.16}$$

where constant $A \sim 2.67$, and η is in Pa·s. For the buffer method, the measured $P - u_p$ is an instantaneous value, and the release time-scale involved is $10^{-9} - 10^{-8}$ seconds. This is also the time-scale over which release measurements probe the state of disordered stishovite. This indicates a critical temperature $T_g \sim 3100$ K. If the release time is larger, T_g will be even lower. In the case of H_2 and H_3, T_R of frozen release is higher than T_g, thus we describe the phase transition experienced by stishovite during release as melting and expect that the phase at the post-shock state will be low-density silica liquid. However we cannot rule out unrelaxed decompression of a dense amorphous state during release because the above development makes several assumptions including a weak pressure-dependence of $\eta - T$ relationship, a constant shear modulus, and a similarity between volume and shear relaxation.

Because the equation of state and thermodynamics of liquid silica at high P and T are poorly constrained, a meaningful and rigorous calculation of the complete release paths involving mixtures of stishovite/liquid or stishovite/glass will be left open. Entropy, heat capacity C_p and thermal expansivities for stishovite and silica liquid at ambient pressure, however, are documented [*Malcolm*, 1998; *Saxena et al.*, 1993; *Navrotsky*, 1994], and the above argument about relaxation time suggests that the liquid phase at the post-shock states released from H_2 and H_3 will be relaxed to low-pressure properties. Considering only the post-shock states at ambient pressure, then, knowledge of the entropy (presumed equal to shock state entropy) and the release volume V_R allow an estimate of the phase proportions and post-shock temperature after release from H_2R and H_3R (Table 5.3). In H_2 case, the mass fraction of stishovite is

0.53, and temperatures for frozen and non-frozen release differ by only 90 K. In H_3 case, stishovite transforms into liquid totally, and the post-shock temperature estimates are 3617 K and 3273 K for frozen and non-frozen release respectively. Finally, if we now consider the possibility that the volume increase seen on release from H_1 is an amorphization rather than an inversion to quartz, the estimate of T_R from low-pressure properties of ordinary silica liquid suggests $T_R = 1840$ K (compared to 1990 K for inversion to quartz and 2200 K for frozen-phase stishovite). This is below the estimate of T_g for relaxed behavior and so the liquid properties may not be appropriate. Nevertheless, it seems clear that in all cases, T_R estimates allowing for phase transitions during unloading are only $100-350$ K lower than those for frozen release. Hence without direct measurement of the phases present at release state we can still conclude that the post-shock temperatures inferred by [*Boslough*, 1988] are approximately correct. Thus it appears to validate the methodology of measuring post-shock temperature [*Boslough*, 1988]. This also suggests that melting in SiO_2 upon release is best resolved from volume instead of temperature, because the entropy of fusion is too small to give a clear signal of T_R.

5.3 Discussion

5.3.1 Superheating

In general, in studies of the kinetics of melting and freezing, it is straightforward to achieve undercooled liquid states but extremely challenging to obtain solids superheated above their congruent melting temperatures, mostly because of heterogeneous nucleation on grain boundaries and other sites. In shock loaded samples, however, temperatures can be increased by $\sim 10^3$ K on a *ns* time-scale, corresponding to a heating rate of 10^{12} K/s. The sample is heated internally as the shock front passes, and hence superheating is limited by homogeneous nucleation. Shock temperature measurements on fused quartz and quartz [*Lyzenga et al.*, 1983] and sound speed measurements [*Chhabildas and Miller*, 1985] clearly demonstrate the persistence of stishovite above its melting curve and hence superheating upon shock loading. On the principal Hugoniot centered on quartz, the maximum superheating $(T - T_m)/T_m$ (where T_m is equilibrium melting temperature) is about 0.22 at ~110 GPa. If we examine the frozen release path with respect to the equilibrium phase boundary, the whole release path for H_3 is superheated. In the case of H_2, stishovite remains stable until the release path crosses the liquid-stishovite phase boundary at about 16 GPa, where stishovite becomes superheated. As shown in Figure 5.6c-d, volume increases sharply below $\sim$ 20 GPa along both release paths H_2R and H_3R. This could be associated with the sharp drop of T_m of stishovite beginning at 20 GPa (Figure 5.4), which gives rise to a rapid increase in the superheating ratio along these release paths below 20 GPa. In the case of H_3, superheating is about 0.1 at the shock state and increases to about 0.3 at 15 GPa, which appears to be similar to the homogeneous nucleation-limited maximum superheating in silica [*Luo et al.*, 2002b]. Based on the large volume attained by H_3 upon release there appears to be sufficient time after nucleation occurs for the stishovite to melt completely. The case of H_2 is different in that the release state appears to be only partially molten despite being in the stability field of liquid. The explanation may lie in the very short time interval after the pressure (~2 GPa) at which the H_2 path achieves large superheating relative to its liquidus.

5.3.2 Polymorphism

Polymorphism upon shock loading and unloading mainly involves quartz-stishovite transition and related mechanisms. During loading quartz transforms directly into stishovite (surpassing coesite) and the mixed-phase (quartz and stishovite) regime on the Hugoniot $(15 - 46$ GPa$)$ lies at higher pressure than the equilibrium boundary. The rarity of recovered coesite in laboratory experiments on shocked quartz suggests that the forward and backward transitions between quartz and coesite are kinetically too sluggish to proceed during short shock durations [*Wackerle*, 1962]. The same may be true of the inverse transition of stishovite to coesite. But the delayed onset of transition to stishovite upon loading implies that a special mechanism is needed to explain the common occurence of this transition during shock loading. For quartz-stishovite transition, *Tan and Ahrens* [1990] proposed a combination of shear-band melting of quartz and recrystallization (progressive bond-bending model) as the quartz-stishovite transformation mechanism. The shear melting model follows *Grady* [1980] who suggested that heterogeneous strain concentrates deformation into narrow shear zones that can attain much higher temperature than that of the bulk sample. Stishovite is then thought to nucleate and grow from melt within the heated zones. Yet, since the heating mechanism depends on concentrating the deformation into a small fraction of the sample volume, it is unclear that a large mass fraction of the sample can be converted by such a mechanism until the bulk shock temperature begins to approach the melting curve. Hence this mechanism may explain minor conversion to stishovite but has difficulty explaining bulk transformation into stishovite near the high end of the mixed phase regime. The occurrence of lamellar features upon recovery can be explained by shear melting.

An alternative (probably dominant) mechanism, a displacive martensitic transition from quartz to stishovite induced by uniform shear stress in the shocked sample, was suggested by *Podurets et al.* [1976]. But the exact displacive quartz-stishovite transformation mechanism remains controversial, and the stress field in shock sample could be complicated. We speculate that the presence of non-hydrostatic stress could shift the phase boundary [*Simha and Truskinovsky*, 1994] toward higher pressures relative to the hydrostatic equilibrium. This mechanism can explain the occurrence of the quartz-stishovite transition when quartz-coesite is not observed, its occurrence at higher pressure than expected, and its ability to achieve bulk transformation to stishovite well below the melting curve. We also note that this may explain the curious observation that upon release from H_1 and H_2, the reverse transformation seems to occur before the phase boundary is crossed, which the model of kinetic delay of a phase transition (until a certain driving force is developed due to overpressure or underpressure) cannot explain. That is, since displacive transitions are in general reversible, the back transition may be taking place under non-hydrostatic but equilibrium conditions. Hence we prefer the model of displacive martensitic transition of quartz to stishovite, perhaps with a minor role for shear melting.

5.3.3 Amorphization

There have been numerous observations of formation of amorphous phases upon compression and decompression at low temperature, sometimes termed cold melting. A similar mechanism has been proposed for the increase in density by formation of a dense amorphous phase through the mixed phase regime ($15 - 46$ GPa) along the principal Hugoniot of quartz studies (see *Sharma and Sikka* [1996] for a review) which we are here attributing to formation of crystalline stishovite.

Proposals for the mechanism of cold melting [*Hemley et al.*, 1988; *Richet and Gillet*, 1997] involve the relative transformation kinetics of solid-solid phase changes and solid-amorphous changes. That is, although crystal I persists metastably in the stability field of crystal II, upon crossing of the metastable extension of the melting curve of crystal I the amorphization process may be kinetically easier than the solid-solid transition. Ice and silica are two classical examples of pressure induced amorphization. Hexagonal H_2O ice (I_h) transforms into high density amorphous ice (hda) at about 1 GPa and 77 K [*Mishima et al.*, 1984]. *Hemley et al.* [1988] demonstrated that at room temperature, crystalline silica (quartz or coesite) becomes amorphous between $25 - 35$ GPa. The insert to Figure 5.4 illustrates the process and its relationship to metastable melting curves with silica as an example. With static compression at room temperature (the dotted arrow), quartz and coesite are expected to transform to stishovite beginning at below 10 GPa. Instead, the low pressure solid persists to $25 - 35$ GPa and then amorphizes. This is the pressure range where the fictitious melting temperatures on the metastable extensions of the melting curves of quartz (EQ) and coesite (EC) may cross below 300 K. Thus, quartz and coesite transform to dense amorphous silica instead of stishovite. The underlying assumption is that amorphization of quartz and coesite are kinetically favored relative to transition to stishovite, at the time-scale of static experiments. During shock compression, however, there are several factors that may kinetically favor solid-solid transition. First, the present calculation shows that at $25-35$ GPa, the temperature is in the range of $850-1900$ K, where transition kinetics should be much faster than at 300 K. Second, the non-hydrostatic stress conditions may allow a displacive martensitic transition mechanism at the shock front. In part the notion that shock compression forms a dense amorphous phase is based on recovery experiments, but recovered amorphous material may well have formed during or after release. The excellent match between the Hugoniot equation of state of silica and static high pressure data on stishovite argue instead for crystalline stishovite on the Hugoniot [*Luo et al.*, 2002d], and this is kinetically plausible.

Based on logic similar to that invoked for cold pressure-induced amorphization, *Richet* [1988] proposed the possibility of amorphization upon decompression across metastable extensions of the melting curves of high pressure phases. As shown in the insert to Figure 5.4, we drew a fictitious metastable extension of stishovite melting (ES) into the low pressure regime which intersects the T-axis at about 900 K. Thus, if the post-shock temperature is higher than 900 K, stishovite could transform to a dense amorphous phase (diaplectic glass) upon release [*Skinner and Fahey*, 1963]. Similar behavior is observed on decompression of other silicates such as $CaSiO_3$ perovskite [*Liu and Ringwood*, 1975]. This may be part of the reason that stishovite is rarely recovered. Even though we argue that stishovite does form at the shock state, in order to be recovered it would have to survive amorphization, inversion to quartz, and ordinary thermal melting during release and cooling.

5.3.4 Isentropic assumption upon release

In the above discussion of release from shock states, we assumed isentropic paths. This assumption produced sensible results, *e.g.*, the calculated post-shock temperature agrees with measurement and, as we will see below, is consistent with recovery results. But we do not have independent verification. Thus, it is necessary to examine the maximum entropy production possible as shown in the following cases.

First we compare the frozen-phase release of a two-phase aggregate in which the phases maintain thermal equilibrium to the case where each phase follows its own isentrope and then they return to thermal equilibrium at 1 bar. We will take release from $P_H = 35.8$ GPa ($S_H = 2.393$ J/K/g, $T_H = 1900$ K, mass fraction of stishovite $\lambda_H = 0.82$) as a typical example. If as above we assume that quartz and stishovite maintain thermal equilibrium upon release, then $T_R = 1710$ K is common to both phases. Now we let quartz and stishovite release separately and isentropically from the shock state with specific entropy of each phase and mass fractions fixed, and the post shock temperatures are different (1466 K and 1772 K for quartz and stishovite respectively). If the system returns to thermal equilibrium at $P = 0$, the maximum entropy production for this adiabatic isobaric process will be the isenthalpic case. The total enthalpy of the system can be readily calculated at post-shock state. If we assume that mass fractions of the phases at final state continue to remain constant, we obtain $T_h = 1720$ K (compared to $T_R = 1710$ K) and the entropy production is negligible.

If in the above case we let the phase proportions change as well during the isenthalpic step at ambient pressure, the maximum entropy is produced when the mass fraction of quartz goes to 1, which corresponds to $T_h = 2240$ K and a significant entropy increase of 22% relative to S_H. This is an extreme case since we delayed the phase transition all the way to ambient pressure, but it implies that phase transitions that occur during release but with finite driving force could significantly increase the entropy. We presently lack a formalism for rigorously evaluating such cases because the Riemann invariant formulation, Equation 5.15 above, assumes isentropic flow and is no longer applicable. Despite this uncertainty, however, our calculations based on isentropic assumption appear to yield reasonable results. Thus, we regard release involving phase changes as a quasi-isentropic process, and isentropic assumption is at least acceptable to first order.

5.4 A pressure-temperature scale

The principal Hugoniot of quartz can be divided into distinct regimes of pressure based on the phases present at peak shock state: $0-15$ GPa, quartz; $15-46$ GPa, mixture of quartz and stishovite; $46-77$ GPa, stishovite; $77-110$ GPa, superheated metastable stishovite; >110 GPa, melt. Here we use our calculations of temperature and phases at post-shock states calculated by frozen-phase isentropic release to predict recovery products that will survive after cooling to ambient temperature, assuming cooling slow enough to avoid quenching of the post-shock phases, as shown in Figure 5.7. At ambient pressure, stishovite become amorphous as low as $800-950$ K [*Skinner and Fahey*, 1963; *Brazhkin et al.*, 1991], the release temperature corresponding to peak shock pressure of ~26 GPa. Quartz melts metastably at 1700 K (expected upon release from peak shock pressure of 35 GPa). Thus, given the mass fractions of quartz and stishovite at peak-shock state, the post-shock temperature from frozen release and phase stability, we divide peak-shock pressure into four regimes (Figure 5.7), distinct from the five shock-state regimes: (I) $P_H = 0-15$ GPa, $T_R = 300-450$ K and Recovery = quartz. Along Hugoniot, no quartz transforms into either coesite or stishovite, due to sluggish quartz-coesite transformation rate and low temperatures. Thus, only quartz will be recovered. (II) $P_H = 15-26$ GPa, $T_R = 450-900$ K, and Recovery = quartz+trace stishovite. Stishovite with mass fraction of up to 0.25 is produced on Hugoniot, and T_R is lower than 900 K. Stishovite will not amorphize, but the back-transformation to quartz is fast. Thus, only trace stishovite will be recovered. (III) $P_H = 26-36$ GPa, $T_R = 900-1700$ K, and Recovery = quartz+dense amorphous glass. In this case, significant stishovite ($\lambda = 0.25-0.8$) is produced at shock state. Even if stishovite did not invert to quartz, it would amorphize with density higher than ordinary silica glass. Quartz will not melt metastably or transform to tridymite due to slow kinetics. Thus only quartz and dense amorphous glass can be recovered. The latter could be diaplectic glass. (IV) $P_H > 36$ GPa, $T_R > 1700$ K and Recovery = ordinary glass. Both stishovite and quartz (no matter what the mass fraction is at post-shock state) will melt and ordinary glass formed from silica melt is the only phase in recovery. We summarized in Table 5.4 the above results as a pressure-temperature scale for impact events involving quartz.

In the above discussion, we assumed frozen-phase release which is not necessarily true for all pressures. We already demonstrated that T_R from non-frozen phase release is slightly lower than T_R in frozen release (Table 5.3), and it will not change our results. The above analysis indicates that shock recovery of a large fraction of stishovite is essentially impossible, as predicted by *Skinner and Fahey* [1963], although some stishovite can be recovered by special experiment design (*e.g.*, *Kleeman and Ahrens* [1973]). Shear melting related phenomena (*e.g.*, lamellar features) could be present in low pressure recovery (*e.g.*, case II and III), but they are not dominant and are second order features. To first order, we can apply the pressure-temperature scale from frozen-phase release to impact events involving quartz. Interestingly, despite careful consideration here of the kinetics and stability of many possible phases, our results are not dramatically different from *Stöffler* [1971] based on earlier calculations of shock and post-shock temperature [*Wackerle*, 1962]. As shown next, predictions with our scale (Table 5.4 and Figure 5.7) agree well with recovery experiments.

Many recovery experiments have been conducted on silica. Recovered material from quartz shock loaded to 60 GPa is amorphous with density of ordinary silica [*DeCarli and Jamieson*, 1959], indicating glass formed from melting as predicted by our calculation. At 35 GPa, recovered material has density of 2.64 g/cm^3 and broadened X-ray peaks of α-quartz [*DeCarli and Jamieson*, 1959], consistent with a small fraction of dense amorphous silica. Similarly, *DeCarli and Milton* [1965] recovered predominantly quartz with minor short-range-order (SRO) (possibly due to minor shear melting) and trace stishovite at $14 - 16$ GPa (at 16 GPa, we predict 2% stishovite is formed at shock). From 25 GPa *Wackerle* [1962] recovered essentially quartz, and from about 50 GPa, ordinary glass with density 2.2 g/cm^3.

This work demonstrates that the phases recovered are not necessarily the same as those at post-shock state or peak shock state. While the shock state and release path are constrained with confidence, the phase changes between recovery and post-shock state are not. This part of the process depends on size-dependent sample-environment

Table 5.4: A pressure-temperature scale for impact events involving quartz

	P_H (GPa)	T_H (K)	Phases on Hugoniot	P_H (GPa)	T_R (K)	Phases Recovered
I	$0 - 15$	$300 - 500$	quartz	$0 - 15$	$300 - 450$	quartz
II	$15 - 46$	$500 - 2600$	quartz, stishovite	$15 - 26$	$450 - 900$	quartz, trace stishovite
III	$46 - 77$	$2600 - 4700$	stishovite	$26 - 36$	$900 - 1700$	quartz, diaplectic glass
IV	$77 - 110$	$4700 - 6850$	superheated stishovite	> 36	> 1700	ordinary glass
V	> 110	> 5000	melt	-	-	-

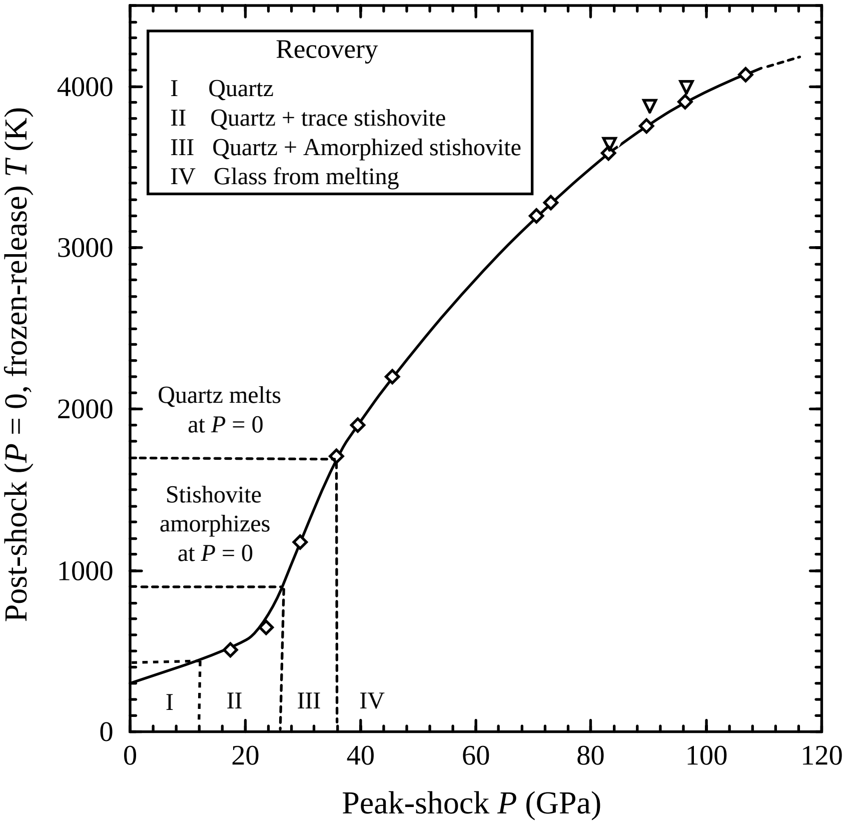

Figure 5.7: Frozen-phase release post-shock temperature *vs.* peak-state shock pressure. Diamonds: calculated; inverted triangles, measurements [*Boslough*, 1988]. The regimes of recovery state are marked (see Table 5.4).

interaction, particularly heat conduction to the surroundings. For example, the temperature of the post-shock state upon release of shocked quartz from $P_H = 70$ GPa suggests complete post-shock melting and recovery of ordinary glass. However, there is a narrow range near our example H_2 where the post-shock state includes stishovite which might, with a rapid enough quench, be recoverable. Furthermore, in the interpretation of recovered samples from natural impacts, porosity and impurities such as water content need also be taken into account.

5.5 Conclusion

We computed the thermodynamic states along the principal Hugoniot (including mixed-phase regime) of quartz and frozen-phase release paths based on classical Debye-Grüneisen theory, and quantified the phases, mass fractions and temperatures. Along the Hugoniot, direct conversion to stishovite in the range $15-46$ GPa is preferred over any pressure-induced amorphization mechanism. Superheating of stishovite along the Hugoniot between $77-110$ GPa is confirmed. Comparison to the phase diagram of silica shows that the frozen release paths may enter the stability fields of quartz or liquid, and cross the metastable (cold) melting curve of stishovite, suggesting that releases may not maintain frozen phase assemblages. This is supported by $P-V$ release paths converted from measurements on $P-u_p$ assuming isentropic release. Shock temperature and post-shock temperature calculations with frozen or non-frozen release yielded values in accord with shock and post-shock temperature measurements. This validates the method of measuring post-shock temperature but shows the poor sensitivity of such measurements to phase transitions during decompression compared to volume information, at least for silica. The isentropic assumption appears yield useful first order results even for non-frozen release.

The phase proportions in the computed Hugoniot states and the frozen-phase release temperatures provide an appropriate pressure-temperature scale for impact events involving quartz. It is necessary to distinguish recovered phases and phases produced upon shock loading and unloading. The proposed scale is consistent with previous shock recovery experiments and demonstrate that while recovery of trace quantities of stishovite is straightforward, the recovery of high-purity bulk stishovite from shock loading on quartz does not occur without special quenching mechanisms.

Acknowledgement: We appreciate helpful discussions with Z. R. Wang, D. Andrault and O. Tschauner. T. J. Ahrens and P. D. Asimow contributed partly to this work.

Chapter 6

Maximum Superheating and Undercooling: Systematics, Molecular Dynamics Simulations, Dynamic Experiments and Applications to High-Pressure Melting

Abstract

The maximum (or minimum) temperature (T_c) achievable in superheated solid (or undercooled liquid), depends on material property β inherently and heating (or cooling) rates (Q). β is the dimensionless energy barrier for nucleation of melt (or crystal), defined as $\beta = 16\pi\gamma_{sl}^3/(3kT_m\Delta H_m^2)$ where γ_{sl} is solid-liquid interfacial energy, ΔH_m heat of fusion, T_m melting temperature and k Boltzmann's constant. The systematics of maximum superheating and undercooling ($\theta_c = T_c/T_m$) are established phenomenologically as $\beta = (A_0 - blogQ)\theta_c(1-\theta_c)^2$, where $A_0 = 59.39$, $b = 2.33$ and Q is in K/s. For a considerable number of elements and compounds investigated, β varies between $0.2-8.2$, corresponding to maximum superheating $\theta_c = 1.06-1.35$ and $1.08-1.43$ at $Q \sim 1$ and 10^{12} K/s, respectively. Such systematics predict that a liquid with certain β can not crystallize at cooling rates higher than a critical value. The largest possible maximum undercooling ($\theta_c = 1/3$) is achievable by increasing cooling rate. Systematic molecular dynamics (MD) simulations ($Q \sim 10^{12}$ K/s) at ambient and high pressures are conducted on close-packed metals with Sutton-Chen many-body potentials. The maximum superheating and undercooling resolved from single- and two-phase simulations, are self-consistent with regard to the $\theta_c-\beta-Q$ systematics for superheating and undercooling. The systematics are also in accord with previous

MD melting simulations on other materials (*e.g.*, silica, Ta and ϵ-Fe) described by different force fields such as Morse-stretch charge equilibrium and embedded-atom-method potentials. Thus, the $\theta_c - \beta - Q$ systematics for maximum superheating and undercooling are validated at the level of interatomic interactions. Upon ultrafast heating, the inherent kinetics of melting may give rise to significant superheating. We demonstrate that the amount of superheating achieved in dynamic experiments ($Q \sim 10^{12}$ K/s) such as planar shock-wave loading and intense laser irradiation, agrees with the superheating systematics. We apply the shock-induced superheating to deriving the high-pressure melting parameters of geophysically important materials based on Lindemann's law and the $ln2$ rule for entropy of melting.

6.1 Introduction

Melting of crystals and crystallization of liquids are of scientific and technological significances. Metastable superheating and undercooling, are inherent in melting and freezing processes. A fundamental issue of immediate theoretical and experimental interests is to what extent a solid can be superheated and a liquid undercooled. Tremendous undercooling experiments have been conducted to probe the maximum undercooling on elements and compounds [*Kelton*, 1991], and appreciable amount of undercooling has been observed as homogeneous nucleation of crystals in liquids is more attainable experimentally. On the other hand, superheating has been observed in very few cases by special experimental designs [*Uhlmann*, 1980], due to the fact that heterogeneous nucleation is dominant in most melting experiments with low heating rates. Heterogeneous nucleation of melt is favored at sites with free surfaces, defects and impurities which significantly lower the energy barriers for nucleation. Predicting the maximum superheating is particularly challenging due to a paucity in experimental data.

High-pressure melting in experiments employing static (*e.g.*, diamond-anvil cell) and dynamic (*e.g.*, planar shock-wave loading) techniques is of great interest. Shock-state sound-speed and temperature measurements on metals, alkali halides and silicates have demonstrated unambiguously special melting behavior distinct from equilibrium melting, and superheating has been utilized to interpret the sharp drop in temperature on Hugoniot [*Lyzenga et al.*, 1983; *Boness and Brown*, 1993; *Yoo et al.*, 1993]. The apparent superheating in ultrafast dynamic loading, indicates the important role of heating rates in achieving superheating. Besides probing the fundamental limit of superheating and undercooling, the present study is also motivated by the issues as to the interpretation of temperature measurements in shock melting experiments [*Lyzenga et al.*, 1983; *Boness and Brown*, 1993; *Yoo et al.*, 1993; *Dai et al.*, 2001], and whether the striking discrepancies between the melting temperatures obtained from shock-wave loading and recent much lower diamond-anvil cell (DAC) results [*Errandonea et al.*, 2001] for transition metals such as Fe, V, Mo, W, and Ta, can be simply attributed to the effect of superheating.

The earliest work on the criteria for melting include Lindemann's criterion [*Lindemann*, 1910] and Born (shear) instability [*Born*, 1939; *Wang et al.*, 1997]. Previously, there were a few theoretical attempts in defining the limit of superheating. Catastrophic theories proffered involve the catastrophe of entropy [*Fecht and Johnson*, 1983], rigidity and volume [*Tallon*, 1989] upon melting. Other efforts to describe superheating utilized kinetic nucleation theory [*Lu and Li*, 1998; *Rethfeld et al.*, 2002]. Yet, a systematic and realistic description (either phenomenological or first-principles) of the limit of superheating and undercooling was not available. A recent development on superheating systematics relates superheating to well-defined undercooling parameters and the systematics of energy barrier for nucleation, and incorporates heating rates [*Luo and Ahrens*, 2003a]. In this work, we extend our previous efforts to present detailed treatment on the systematics of maximum undercooling and superheating, molecular dynamics (MD) simulations of superheating and undercooling, dynamic melting experiments and physical implications.

6.2 Systematics of maximum undercooling and superheating

We start with classical theory of homogeneous nucleation. The reason for the choice of homogeneous as opposed to heterogeneous nucleation is 2-fold: heterogeneous nucleation theory is difficult to implement in a systematic study because it requires detailed information such as characteristics of heterogeneous nucleants that are not available in general, and by careful experimental design, heterogeneous nucleation can be circumvented as demonstrated by undercooling and superheating experiments [*Kelton*, 1991; *Uhlmann*, 1980]. On the other hand, given possible heterogeneous nucleation in reality, homogeneous nucleation theory supplies an upper bound to the maximum undercooling and superheating. For steady-state homogeneous nucleation of crystal (*e.g.*, in liquid metals), the time for nuclei growth is negligible compared to that required for nucleation [*Singh and Holz*, 1983], thus only the nucleation aspects will be concerned. Indeed, catastrophic increase in nucleation rate near the maximum undercooling (superheating) dominates the process of creating or breaking the long-range order. Given the inherent complications and poor understanding of nucleation from first principles, our discussion based on classical nucleation theory is phenomenological in nature, but we can gain physical insights into superheating and undercooling and make sensible predictions. There are various treatments of nucleation [*Turnbull*, 1956; *Christian*, 1965; *Walton*, 1969; *Motorin and Musher*, 1984; *Kelton*, 1991; *Shao and Spaepen*, 1996] and they share a common form for steady-state nucleation rate per unit volume I

$$I = M(m,T)exp\{-\frac{\Delta G_c}{kT}g(\phi)\} \tag{6.1}$$

where M is a function of material properties m and temperature T, ΔG_c is the critical Gibbs free energy for nucleation, k Boltzmann's constant, and $g(\phi)$ a geometrical factor depending on wetting angle ϕ of a heterogeneous nucleant. $g(\phi) = 1$ for homogeneous nucleation, the case assumed in the following discussions. Consider a spherical liquid nucleus of critical radius within a superheated crystal lattice (similar for nucleation of crystal from an undercooled liquid), the critical nucleation energy $\Delta G_c = 16\pi\gamma_{sl}^3/(3\Delta G_{sl}^2)$ where γ_{sl} is the solid-liquid interfacial energy, and ΔG_{sl} the Gibbs free energy difference per unit volume between solid and liquid state, approximated as $\Delta H_m(T-T_m)/T_m$ where ΔH_m is heat of fusion and T_m melting temperature (assuming heat capacities of liquid and solid are approximately equal [*Turnbull*, 1952; *Kelton*, 1991]). The temperature dependence of M-term in I is negligible compared to that of the exponential term involving ΔG_c, thus M can be regarded as a constant [*Kelton*, 1991; *Porter and Easterling*, 1981], I_0. We define the energy barrier for nucleation, β, as a dimensionless quantity,

$$\beta(\gamma_{sl}, \Delta H_m, T_m) = \frac{16\pi\gamma_{sl}^3}{3\Delta H_m^2 k T_m} \tag{6.2}$$

and introduce reduced temperature, $\theta = T/T_m$. Thus $I = I_0 f(\beta, \theta)$ with

$$f(\beta, \theta) = exp\{-\frac{\beta}{\theta(\theta-1)^2}\}. \tag{6.3}$$

The prefactor I_0 can be obtained experimentally or theoretically. This functional form applies to both melting and freezing cases. Nucleation is essentially controlled by $f(\beta, \theta)$, *i.e.*, by the dimensionless energy barrier β at given temperature. The form of $f(\beta, \theta)$ is simple but it does reflect the fundamental physics of nucleation (Figure 6.1). During superheating ($\theta > 1$) of solids, f (*i.e.*, normalized nucleation rate) increases with temperature monotonically, as the mobility of atoms and the chemical driving force for melt nucleation both increase with T. On the other hand, during undercooling of liquids, the chemical driving force induced by undercooling is partly offset by the decrease in mobility, thus we have a maximum for f at $\theta = 1/3$. Although diffusion process is not explicitly included in f, it is well accounted for by the functional form of f.

Note that $f(\beta, \theta)$, β and θ are all dimensionless, allowing direct meaningful comparison of these quantities for different materials. β is characteristic of material itself,

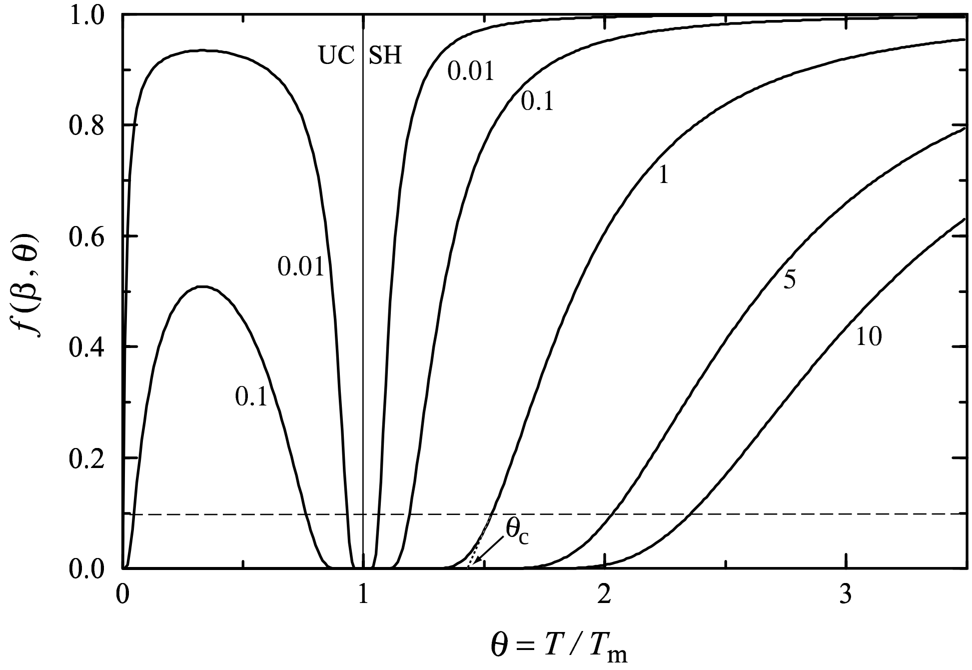

Figure 6.1: $f(\beta, \theta)$ *vs.* reduced temperature θ for different values of β. Each curve is labeled with the adopted value of β. UC denotes undercooling and SH superheating. θ_c is the critical temperature of maximum superheating, schematically obtained by drawing a tangent to f at $f = f_0$ (dashed line) and intersecting θ-axis.

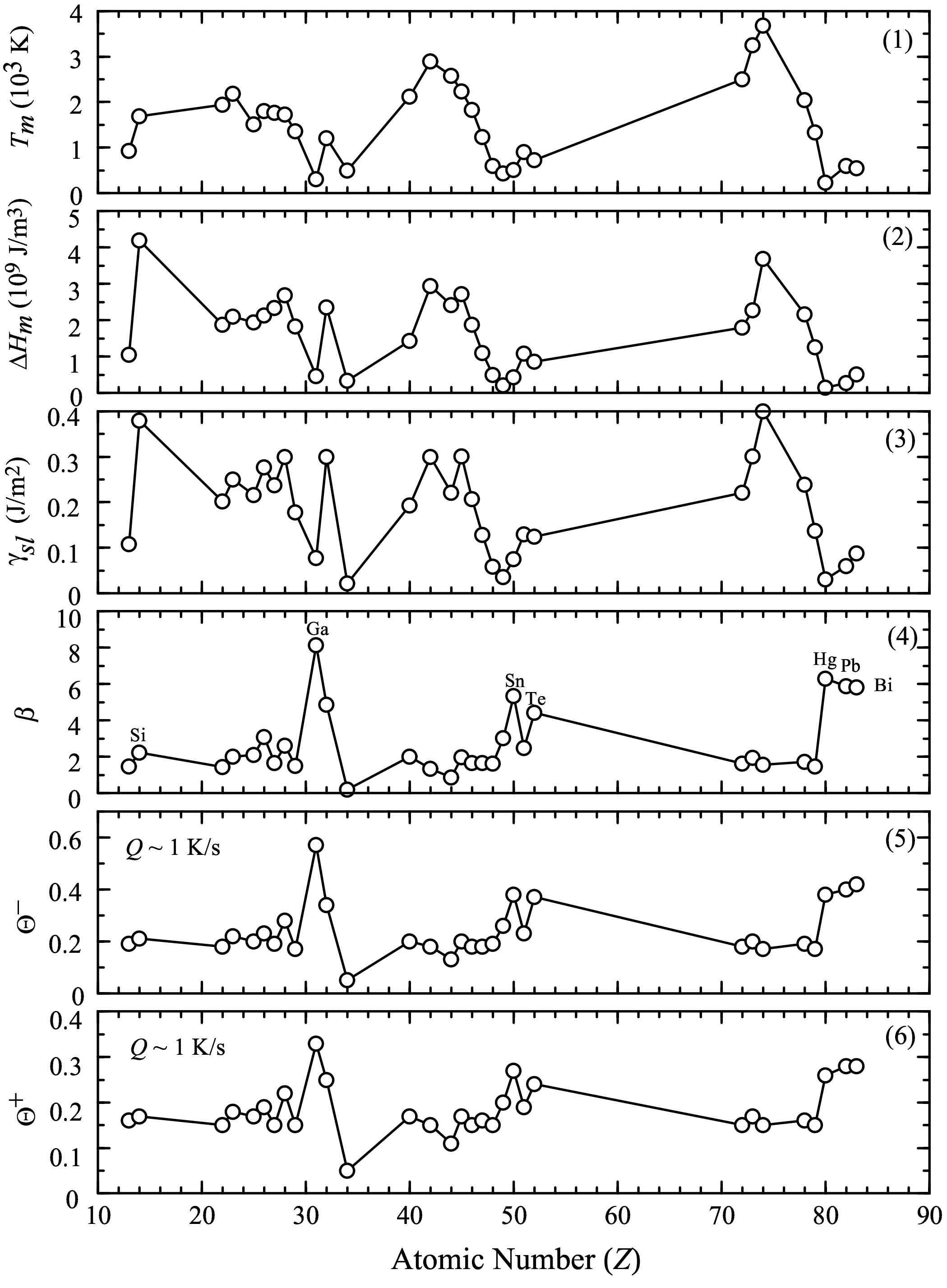

Figure 6.2: Atomic number (Z) vs. melting point (T_m), heat of fusion (ΔH_m), solid-liquid interfacial energy (γ_{sl}), normalized energy barrier for nucleation (β), experimental undercooling (Θ^-) and calculated superheating (Θ^+) at $Q \sim 1$ K/s. These parameters are indexed as $1-6$, respectively. Values for T_m, ΔH_m and γ_{sl} are from literature [*Kelton*, 1991; *Shao and Spaepen*, 1996].

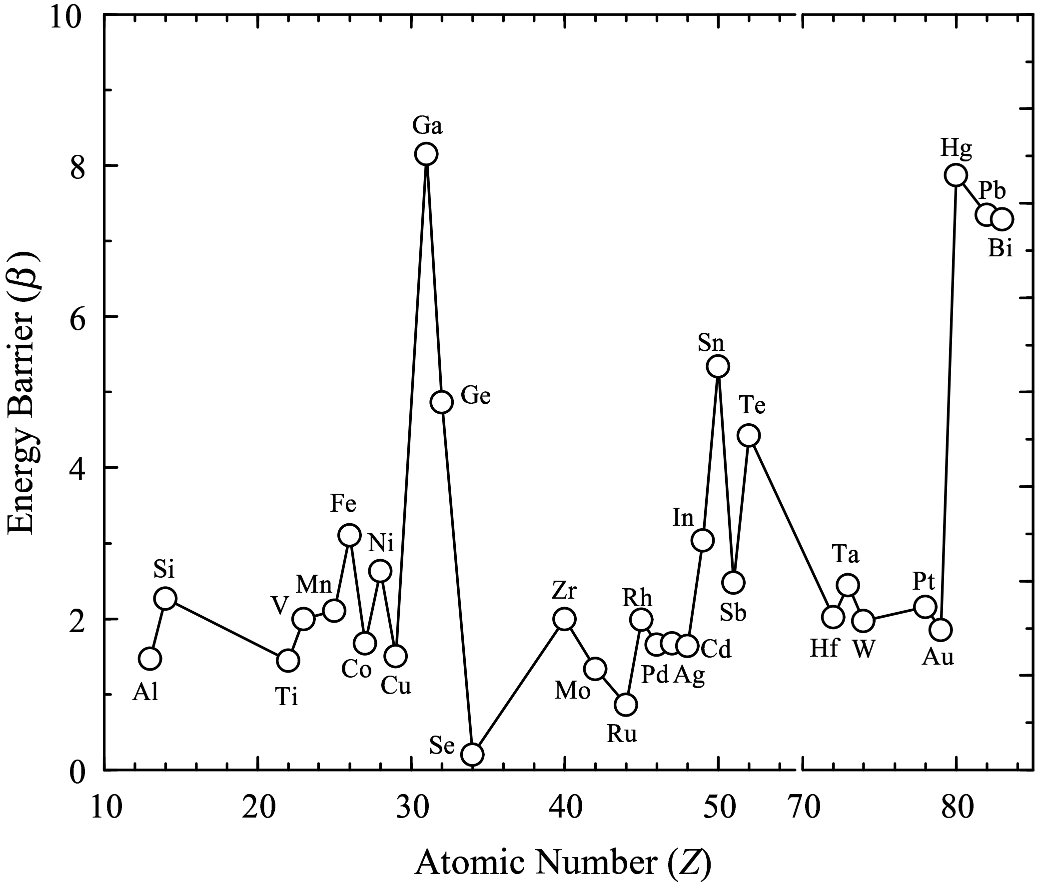

Figure 6.3: Normalized energy barrier β vs. atomic number Z.

depending on γ_{sl}, ΔH_m and T_m. To estimate the value of β, we start with a hard sphere system (hss) due to its simplicity and theoretical significance. Let the diameter of hard sphere be σ. The solid-liquid interfacial energy for a hard sphere system (γ_{sl}^{hss}) [*Davidchack and Laird*, 2000] is shown to be $0.61kT/\sigma^2$. Heat of fusion [*Hoover and Ree*, 1968] for a hss, $\Delta H_m^{hss} = 1.16kT$. Thus, $\beta \sim 0.77$ for a hard sphere system. We may expect for a real system, the value of β is of similar magnitude. For a real system, $\gamma_{sl} \sim 0.1$ J/m^2, $T_m \sim 10^3$ K and $\Delta H_m \sim 10^9$ J/m^3 yield $\beta \sim 1.2$. Undercooling experiments with homogeneous nucleation have been well documented in the literature (*e.g.*, for elements [*Kelton*, 1991; *Shao and Spaepen*, 1996]) (Table 6.1). The elements studied include transition metals, simple metals and semiconductors in the 3rd-6th row of the periodic table. Elements are simple by themselves, and their physical properties vary dramatically due to the variations in electronic structure. Their character may be regarded as typical of materials. Given T_m, ΔH_m and γ_{sl} (Figure 6.2), values of β for these elements are readily calculated as shown in Figures. 6.2-6.3. Transition metals (Group IVB-IIB) have relatively constant value of β with an average close to 2, except for Hg ($\beta = 6.30$). Group IIA-VIA elements have significantly higher values of β, with maximum at Ga ($\beta = 8.15$) except for Al ($\beta = 1.47$) and Se which has the lowest $\beta = 0.20$. This does reflects the periodic variations in electronic structure in a general sense. To explore the systematics of material property β given T_m, ΔH_m and γ_{sl} (indexed as 1-3 respectively in Figure 6.2), we calculate the cross-correlation coefficients among these parameters (Table 6.2). As $R_{ij} = 0.81 - 0.97$ $(i, j = 1, 2, 3)$, T_m, ΔH_m and γ_{sl} vary with atomic number Z in similar manners. In particular, $R_{23} = 0.97$ for γ_{sl} and ΔH_m. This indicates that compared to T_m, ΔH_m is a better indicator of γ_{sl} which is difficult to measure. $R_{ij} \sim 1$ also implies that these three parameters can be attributed to the same physics, *e.g.*, binding energy although it is more directly related to heat of vaporization. γ_{sl} increases with T_m and ΔH_m. Thus, although β is sensitive to γ_{sl}, variation in β induced by that in γ_{sl} could be offset by those in T_m and ΔH_m. It is demonstrated that $\gamma_g/(\Delta H_m V) \sim$ constant for a variety of elements and compounds [*Kelton*, 1991; *Uhlmann*, 1980]. The gram-interfacial energy $\gamma_g = \gamma_{sl} V^{2/3} N_A^{1/3}$ where V is molar volume and N_A Avogadro's number. As

$\Delta H_m = T_m \Delta S_m$ where ΔS_m is the entropy of fusion, thus $\beta \propto \Delta S_m V$, and should vary in a narrow range for different materials. Similar argument can be made with $\gamma_{sl} \propto \Delta H_m / a^2$ where a^2 is the effective atomic surface area [*Walton*, 1969]. Using the same arguments, β of most solids under high pressures (*e.g.*, megabar under shock compression) should be of the same order as at ambient pressure. Cross-correlating β (indexed as 4 in Figure 6.2) to T_m, ΔH_m and γ_{sl}, yields negative values between -0.57 and -0.38 (Table 6.2).

Given the systematics of β, next we explore the relationship of T_m, ΔH_m, γ_{sl} and β to the maximum undercooling and superheating, denoted as $\theta_c = T_c/T_m$ where T_c is the highest (lowest) temperature in superheated solid (undercooled liquid). The maximum undercooling is also referred to as $\Theta^- = 1 - \theta_c$ and superheating as $\Theta^+ = \theta_c - 1$. The cooling rate $Q \sim 1$ K/s is typical in conventional undercooling experiments, and the experimental values of Θ_s^- (subscript s refers to $Q \sim 1$ K/s, and ns to 10^{12} K/s) for elements and calculated Θ_s^+ (discussed next) are plotted in Figure 6.2 (indexed as 5 and 6, respectively). Θ_s^- and Θ_s^+ increase with β as cross-correlation yields $R_{45} = 0.98$ and $R_{46} = 0.96$ (Table 6.2). On the contrary, Θ_s^- (Θ_s^+) correlates poorly with any of γ_{sl}, T_m and ΔH_m. This makes perfect sense because the nucleation rate I depends on all of these three parameters. Thus, β as an integral part of γ_{sl}, T_m and ΔH_m best describes the nucleation rate and fully represents variations in the maximum undercooling and superheating. It also contends conventional wisdom that material with low T_m should have smaller maximum superheating (undercooling). The extreme counter examples are Ga and Hg, which have low T_m (303 and 234 K, respectively) but high Θ_s^- (0.57 and 0.38). Indeed, relative to γ_{sl} and ΔH_m, T_m is better anti-correlated with Θ^- and β: most low-T_m materials have high values of β and Θ_s^- (Figure 6.2). But this should not be over-interpreted, as $R_{24} = -0.57$ which is far way from -1. Thus the best parameter for study nucleation of melt (crystal), is β. The physical meaning of β is inherent in its relation to γ_{sl}, T_m and ΔH_m, in turn whose physics dwells on nucleation theory. Simply, β is an integral of these three parameters.

In contrary to undercooling experiments with $Q \sim 1$ K/s, few experiments have

Table 6.1: Nucleation parameters for elements, experimental values of Θ_s^- and predicted superheating and undercooling at different heating (cooling) rates based on systematics. s, ms and ns refer to $Q = 1$, 10^6 and 10^{12} K/s, respectively. $\Theta^+ = \theta_c - 1$ and $\Theta^- = 1 - \theta_c$.

Element	Z	T_m (K)	V (cm^3/mol)	γ_{sl} (J/m^2)	ΔH_{mm} (kJ/mol)	β	$\Theta_{s,exp}^-$	Θ_s^-	Θ_{ms}^-	Θ_{ns}^-	Θ_s^+	Θ_{ms}^+	Θ_{ns}^+
Ag	47	1234	10.27	0.128	11.40	1.67	0.180	0.187	0.217	0.269	0.157	0.177	0.209
Au	79	1336	10.19	0.137	12.80	1.48	0.170	0.175	0.202	0.250	0.148	0.167	0.198
Cd	48	594	12.99	0.058	6.40	1.64	0.190	0.185	0.214	0.266	0.155	0.175	0.208
Co	27	1765	6.61	0.238	15.50	1.69	0.190	0.188	0.218	0.271	0.158	0.178	0.210
Cu	29	1356	7.11	0.178	13.00	1.51	0.170	0.177	0.205	0.253	0.150	0.169	0.200
Fe	26	1809	7.10	0.277	15.20	3.11	0.230	0.269	0.317	0.408	0.209	0.236	0.278
Hf	72	2500	13.41	0.221	24.10	1.62	0.180	0.184	0.213	0.264	0.155	0.174	0.206
Hg	80	234	14.82	0.031	2.32	6.30	0.380	0.436	0.564	0.667	0.288	0.324	0.380
Mn	25	1517	7.53	0.216	14.70	2.12	0.200	0.214	0.249	0.313	0.175	0.198	0.233
Mo	42	2896	9.39	0.300	27.60	1.31	0.180	0.163	0.189	0.233	0.140	0.158	0.187
Ni	28	1728	6.59	0.300	17.70	2.63	0.280	0.243	0.285	0.361	0.194	0.218	0.257
Pd	46	1825	8.85	0.207	16.70	1.66	0.180	0.186	0.216	0.268	0.156	0.176	0.209
Pt	78	2042	9.09	0.239	19.70	1.73	0.190	0.191	0.221	0.275	0.159	0.180	0.213
Rh	45	2239	8.30	0.301	22.60	1.99	0.200	0.207	0.240	0.300	0.170	0.192	0.227
Ru	44	2583	8.12	0.221	19.70	0.86	0.130	0.130	0.149	0.183	0.115	0.130	0.154
Ta	73	3253	10.84	0.301	24.70	1.96	0.200	0.205	0.238	0.297	0.169	0.190	0.225
Ti	22	1940	9.98	0.202	18.80	1.45	0.180	0.173	0.200	0.247	0.147	0.166	0.196
V	23	2183	8.34	0.250	17.60	1.95	0.220	0.204	0.237	0.296	0.168	0.190	0.225
W	74	3683	9.54	0.400	35.20	1.55	0.170	0.179	0.208	0.257	0.151	0.171	0.202
Zr	40	2125	14.02	0.193	20.10	2.00	0.200	0.207	0.241	0.301	0.170	0.192	0.227
Al	13	933	9.96	0.108	10.50	1.47	0.190	0.174	0.201	0.249	0.148	0.167	0.197
Bi	83	544	21.35	0.088	10.90	5.83	0.420	0.410	0.514	0.667	0.278	0.313	0.368
Ga	31	303	11.80	0.077	5.59	8.15	0.570	0.563	0.667	0.667	0.324	0.363	0.426
Ge	32	1210	13.65	0.300	32.20	4.87	0.340	0.360	0.436	0.667	0.257	0.289	0.339
In	49	430	15.71	0.036	3.27	3.04	0.260	0.265	0.312	0.401	0.207	0.233	0.275
Pb	82	601	18.27	0.060	4.98	5.87	0.400	0.412	0.518	0.667	0.279	0.314	0.369
Sb	51	904	18.23	0.130	19.90	2.48	0.230	0.235	0.274	0.347	0.188	0.212	0.251
Se	34	490	18.49	0.021	6.28	0.20	0.050	0.060	0.069	0.083	0.057	0.064	0.077
Si	14	1685	12.05	0.380	30.03	2.24	0.210	0.220	0.260	0.326	0.180	0.200	0.240
Sn	50	505	16.25	0.075	7.08	5.34	0.380	0.384	0.472	0.667	0.268	0.301	0.354
Te	52	723	20.45	0.125	17.60	4.43	0.370	0.337	0.405	0.574	0.246	0.277	0.325

Table 6.2: Cross-correlation coefficient R_{ij}. T_m, ΔH_m, γ_{sl}, β, Θ^- and Θ^+ are indexed as $1-6$, respectively (also see Figure 6.2).

R_{12}	R_{13}	R_{23}	R_{14}	R_{24}	R_{34}	R_{45}	R_{46}	R_{56}
0.81	0.84	0.97	-0.57	-0.46	-0.38	0.98	0.96	0.98

achieved appreciable superheating at heating rates of ~1 K/s, as heterogeneous nucleation is dominant at such low heating rates due to surface melting and the effect of defects such as grain boundaries. It would be of great interest to predict the maximum undercooling and superheating under various cooling (heating) rates, say, $Q \sim 10^{12}$ K/s. Given the β systematics and experimental values of Θ_s^-, next we will develop a Q-dependent scheme to predict undercooling and superheating under typical cooling and heating rates.

For steady-state homogeneous nucleation of crystal in liquid (melt in crystal), the probability [*Kelton*, 1991] x for a given amount of parent phase of volume v containing no new phase under certain cooling (heating) rate Q is

$$x = exp\{\pm\frac{vT_mI_0}{Q}\int_{\theta_c}^{1} f(\beta,\theta)d\theta\} \tag{6.4}$$

where + refers to superheating and $-$ to undercooling. The parameters for undercooling experiments at $Q \sim 1$ K/s, such as γ_{sl}, ΔH_m, T_m (thus β), x and v can be regarded as equal to those for superheating and undercooling at different heating (cooling) rates. Further, we assume I_0 is roughly the same for undercooling and superheating case. Thus, the maximum superheating and undercooling under any Q, can be calculated from experimental value of Θ_s^-. For example, superheating Θ^+ at any heating rate Q can be solved from

$$\frac{1}{Q}\int_{1}^{(1+\Theta^+)} f(\beta,\theta)d\theta = \frac{1}{Q_0}\int_{(1-\Theta_s^-)}^{1} f(\beta,\theta)d\theta \tag{6.5}$$

where $Q_0 = 1$ K/s. Similarly, undercooling Θ^- under other cooling rates Q, can be readily calculated. Thus for a given material with β and Θ_s^-, we can predict the maximum superheating and undercooling at any heating (cooling) rates (Table 6.1). Figure 6.4 shows experimental value of the maximum undercooling ($\theta_c = 1 - \Theta_s^-$, circles) and calculated maximum superheating $\theta_c = 1 + \Theta_s^+$ (diamonds) at $Q = 1$ K/s for elements. Note that heating (cooling) rates such as 1 and 10^{12} K/s should be regarded as typical but exact, as a factor of 10^2 in Q would yield negligible changes θ_c (except for high-β elements such as Ga upon undercooling), due to the functional form of $f(\beta, \theta)$. In the case of calculating maximum undercooling at high cooling rates, Θ^- might be 1 (*i.e.*, $T_c = 0$). For instances, $\Theta^- = 1$ for Ga at $Q = 10^6$ K/s, and for Bi, Ga, Pb, Sn and Te at $Q = 10^{12}$ K/s. $\Theta^- = 1$ indicates that under such cooling rates, these liquids cannot solidify as crystals.

In the absence of first-principles formulations relating material property β, heating (cooling) rate Q and maximum superheating (undercooling) θ_c as obtained above, we fit these parameters to an analytical form,

$$\beta = A(Q)\theta_c(\theta_c - 1)^2 \tag{6.6}$$

where A is a fitting constant depending on Q. Separate fittings for undercooling and superheating cases yield similar A, indicating that this functional form describes both superheating and undercooling with a single $A(Q)$. Such fittings to both superheating and undercooling yield $A(Q) = 58.8523$, 45.4269 and 31.5746 for 1 K/s, 10^6 and 10^{12} K/s respectively and plotted in Figure 6.4. While its exact physical meaning is not clear, A could be regarded as defining a relative characteristic time scale for nucleation at various heating (cooling) rates. Similar fittings have been conducted at various Q, and A is found to linearly depend on $logQ$. Thus we can rewrite Eq. (6.6) as

$$\beta = (A_0 - blogQ)\theta_c(\theta_c - 1)^2 \tag{6.7}$$

where $A_0 = 59.39284$ and $b = 2.33395$, and Q is in K/s. Eq. (6.7) is referred to as the $\theta_c - \beta - Q$ systematics for maximum superheating and undercooling.

There are some important features in the $\theta_c - \beta - Q$ systematics [Eq. (6.7) and

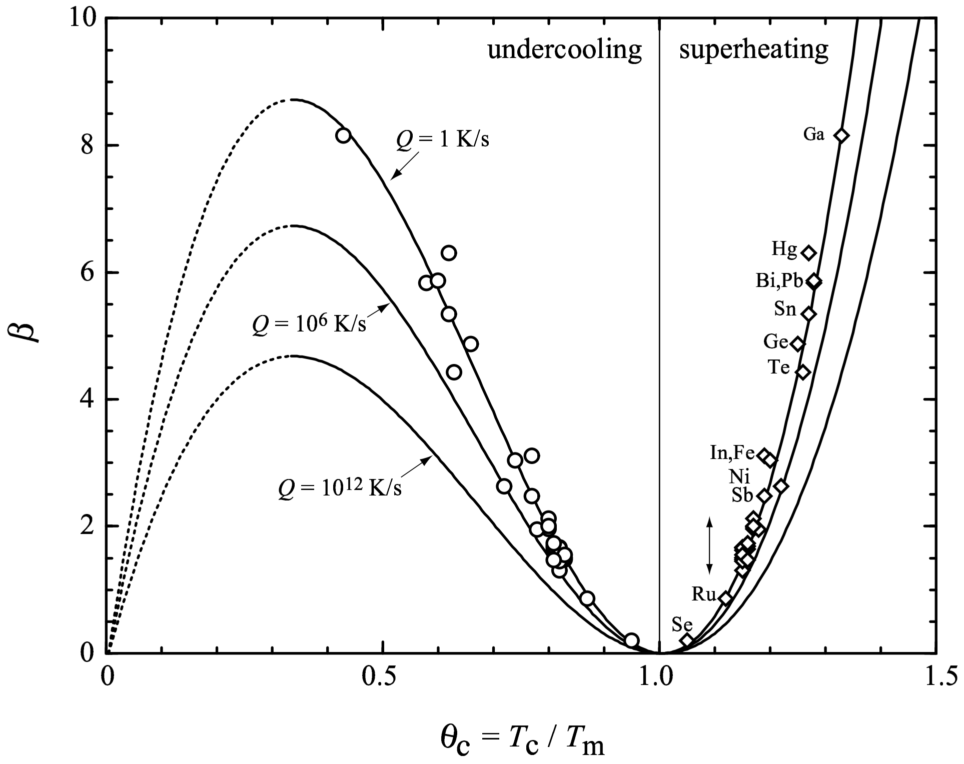

Figure 6.4: Maximum superheating-undercooling systematics for elements: $\beta = (A_0 - blogQ)\theta_c(1-\theta_c)^2$. Circles are experimental value of undercooling at cooling rate $Q \sim$ 1 K/s, and diamonds are calculated superheating at $Q \sim 1$ K/s. Solid curves are plots with $Q = 1$, 10^6 and 10^{12} K/s, respectively. Dotted curves denote the undercooling portions for $\theta_c = 0 - \frac{1}{3}$. The elements inside the arrow is Ti, Al, Au, Cu, Hf, Cd, Pd, Ag, Co, Pt, Ta, Rh, Zr, Mn, Si, Sb, Ni, In and Fe in β-increasing order.

Figure 6.4]. The functional form for $\theta_c - \beta - Q$ implies that $f(\beta, \theta_c) = exp[-A(Q)]$ and can be regarded as a universal constant at certain Q. This is in some sense similar to assuming universal constant [*Lu and Li*, 1998] for $I = 1$ cm^{-3}s^{-1} if I_0 does not vary much for different materials. Nucleation rate near θ_c dominates the nucleation process during undercooling and superheating. As shown in Figure 6.4, there is an asymmetry of the maximum superheating and undercooling θ_c (relative to $\theta_c = 1$) at the same Q, *i.e.*, for a material with certain β, it can achieve larger amount of maximum undercooling than maximum superheating. This makes sense in that a critical value of nucleation rate I_c, is more achievable for melting than freezing because of the difference in T. The increase of maximum superheating induced by increasing Q is less pronounced than undercooling case, *e.g.*, for Al, $\Theta^+_{ns} - \Theta^+_s = 0.07$ while $\Theta^-_{ns} - \Theta^-_s = 0.11$. Increasing Q does not significantly increase maximum superheating: a change in Q from 1 to 10^{12} K/s only yields a change of less than 10% in θ_c. The maximum $\Theta^+ < 0.5$ even at $Q = 10^{12}$ K/s. But increasing heating rate does serve as an important practical approach to achieving superheating as shown next. There is a maximum of β at $\theta_c = 1/3$ for any cooling rate, say, $\beta_{max} = 8.72$, 6.73 and 4.68 at 1, 10^6 and 10^{12} K/s respectively. This simply means that materials with $\beta > \beta_{max}$ cannot crystallize under cooling rates larger than corresponding Q. The physical cause can be traced back to the tradeoff between increasing chemical driving force for crystallization and decreasing atomic mobility while reducing temperature. The maximum possible undercooling for any material at any cooling rate is $\Theta^- = 2/3$. The largest Θ^-_s achieved is 0.57 for Ga. Possibly, there could exist an unknown element with $\beta = 8.72$ such that $\Theta^-_s = 0.67$. Increasing cooling rate may induce $\Theta^- = 2/3$, *e.g.*, such undercooling may be achieved for Ga at $Q \sim 10^2$ K/s. Materials with $\beta > \beta_{max} = \frac{4}{27}(A_0 - blogQ)$ will not crystallize at given cooling rate Q, and possibly liquids become glassified or stay as liquid, as the glass transformation temperature could be higher or lower than θ_c [*Weinberg*, 1986].

Previously, theories involving catastrophe in entropy [*Fecht and Johnson*, 1983], rigidity and volume [*Tallon*, 1989] predicted a wide range [*Lu and Li*, 1998] ($\Theta^+ = 0.3 - 2.0$) of maximum superheating. Other efforts [*Lu and Li*, 1998; *Rethfeld et al.*, 2002] to describe superheating assumed $I = 1$ cm^{-3}s^{-1} or a critical volume. Mostly heating rates were not considered. We have established the $\theta_c - \beta - Q$ systematics [Eq. (6.7) and Figure 6.4] based on undercooling experiments and homogeneous nucleation theory, and incorporated the effect of heating (cooling) rates. Maximum superheating at $Q = 1$ K/s predicted from Eq. (6.7) is slightly lower than those from *Lu and Li* [1998] (Table 6.3). $I = 1$ cm^{-3}s^{-1} is a reasonable first-order value at low Q. A direct application of the systematics is that given measured maximum undercooling and superheating, we can determine β and predict maximum superheating and undercooling at other heating (cooling) rates. The knowledge of β also allows an evaluation of γ_{sl} given ΔH_m and T_m which are in general available. Systematic undercooling experiments were conducted on alkali halides [*Walton*, 1969]. The interfacial energy and maximum undercooling and superheating at typical cooling (heating) rates, are obtained (Table 6.4). For example, the maximum superheating achievable for CsBr at 10^{12} K/s, is 0.20. Similarly, given superheating measurement on silicates [*Uhlmann*, 1980], we predict γ_{sl} and maximum undercooling and superheating under various Q (Table 6.4).

Thus we have established the $\theta_c - \beta - Q$ systematics [Eq. (6.7) and Figure 6.4] based on undercooling experiments and homogeneous nucleation theory.

6.3 Molecular dynamics simulations of superheating and undercooling

Molecular dynamics simulation is an important tool to study melting and freezing processes under various pressures. Microscopic examination of the melting and freezing process is also allowed from real-time trajectories. It has long been recognized that temperature hysteresis exists in MD simulations of bulk crystal with three-dimensional boundaries [*Allen and Tildesley*, 1987; *Jin and Lu*, 1998; *Stranchan et al.*, 1999; *Luo et al.*, 2002c]. But a systematic and quantitative examination of both superheating and undercooling in MD simulations, is not available. It is of

Table 6.3: Comparison of superheating from *Lu and Li* [1998] (assuming $I = 1$ cm^{-3}s^{-1}) and this work at 1 K/s.

	Sn	Pb	Sb	Al	Ag	Au	Cu	Mn	Ni	Co	Fe	Pd	Pt
Lu & Li	0.279	0.291	0.192	0.208	0.179	0.184	0.174	0.177	0.212	0.184	0.212	0.183	0.185
This work	0.265	0.280	0.188	0.158	0.155	0.145	0.150	0.170	0.216	0.154	0.190	0.154	0.156

Table 6.4: Undercooling and superheating of alkali halides and silicates. *a*: Θ_s^- from *Walton* [1969], and *b*: Θ_s^+ from *Uhlmann* [1980].

	T_m	γ_{sl}	ΔH_{mm}	β	Θ_s^-	Θ_{ns}^-	Θ_s^+	Θ_{ns}^+
	(K)	(J/m^2)	(kJ/mol)					
			Alkali halides ^{a}					
CsBr	909	0.066	23.58	1.56	0.18	0.26	0.15	0.20
CsCl	919	0.051	15.06	1.41	0.17	0.24	0.14	0.19
CsF	955	0.046	10.25	1.27	0.16	0.23	0.14	0.18
CsI	894	0.069	24.66	2.40	0.23	0.34	0.19	0.25
KBr	1003	0.063	20.92	1.27	0.16	0.23	0.14	0.18
KCl	1049	0.082	26.82	1.27	0.16	0.23	0.14	0.18
KI	959	0.047	17.15	1.27	0.16	0.23	0.14	0.18
LiBr	820	0.046	12.13	0.63	0.11	0.15	0.10	0.13
LiCl	887	0.086	13.39	2.05	0.21	0.31	0.17	0.23
LiF	1115	0.124	9.87	2.05	0.21	0.31	0.17	0.23
NaBr	1028	0.088	25.69	1.27	0.16	0.23	0.14	0.18
NaCl	1074	0.112	30.21	1.27	0.16	0.23	0.14	0.18
NaF	1261	0.206	29.29	2.22	0.22	0.32	0.18	0.24
RbCl	988	0.057	18.41	1.27	0.16	0.23	0.14	0.18
			Silicates ^{b}					
$NaAlSi_3O_8$	1371	0.088	63.00	1.52	0.18	0.25	0.15	0.20
SiO_2	1700	0.106	9.40	5.01	0.37	1.00	0.26	0.34

particular interest whether both superheating and undercooling in MD simulations are consistent with the superheating-undercooling systematics, *i.e.*, the phenomenological superheating-undercooling systematics [Eq. (6.7)] can be validated from the level of interatomic interactions. The heating (cooling) rate typical in conventional MD simulations, is on the order of 10^{12} K/s, comparable to light-gas gun shock-wave experiments and intense laser irradiation (see next section), thus melting and freezing simulations with MD could elucidate our understanding of superheating and undercooling in ultrafast heating (cooling) experiments.

A supercell with three-dimensional periodic boundaries, is subjected to step-by-step heating at constant pressure P (*e.g.*, with isothermal-isobaric statistical ensemble NPT where N is the total number of atoms in the supercell) until it melts, then the system is cooled down step by step until it refreezes. A hysteresis is obtained by such a stepped heating-cooling process. The melting temperature determined from "heat-until-it-melts" process (single-phase melting temperature, $T_{1,m}$) is higher than the equilibrium T_m as superheating is part of the hysteresis. On the other hand, the crystallization temperature from "cool-until-it-refreezes" (single-phase crystallization temperature, $T_{1,c}$) is lower than T_m. To quantify the amount of superheating and undercooling, we need to find the equilibrium melting temperature T_m. Given a specific force field (FF) describing interatomic interactions, T_m can be determined by such techniques as thermodynamic integration of free energy [*Frenkel and Smit*, 1996] and solid-liquid coexisting phase simulations [*Morris et al.*, 1994]. The latter is a natural choice for our purpose. Superheating and undercooling can be attributed to the nucleation process (overcoming the energy barrier for nucleation), and are circumventable by constructing a solid-liquid coexisting system (two-phase simulation) with planar solid-liquid interface. Nucleation problem of either solid or liquid and associated superheating or undercooling are avoided [*Morris et al.*, 1994]. Thus we can determine the equilibrium melting temperature (two-phase simulation, $T_{2,m}$) for the specific system with assigned FF. In this way, we can quantify the amount of the maximum superheating ($\Theta^{+}_{md} = T_{1,m}/T_{2,m} - 1$) and undercooling ($\Theta^{-}_{md} = 1 - T_{1,c}/T_{2,m}$) for the system. In this work, we conduct single- and two-phase simulations of melting and refreezing of close-packed metals. These simulations along with previous work, allow us to systematically examine superheating and undercooling behavior for elements and compounds described with different potentials against the superheating-undercooling systematics developed. The pressure effect on superheating is also addressed.

To simulate the close-packed (*fcc* and *hcp*) metals, we adopt Sutton-Chen many body potential (SC) [*Sutton and Chen*, 1990] with quantum corrections (qSC) [*Kimura et al.*, 1998]. For SC FF, the total potential energy of the system, U_{tot}, is

$$U_{tot} = \sum_i \epsilon[\sum_{j \neq i} \frac{1}{2} V(r_{ij}) - c\rho_i^{1/2}]. \tag{6.8}$$

The pair potential

$$V(r_{ij}) = (\frac{a}{r_{ij}})^n \tag{6.9}$$

accounts for the repulsion between the atoms i and j where r_{ij} is the separation between them. The many-body cohesion is accounted for with the local electron density on atom i

$$\rho_i = \sum_{j \neq i} (\frac{a}{r_{ij}})^m. \tag{6.10}$$

The parameters (a, ϵ, c, m, n) were obtained by optimization to best fit the empirical values including lattice parameter, cohesive energy, elastic constants and bulk modulus, phonon vibration frequencies, vacancy formation energy, surface energy, and equation of state. The quantum effect (*e.g.*, zero-point vibrational energy) was also included in optimization [*Kimura et al.*, 1998]. The parameters of such qSC force field for close-packed metals are listed in Table 6.5.

Given force field, we construct a supercell of 864 atoms (6 × 6 × 6) for each fcc metal and 1024 atoms (8 × 8 × 8) for Be with three-dimensional periodic boundaries. MD calculations are conducted with an NPT ensemble using a Hoover thermostat [*Hoover*, 1985] and a Rahman-Parrinello barostat [*Parrinello and Rahman*, 1981].

Table 6.5: The qSC FF for close-packed metals [*Kimura et al.*, 1998].

	a (Å)	ϵ (10^{-2} eV)	c	m	n
Be	3.18863	0.18207	222.34769	6	13
Al	4.03230	0.90144	54.97923	5	9
Ni	3.51570	0.73767	84.74500	5	10
Cu	3.60300	0.57921	84.84300	5	10
Rh	3.79840	0.24612	305.49900	5	13
Pd	3.88130	0.32864	148.20500	6	12
Ag	4.06910	0.39450	96.52400	6	11
Ir	3.83440	0.37674	224.81500	6	13
Pt	3.91630	0.97894	71.33600	7	11
Au	4.06510	0.78052	53.58100	8	11
Pb	4.94950	0.55772	45.88200	7	10

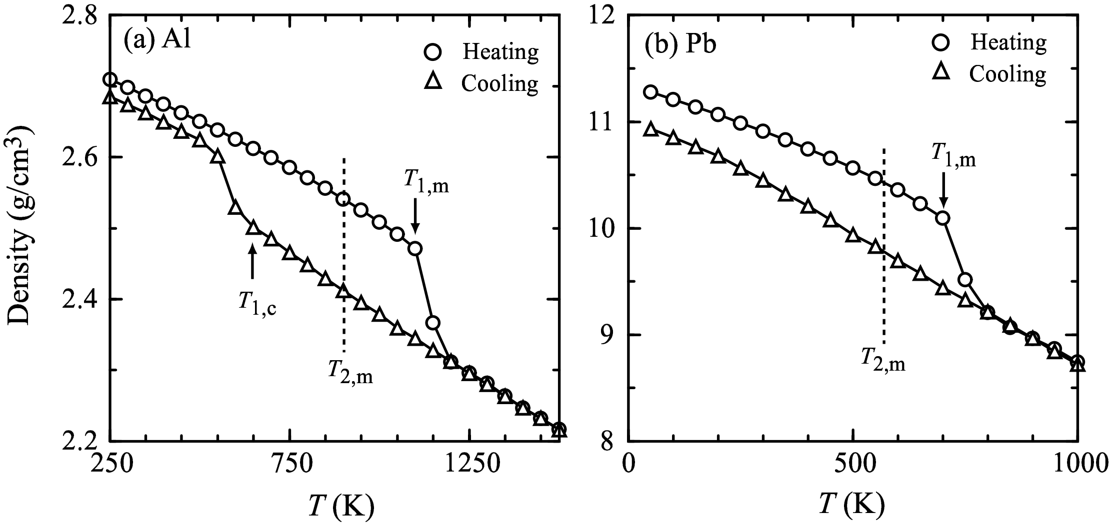

Figure 6.5: Typical single- and two-phase molecular dynamics simulations of the melting and refreezing behavior: density vs. T. A complete hysteresis of density forms during continuous heating-cooling process for Al (a), while for Pb (b) liquid becomes vitrified upon cooling. $T_{1,m}$ and $T_{1,c}$ are the single-phase melting and freezing temperature at superheated and undercooled state, respectively. $T_{2,m}$ is the equilibrium melting temperature from two-phase simulations.

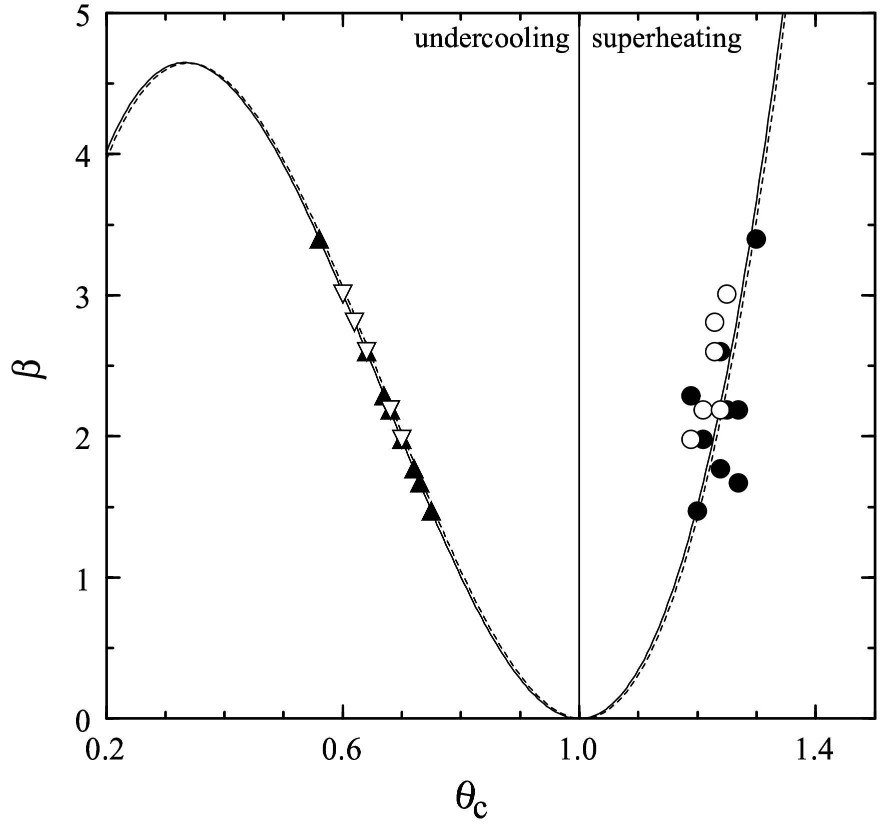

Figure 6.6: Deduced energy barrier β vs. maximum undercooling and superheating achieved (θ_c) in MD simulations for fcc metals and Be (hcp). Open symbols are for Al at $P = 0, 20, 40, 60, 80$ and 100 GPa, and filled symbols for other elements simulated with qSC force field. Solid curve is the plot of $\beta = (A_0 - blogQ)\theta_c(\theta_c - 1)^2$ with $Q = 10^{12}$ K/s. The dashed curve is the best fit of simulations to the same functional form as the superheating-undercooling systematics.

Table 6.6: Single- and two-phase MD simulations of melting and refreezing of metals at $P = 0$. *a*: Calculated from the superheating-undercooling systematics and Θ^+_{md}. *b*: Simulated with embedded-atom-method force field based on quantum mechanics calculations [*Stranchan et al.*, 2001].

	$T_{1,m}$ (K)	$T_{1,c}$ (K)	$T_{2,m}$ (K)	$T_{e,m}$ (K)	ΔH_m (kJ/mol)	γ_{sl} [a] (J/m^2)	Θ^-_{md}	Θ^-_{ns}	Θ^+_{md}	Θ^+_{ns}
Be	1600	900	1350	1560	15.55	0.053	0.33	-	0.19	-
Al	1100	650	925	933	9.08	0.108	0.30	0.25	0.19	0.20
Ni	1700	1000	1375	1728	13.55	0.085	0.28	0.36	0.24	0.26
Cu	1350	750	1070	1356	10.80	0.086	0.30	0.24	0.21	0.19
Rh	2700	1600	2125	2239	25.56	0.081	0.25	0.30	0.27	0.23
Pd	1850	1000	1475	1825	16.28	0.096	0.32	0.27	0.25	0.21
Ag	1200	650	1000	1234	10.78	0.104	0.25	0.27	0.20	0.21
Ir	3400	1750	2740	2683	31.76	0.071	0.36	-	0.24	-
Pt	2450	1300	1925	2042	20.93	0.096	0.32	0.28	0.27	0.21
Au	1400	600	1075	1336	12.38	0.130	0.44	0.25	0.30	0.20
Pb	700	-	575	601	5.93	0.203	vitri.	1.00	0.22	0.37
Ta [b]	3650	-	3150	3253	24.70	0.074	-	0.30	0.15	0.23

The system is subjected to stepped heating and cooling at a rate of 5 K/ps (5×10^{12} K/s). At the end of each heating and cooling step, physical properties such as P, density (or specific volume V) and T are calculated statistically. Thus a plot of density vs. T at constant P can be obtained from NPT runs, from which temperatures at the first-order phase transition (melting and freezing, $T_{1,m}$ and $T_{1,c}$) are readily recognized. Figure 6.5a is a typical example (Al) of the melting-refreezing hysteresis: the system undergoes superheating before melting and undercooling before refreezing. To find the equilibrium melting temperature for the system with the prescribed force fields, we construct a two-phase system with solid and liquid models at a common temperature from single-phase simulations. For the two-phase system, we conduct NPT runs at different temperatures: if $T > T_m$, the system melts and T is reduced, and vice versa. Thus the equilibrium melting temperature of the two-phase system ($T_{2,m}$) is bracketed within a range of 25 K.

From MD simulations, we obtained $T_{1,m}$, $T_{1,c}$ and $T_{2,m}$ at given pressure, thus we can quantify the maximum superheating (Θ^+_{md}) and undercooling (Θ^-_{md}) achieved for a material with the specific force field. Superheating and undercooling achieved at ambient pressure are summarized in Table 6.6. Θ^+_{md} and Θ^-_{md} vary in the range of $0.19-0.30$ and $0.25-0.44$ (except Pb), respectively. These values of Θ^+_{md} and Θ^-_{md} are comparable to the predictions of the superheating-undercooling systematics (Θ^+_{ns} and Θ^-_{ns}) at similar heating (cooling) rate ($Q \sim 10^{12}$ K/s) for the real systems. It is interesting for undercooling of Pb in MD simulations. From Figure 6.5b and radial distribution function calculation, it is clear that Pb liquid becomes vitrified rather than crystallized. This appears to be predicted by the systematics: at cooling rate of $\sim 10^{12}$ K/s [Eq. (6.7) and Figure 6.4], a solid with $\beta > 4.7$ [*e.g.*, $\beta(\mathrm{Pb}) = 5.87$] does not crystallize. High-pressure melting, for example, melting under pressures comparable to shock-wave loading, is of particular interest. Here we explore the pressure effect on superheating and undercooling. Single- and two-phase simulations are conducted on Al at 0, 20, 40, 60, 80 and 100 GPa (Table 6.7). Θ^+_{md} and Θ^-_{md} for $P = 0-100$ GPa lies between $0.19-0.25$ and $0.30-0.48$, respectively. There is no obvious pressure-dependence for superheating and undercooling in the case of Al. This seems to support the weak pressure-dependence of β as argued in preceding section. Previously, two-phase simulation technique has been employed to simulated the superheating behavior of other materials described with different force fields. For example, quantum-mechanics based embedded-atom-method (EAM) force field was applied to Ta (*bcc*) and $\Theta^+_{md} = 0.15$ was obtained [*Stranchan et al.*, 2001] (Table 6.6). Simulations with an EAM force field for ϵ-Fe (*hcp*) yielded $T_{1,m} \sim 8600$ K, $T_{2,m} \sim 7100$ K and $\Theta^+_{md} \sim 0.21$ [*Belonoshko et al.*, 2000], close to the prediction $\Theta^+_{ns} = 0.23$ if $\beta = 3.11$ is assumed. For silica's high-pressure phase, stishovite with Morse-stretch-charge-equilibrium FF, $\Theta^+_{md} = 0.28$ was achieved at 120 GPa [*Luo et al.*, 2002c].

The above comparison between MD simulations and the superheating-undercooling systematics assumed that the force fields utilized in MD simulations accurately describe the real systems, and this is not necessarily the case. The equilibrium melting temperature from MD simulations ($T_{2,m}$) deviates from the experimental counterpart ($T_{e,m}$) at ambient pressure for some metals (Table 6.6). As the only exception, the undercooled Pb liquid does not refreeze in MD simulations while $\Theta^+_{md}(\mathrm{Pb}) = 0.22$ indi-

Table 6.7: Pressure-dependence of superheating and undercooling in MD simulations on Al.

P (GPa)	$T_{1,m}$ (K)	$T_{1,c}$ (K)	$T_{2,m}$ (K)	Θ^+_{md}	Θ^-_{md}
0	1100	650	925	0.19	0.30
20	2400	1150	1925	0.25	0.40
40	3400	1700	2750	0.23	0.38
60	4200	2200	3425	0.23	0.36
80	5000	2800	4125	0.21	0.32
100	5800	3200	4675	0.24	0.32

cates that the liquid should freezes with $\Theta^-_{md} = 0.29$ according to the systematics [Eq. (6.7)]. Such discrepancies imply that the force fields we employed do not necessarily represent all the behavior of real systems.

To check whether MD simulations are consistent with the superheating-undercooling systematics, it is not appropriate to compare MD simulations directly with real systems, although they are certainly in reasonable accord. It is not our purpose in this work to develop force field and check its accuracy, instead, we regard the systems investigated as self-consistent and examine MD simulation's consistency with the superheating-undercooling systematics. To serve this purpose, it would be ideal if γ_{sl} were calculated from MD simulations. In that case, β for a specific system under certain P and T conditions can be obtained directly as ΔH_m and T_m can be readily calculated from MD, and superheating and undercooling achieved in MD can be compared directly with the systematics. As $\gamma_{sl} \sim 0.01 - 0.1$ J/m^2 in order of magnitude, the contribution from solid-liquid interfaces to the total energy of the system, is negligible. Thus current two-phase technique is not appropriate for simulating γ_{sl} and its calculation is left open. An alternative way to check the consistency is to take advantage of both Θ^+_{md} an Θ^-_{md}. Suppose that the maximum undercooling (or superheating) can be described by the systematics [Eq. (6.7)]. Given Θ^-_{md} (or Θ^+_{md}), material property β of a system with prescribed force field can be obtained from the systematics. If β is obtained from Θ^-_{md} (Figure 6.6), the predicted superheating (Θ^+_{ns}) at comparable heating rate $Q \sim 10^{12}$ K/s, can be checked against simulation results. Both Θ^-_{md} and Θ^+_{md} along with β (from Θ^-_{md}) are fitted to the same functional form as the systematics, and we find the excellent agreement between the fitting (dashed curve) and the systematics (Figure 6.6). Note that results at both ambient pressure and high pressures for Al are included in Figure 6.6. Thus, both superheating and undercooling achieved in MD simulations with prescribed force fields are self-consistent with regard to the superheating-undercooling systematics developed from undercooling experiments. The abnormal behavior of undercooled Pb is the only exception which does not comply with the systematics, possibly due to an ill-posed force field, or other causes to be investigated.

We have demonstrated the excellent agreement between MD simulations and the superheating-undercooling systematics. A direct application is to predict the interfacial energy γ_{sl}. Heat of fusion (ΔH_m) can be obtained from the enthalpy (H) difference between solid and liquid from single-phase simulations, T_m from two-phase simulations and β from either Θ^+_{md} or Θ^-_{md}, thus γ_{sl} can be derived (Table 6.6).

6.4 Superheating in ultrafast dynamic experiments

While there is a vast amount of undercooling data in literature, experiments with appreciable superheating are scanty. This is especially true for conventional heating experiments with $Q \sim 1$ K/s, where heterogeneous nucleation is dominant due to the effect of free surfaces and defects such as grain boundaries. In shock-wave loading such as planar impact experiments, the shock-wave front thickness is of nanosecond order, temperature increase during shock of 10^3 K order, and $Q \sim 10^{12}$ K/s. Solid is heated inside as shock front advances and surface melting is suppressed. The long-range order of shocked solid can persist as temperature rises faster than the rearrangement of atoms for melting. The kinetics inherent in solid-liquid transition may play an important role at the time scale of shock-wave front, thus induce superheating.

Figure 6.7 is a schematic showing the two distinct types of melting behavior upon shock-wave loading: equilibrium and non-equilibrium melting. The $T-P$ Hugoniot may follow the equilibrium path, *abcd* where *bc* coincides with melting curve, *i.e.*, shocked solid melts along the equilibrium phase boundary. If Hugoniot follows $abc'cd$,

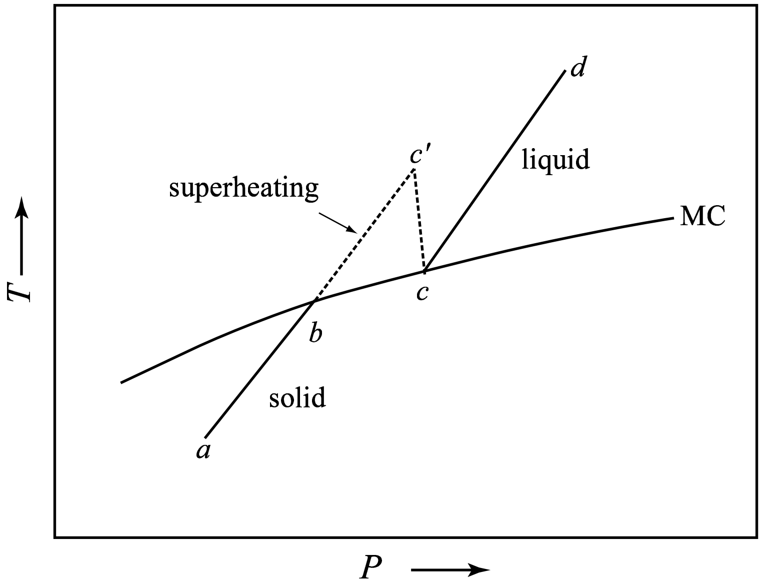

Figure 6.7: Schematic of equilibrium and non-equilibrium melting upon shock-wave loading. MC is the equilibrium melting curve and assumed to have positive dT_m/dP slope. The $T-P$ Hugoniot may follow the equilibrium path, *abcd* where *bc* coincides with MC, *i.e.*, shocked solid melts along the equilibrium phase boundary. If Hugoniot follows $abc'cd$, shocked solid is superheated metastably to a maximum T (c') then melts. Superheating on Hugoniot, $\Theta_H^+ = T_{c'}/T_c - 1$.

shocked solid is superheated metastably to a maximum T (solid Hugoniot ends at c') then melts. The onset of liquid Hugoniot is ideally located on the equilibrium melting curve. Thus, the amount of superheating near the transition pressure P_c on Hugoniot, $\Theta_H^+ = T_{c'}/T_c - 1$. The reason for the preconception of equilibrium melting is 2-fold: equilibrium thermodynamics is chosen for convenience, and more importantly, the pioneering shock temperature measurements on NaCl [*Kormer*, 1965] demonstrate a two-point plateau between 50−60 GPa (Figure 6.8), thus appear to lend experimental support to the equilibrium interpretation. As shown in the following analysis of static and dynamic melting experiments, superheating-melting upon shock loading seems to be a dominant feature in shock melting experiments.

Major techniques employed to detect shock melting are sound-speed and temperature measurements at shock state. Sound speed at shock states drops from longitudinal to bulk sound speed due to the loss of rigidity when solid melts. Similarly,

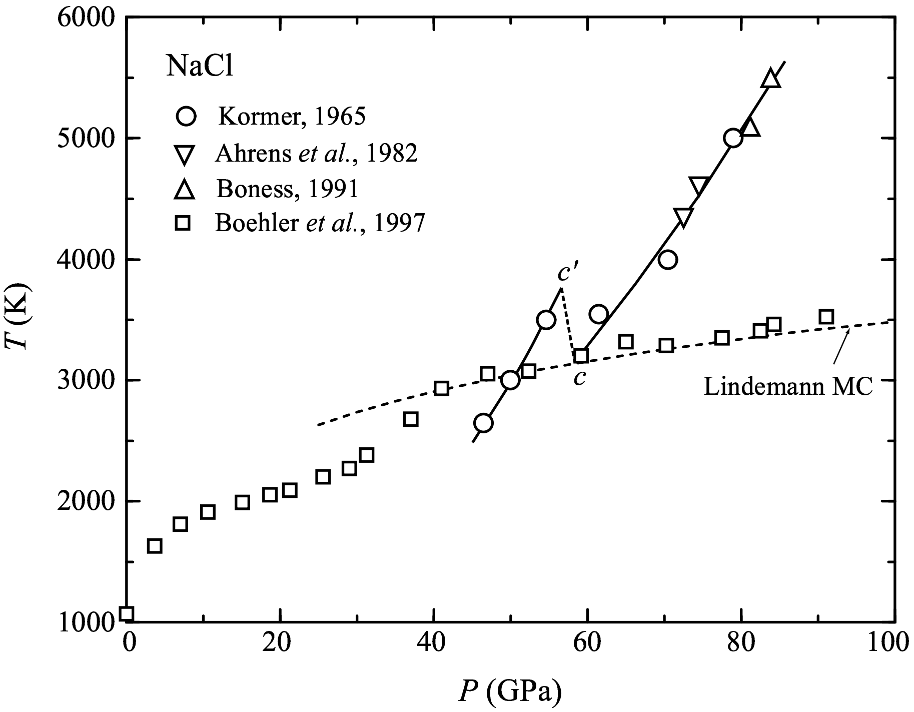

Figure 6.8: Shock temperature [*Kormer*, 1965; *Ahrens et al.*, 1982; *Boness*, 1991] and DAC melting point measurements on NaCl [*Boehler et al.*, 1997b].

shock temperature drops as solid melts due to latent heat. Other techniques such as transient electron diffraction are important diagnostics to detect melting from the loss of long-range order of shocked crystal. Melting might not be recognizable in pressure-density Hugoniot as density change due to melting at high pressures, may be small. Changes in the slope of shock velocity−particle velocity relationship may serve as a complement to other techniques. Temperature and crystal structure measurements are most decisive, while data in the structure measurement are scanty due to technical challenges.

Shock melting experiment have been conducted on alkali halides (NaCl, CsBr and KBr), silicates (fused quartz, quartz and forsterite), and transition metals (Fe, V, Mo, Ta). Alkali halides are advantageous in the studying melting behavior for its optical transparency and relatively low melting temperatures upon shock-wave loading. Thus the $P-T$ conditions are accessible for DAC study. Simultaneous measurement of sound speed and temperature on CsBr and KBr [*Boness and Brown*, 1993] are shown in Figures 6.9-6.10. Simultaneous drop in sound speed and temperature at ∼38 GPa (CsBr) and ∼29 GPa (KBr) signals melting. The amount of superheating is estimated to be 0.16 and 0.20 for CsBr and KBr, respectively. If we assume the energy barrier β of the high-pressure B2 phases of CsBr and KBr to be the ambient values, the superheating systematics predict superheating (Θ^+_{ns}) of 0.20 and 0.18, respectively, with $Q = 10^{12}$ K/s (Table 6.8). (P_c, T_c) is assumed to locate on the equilibrium melting curve, and it coincides with the DAC results [*Boehler et al.*, 1997a] for KBr. We also construct Lindemann melting curve (discussed in next section) integrated from (P_c, T_c). The static data agree almost exactly with the Lindemann curve. For NaCl, we interpret the shock-wave data [*Kormer*, 1965] as non-equilibrium melting (Figure 5), and the estimated superheating agrees with the superheating systematics. The constructed Lindemann curve also agrees exactly with DAC results. Thus, by considering superheating, we resolved one point (P_c, T_c) on the melting curve.

Similar features have been observed in sound speed and/or temperature measurement on fused quartz, quartz [*Lyzenga et al.*, 1983; *McQueen*, 1992] (Figure 6.11a and 6.12), forsterite [*Holland and Ahrens*, 1997] (Figure 6.11b), Fe [*Brown and McQueen*, 1982; *Williams et al.*, 1987; *Yoo et al.*, 1993] (Figure 6.13), V [*Dai et al.*, 2001] (Figure 6.14), Mo [*Hixson et al.*, 1989] (Figure 6.15) and Ta [*Shaner et al.*, 1984] (Figure 6.16). If available, the superheating achieved is compared to the predictions of the superheating systematics (Table 6.8). The superheating of forsterite achieved is estimated to be 0.63 much higher than any material predicted from the superheating systematics. This could be due to complicated chemistry including phase changes and decomposition.

Intense laser irradiation experiments have been conducted on Al [*Williamson et al.*, 1984], Pb(111) [*Herman and Elsayed-Ali*, 1992], Bi(1000) [*Murphy et al.*, 1993] and GaAs [*Fabricius et al.*, 1986], and significant amount of superheating comparable to the predictions of the superheating systematics has been observed (Table 6.8).

The shock melting experiments demonstrate a common feature of superheating with sharp drops in temperature, a behavior deviating from equilibrium melting. The amount of superheating is comparable to the superheating systematics if we

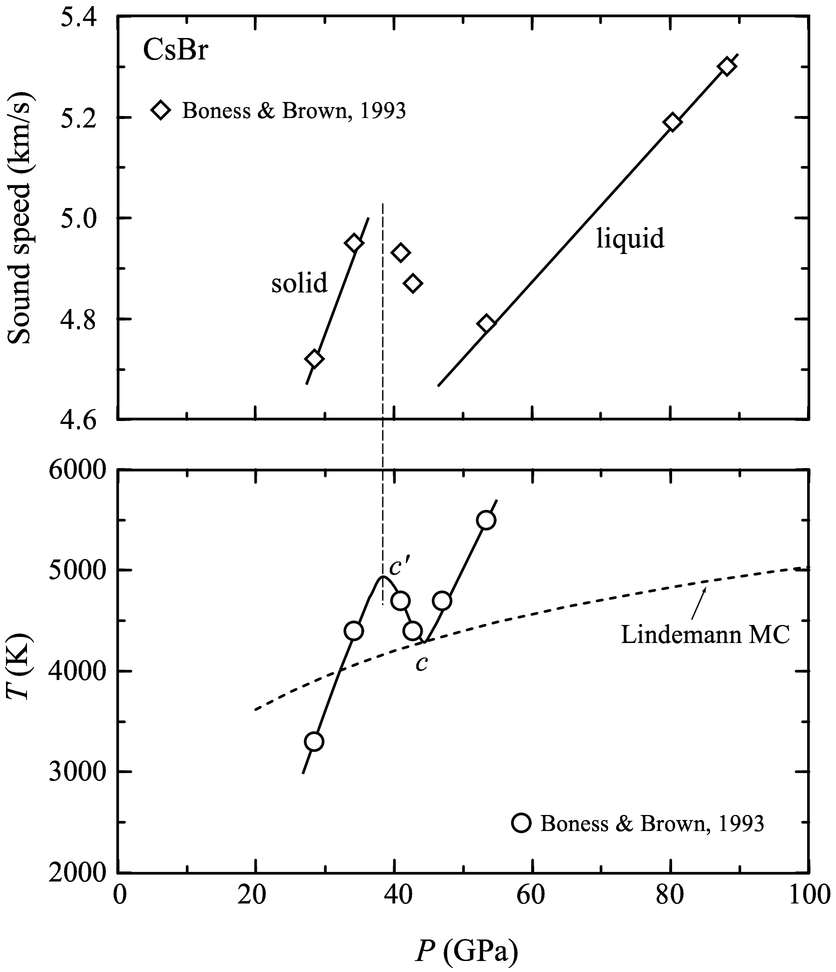

Figure 6.9: Shock-state sound speed and temperature measurements on CsBr [*Boness and Brown*, 1993]. Solid curves are guides for the eye. The thin dashed line denotes the onset of melting.

locate (P_c, T_c) on the equilibrium melting curve. Thus, such an interpretation of shock melting experiments is reasonable, and an important point on the high-pressure melting curve, (P_c, T_c) can be resolved.

Heating rates are comparable to 10^{12} K/s in intense laser irradiation, depending on energy deposited, irradiation time and material properties. In laser irradiation experiments, real-time crystal structure information can be obtained from transient electron diffraction, and temperature from calibration, mass spectometry or inferred. Significant superheating has been observed [*Williamson et al.*, 1984; *Herman and Elsayed-Ali*, 1992; *Murphy et al.*, 1993; *Fabricius et al.*, 1986] in laser irradiated Al,

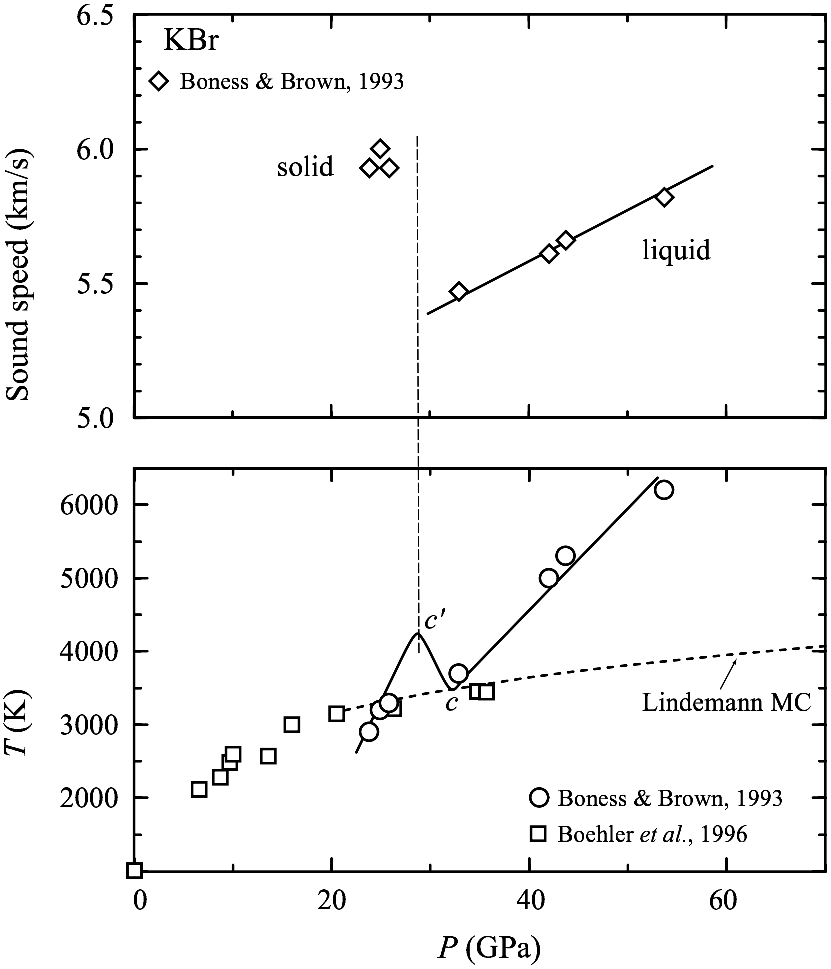

Figure 6.10: Shock-state sound speed and temperature [*Boness and Brown*, 1993], and DAC melting point measurements [*Boehler et al.*, 1997a] on KBr. Solid curves are guides for the eye. The thin dashed line denotes the onset of melting.

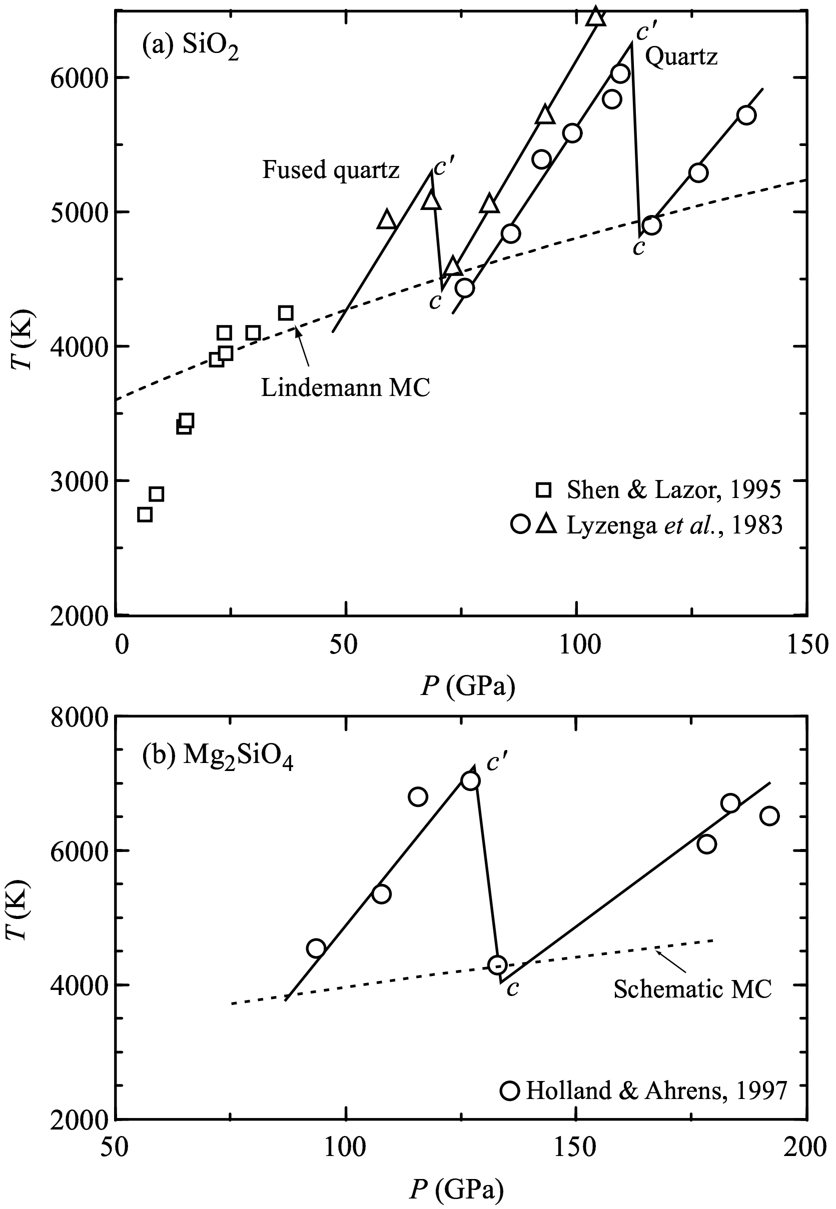

Figure 6.11: Shock temperature measurement on fused quartz and quartz (a, *Lyzenga et al.* [1983]) and forsterite (b, *Holland and Ahrens* [1997]). The DAC measurement on silica melting curve is also shown in (a). The silica Lindemann MC plotted is from shocked fused quartz, and that from shocked quartz is about 150 K lower.

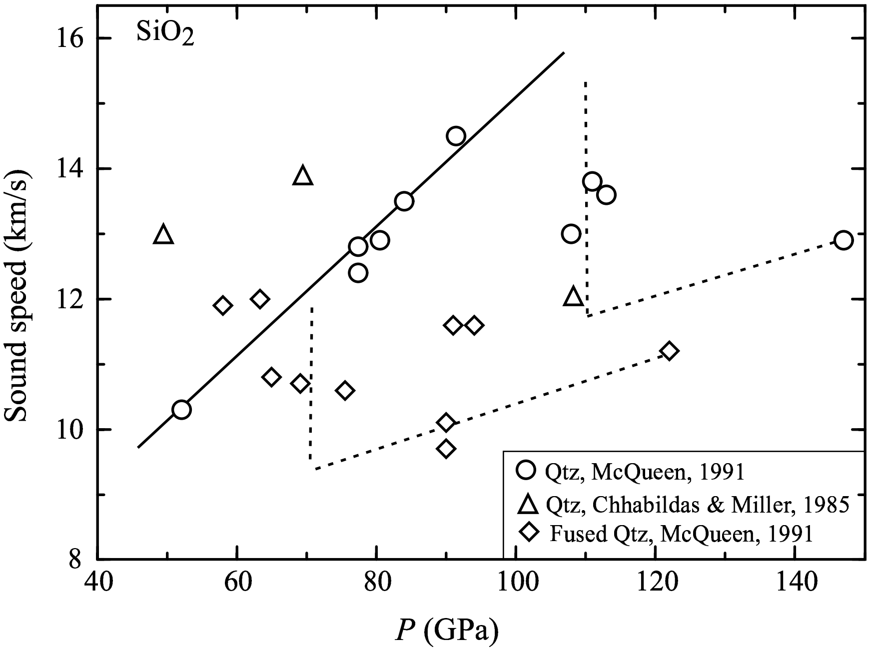

Figure 6.12: Sound speed measurement on shocked fused quartz and quartz [*McQueen*, 1992; *Chhabildas and Miller*, 1985]. Lines are for guide of eye. The vertical dotted lines at ∼ 70 and 110 GPa indicate shock melting [*McQueen*, 1992].

Pb(111), Bi(0001) and GaAs (Table 6.8).

Superheating-melting behavior appears to be the dominant feature in shock melting experiments (including laser irradiation). We compare the observed superheating to the prediction of the superheating systematics at $Q \sim 10^{12}$ K/s, and the agreement is significant (Table 6.8). We assumed that β remains the same at high pressures (thus solid-solid phase changes or chemical decomposition may occur) for planar impact experiments. Shock loading on Mg_2SiO_4 demonstrates unusual superheating [*Holland and Ahrens*, 1997] larger than the prediction for Ga (0.43) at similar heating rate. The result could have been complicated by phase change and decomposition at high pressures. Pressure was assumed to be 0 in laser irradiation experiments. Uncertainties in determining temperature could also contribute to the estimation of superheating. Despite of these uncertainties, it is clear that solids can be superheated substantially beyond the equilibrium melting point by ultrafast heating, and the amount of superheating is comparable to the superheating systematics. The significance of heating

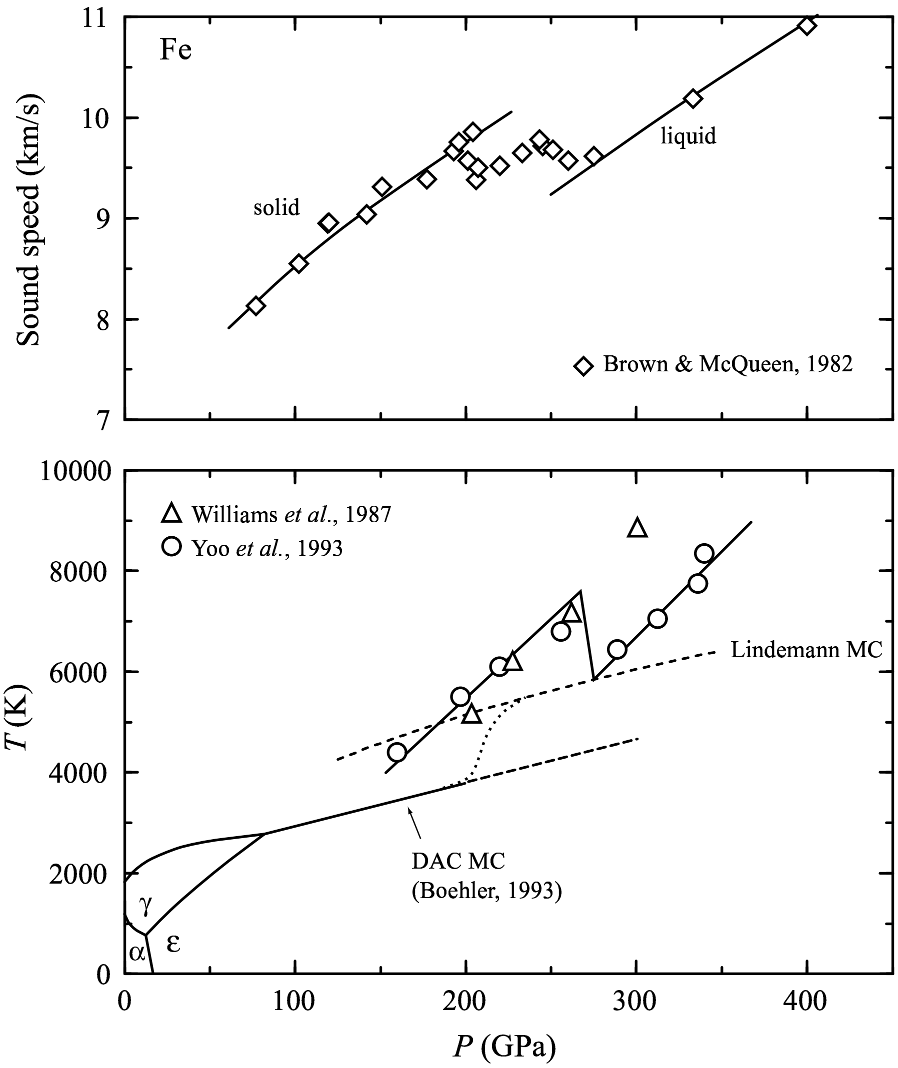

Figure 6.13: Shock-state sound speed [*Brown and McQueen*, 1982] and temperature [*Yoo et al.*, 1993; *Williams et al.*, 1987], and DAC melting point measurements on Fe [*Boehler*, 1993]. The dotted curve is the speculated melting curve connecting $\epsilon-$iron and the possible unknown new phase.

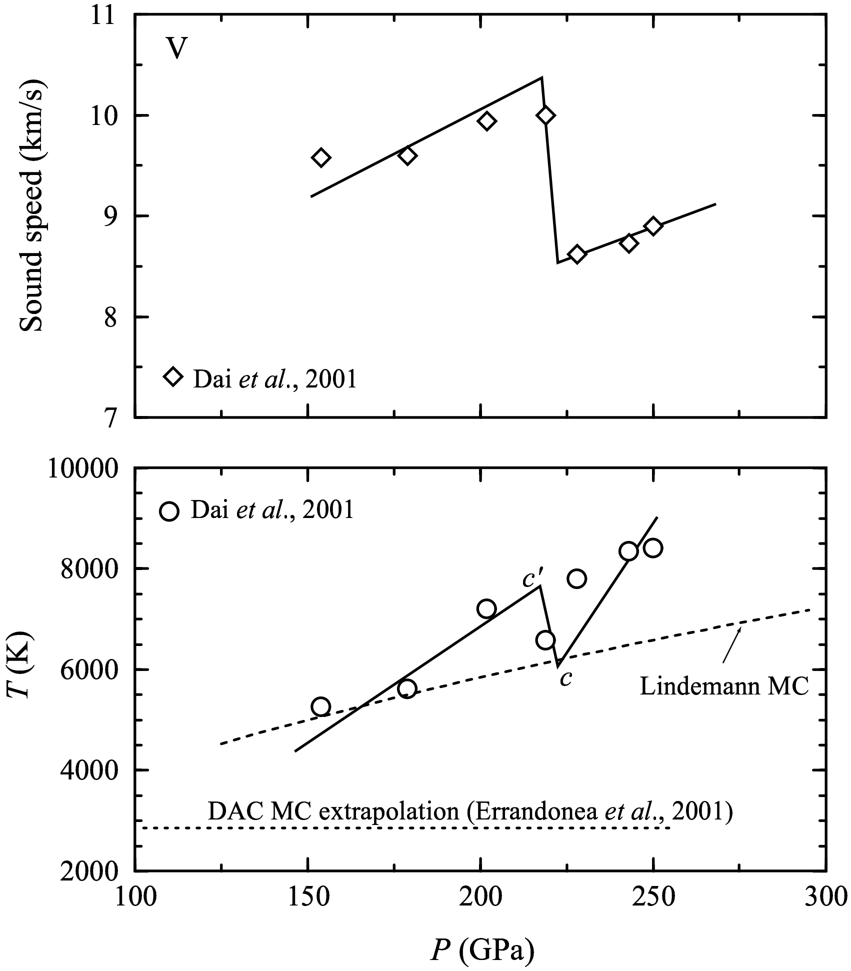

Figure 6.14: Shock-state sound speed and temperature measurements on V [*Dai et al.*, 2001].

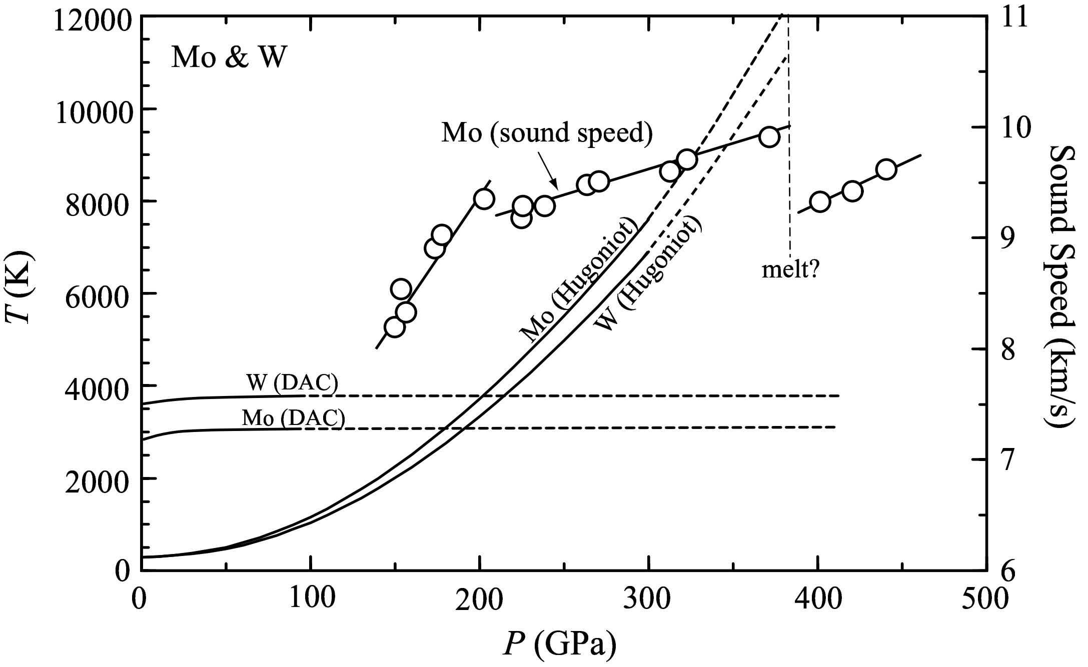

Figure 6.15: Shock-state sound speed measurement on Mo [*Hixson et al.*, 1989] and calculated $P-T$ Hugoniots for Mo and W [*Hixson and Fritz*, 1992]. DAC melting curves of Mo and W [*Errandonea et al.*, 2001] are extrapolated to higher pressures.

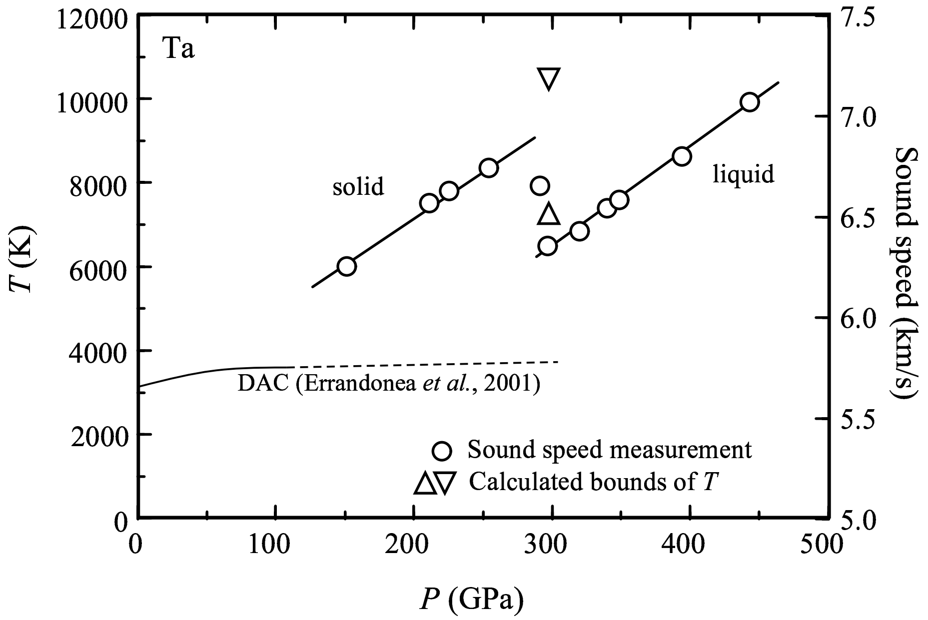

Figure 6.16: Shock-state sound speed measurement on Ta, and upper and lower bound of calculated shock temperature [*Shaner et al.*, 1984]. DAC melting curves of Ta [*Errandonea et al.*, 2001] are extrapolated to higher pressures.

Table 6.8: Superheating achieved in ultrafast dynamic experiments: planar shock-wave loading and intense laser irradiation. Note that materials may be subjected to phase changes and decomposition at high pressures.

Starting Material	P_c (GPa)	T_c (K)	$T_{c'}$ [a] (K)	Θ_H^+	Θ_{ns}^+
Planar Impact					
Fe	270	5800	7250	0.25	0.28
V	220	6150	7600	0.24	0.23
CsBr [b]	38	4150	4950	0.19	0.20
KBr [b]	28	3500	4200	0.20	0.18
Fused quartz	70	4500	5300	0.18	-
Quartz	113	4800	6100	0.27	0.34 [c]
Mg_2SiO_4	130	4300	7000	0.63	-
Laser irradiation					
Al	0	933	1300 [d]	0.39	0.20
Bi(0001)	0	544	634	0.17	0.37
Pb(111)	0	601	721	0.20	0.37
GaAs	0	1511	2061	0.36	-

---

[a] Estimated from $T - P$ Hugoniot.

[b] P at c' and T at $P_{c'}$ on the Lindemann MC are adopted.

[c] Value for quartz at ambient pressure.

[d] Value for irradiation flux of 7 mJ/cm^2 is adopted.

rates lies in that ultrafast heating is crucial to achieving superheating.

The high-pressure melting behavior of transition metals have been investigated systematically [*Errandonea et al.*, 2001] with laser-heated diamond-anvil cell techniques. The slope of melting curve dT_m/dP for transition metals become nearly zero at ∼100 GPa. If such behavior were valid at shock pressures $(200 - 400$ GPa) for metals such as Fe, V, Ta, W and Mo, the induced superheating $(\Theta_H^+ \sim 0.7 - 2.0)$ in shock-wave loading [*Yoo et al.*, 1993; *Dai et al.*, 2001; *Shaner et al.*, 1984; *Hixson et al.*, 1989; *Hixson and Fritz*, 1992] would be far beyond the predictions of superheating systematics even when uncertainties are taken into account. This is unlikely thus caution should be imposed as we extrapolate low pressure static data to high pressures.

6.5 Applications to high-pressure melting

In the preceding discussion, we have observed that significant amount of superheating has been achieved in ultrafast shock-wave loading on metals, alkali halides and silicates. With superheating systematics, shock melting experiments resolve one important point, (P_c, T_c), on the high-pressure melting curve (figure 6.7). Next we deduce other important thermodynamic parameters of melting, such as melting curve, changes in entropy and volume upon melting at high pressures. In the absence of first-principles theories, the Lindemann law and the $ln2$ rule (systematics of entropy of melting) are adopted.

6.5.1 The $ln2$ rule for entropy of melting

First we briefly examine the validity of the $ln2$ rule. Previously, efforts have been made to establish the systematics of entropy of melting [*Oriani*, 1951; *Stishov*, 1975; *Tallon and Robinson*, 1982; *Poirier*, 1991]. The entropy of melting per mole atoms,

ΔS_m, can be written as

$$\Delta S_m = \Delta S_D + \Delta S_V \tag{6.11}$$

where ΔS_V is the entropy of fusion associated with volume and vibrational changes, and ΔS_D the entropy of disorder [*Oriani*, 1951]. Later, a $ln2$ rule was proposed [*Stishov*, 1975; *Tallon and Robinson*, 1982] for simple atomic and some binary and ternary substances, as

$$\Delta S_m = Rln2 + \alpha K \Delta V_m \tag{6.12}$$

where R is the gas constant, α thermal expansivity of volume, K bulk modulus, and ΔV_m volume change upon melting. Comparing Eqs. 11 and 12 yields that ΔS_D is essentially $Rln2$, although Oriani tried different way to quantify disordering upon melting [*Oriani*, 1951]. The $ln2$ rule was justified for simple atomic system with a simple cell model [*Stishov*, 1975] and by calculating topological entropy [*Rivier and Duffy*, 1982].

The $ln2$ rule has been checked against limited data and the universality is not well justified. We take the entropies for elements (Table 6.9) [*Oriani*, 1951] and plot ΔS_m *vs.* ΔS_V. As shown in Figure 14, the $ln2$ rule applies as expected. Note that there are exceptions, *e.g.*, Ga (not plotted). The behavior of silicates is of particular interest. For the five silicates investigated (Table 6.10) [*Poirier*, 1991], the data points of forsterite, fayalite, pyrope and enstatite cluster around the $ln2$ line, except quartz for which ΔS_D is essentially 0 (Figure 14). Appreciable amount of data for alkali halides was documented (Table 6.11) [*Jackson*, 1977] which allow us to examine the behavior of alkali halides. KX (X = F, Cl, Br and I) agrees with the $ln2$ rule, while LiX has 0 or negative ΔS_D. The values of ΔS_D for NaX lie between $ln2$ and 0 line (Figure 14). It is not surprising if we consider the possible large differences in

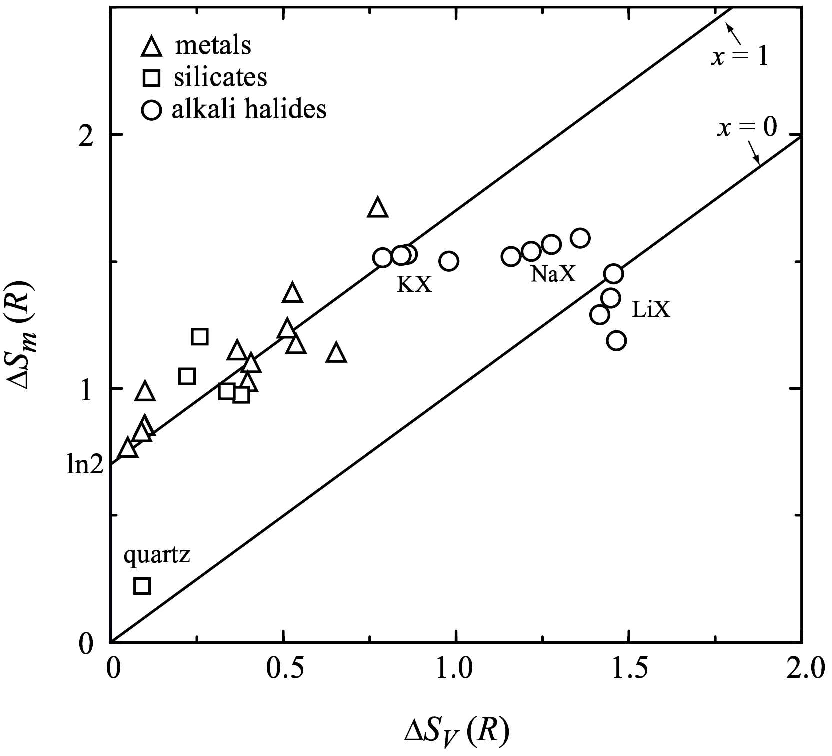

Figure 6.17: The $ln2$ rule of entropy of melting: ΔS_m *vs.* ΔS_V for metals, silicates and alkali halides. Refer to Table 6.9-6.11. Solid lines have slopes of 1 and intercepts of $Rln2$ ($x = 1$) and 0 ($x = 0$) respectively. X denotes F, Cl, Br and I.

disordering upon melting. Instead of a strict $ln2$ rule, we propose that

$$\Delta S_m = xRln2 + \alpha K \Delta V_m \tag{6.13}$$

where $0 \leq x \leq 1$, although by eliminating large uncertainties in calculating ΔS_V (*e.g.*, NaX), data points could cluster near the $x = 1$ and $x = 0$ lines. The structure-dependence of x, should be investigated in a fundamental way and is an important issue to be resolved.

For the materials investigated in shock melting experiments (essentially, melting of high-pressure phases of Fe, V, KBr, CsBr, NaCl and silica), we suppose that $ln2$ rule applies ($x = 1$) as there is no apparent contradiction.

Table 6.9: The $ln2$ rule for melting entropies of metals. Values of entropy are from *Oriani* [1951] and normalized by R.

	Ag	Al	Au	Cu	Pb	Li	Na	K	Cs	Fe	Cd	Mg	Sn
$\Delta S_m(R)$	1.102	1.378	1.142	1.152	1.026	0.770	0.855	0.855	0.830	0.991	1.237	1.177	1.715
$\Delta S_V(R)$	0.407	0.528	0.654	0.367	0.397	0.050	0.100	0.099	0.091	0.100	0.513	0.538	0.774
$\Delta S_D(R)$	0.695	0.850	0.488	0.785	0.629	0.720	0.755	0.756	0.739	0.891	0.724	0.639	0.941

Table 6.10: The $ln2$ rule for melting entropy per mole atoms of silicates.

Silicate	n	ΔV_m^a (cm^3/g)	$\Delta V_m/V^a$	α^b (10^{-6} K^{-1})	K^c (GPa)	ΔS_m (R)	ΔS_V (R)	ΔS_D (R)
Quartz (SiO_2)	3	2.50	0.105	24.3	37.8	0.221	0.092	0.129
Forsterite (Mg_2SiO_4)	7	3.80	0.081	30.6	129.5	1.203	0.259	0.944
Fayalite (Fe_2SiO_4)	7	3.70	0.076	26.1	134.0	1.047	0.222	0.825
Pyrope ($Mg_3Al_2Si_3O_{12}$)	20	18.3	0.158	19.9	172.8	0.975	0.378	0.597
Enstatite ($MgSiO_3$)	5	5.40	0.160	24.1	107.8	0.989	0.337	0.652

---

[a] *Poirier* [1991].
[b] *Fei* [1995].
[c] *Bass* [1995].

Table 6.11: The $ln2$ rule for melting entropy of alkali halides. Heat capacity and entropy refer to per mole atoms.

	γ_0^a	ΔV_m^a (cm^3/g)	$\Delta V_m/V$	C_v^b (R)	ΔS_m^a (R)	ΔS_V (R)	ΔS_D (R)
LiF	1.63	3.47	0.356	2.52	1.451	1.458	-0.007
LiCl	1.81	5.63	0.277	2.89	1.356	1.449	-0.093
LiBr	1.94	6.22	0.248	2.94	1.290	1.417	-0.127
LiI	2.19	7.22	0.222	3.01	1.187	1.465	-0.278
NaF	1.51	4.75	0.320	2.82	1.592	1.361	0.231
NaCl	1.62	7.01	0.259	3.04	1.567	1.277	0.290
NaBr	1.65	7.67	0.239	3.09	1.539	1.220	0.319
NaI	1.71	8.82	0.216	3.14	1.519	1.161	0.358
KF	1.52	5.04	0.219	2.95	1.501	0.981	0.520
KCl	1.49	7.02	0.187	3.09	1.529	0.860	0.669
KBr	1.50	7.72	0.178	3.15	1.524	0.843	0.681
KI	1.49	8.86	0.167	3.18	1.514	0.789	0.725

---

[a] See *Jackson* [1977] and references therein.

[b] JANAF [*Malcolm*, 1998].

6.5.2 High-pressure melting parameters based on the Lindemann law and $ln2$ rule

Now we deduce the parameters of high-pressure melting which are implied by the previously discussed shock temperature, and sound speed data for elements, alkali halides and minerals.

Alternatively, Eq. 6.13 can be written as

$$\Delta S_m = Rln2 + \gamma C_V \frac{\Delta V_m}{V} \tag{6.14}$$

where γ is the Grüneisen parameter and C_V the specific heat per mole atom. Both Eqs. 12 and 14 will be used for evaluating ΔS_m with either γC_V or αK. ΔS_m is related to ΔV_m via the Clausius-Clapeyron equation

$$\Delta V_m = \frac{dT_m}{dP} \Delta S_m \tag{6.15}$$

The slope dT_m/dP along melting curve can be calculated using the Lindemann law [*Stacey and Irvine*, 1977]

$$\frac{dlnT_m}{dP} = \frac{2\gamma}{K} \tag{6.16}$$

Since in most of the materials of interest (Table 6.12), melting of a high-pressure phase occurs, we require the Grüneisen parameter and equation of state (EOS) of the high-pressure phase. We thus employ in most cases the bulk modulus that is derived from the principal Hugoniot centered at the zero-pressure density of the metastable high-pressure phase, and assume Murnaghan EOS [*Poirier*, 1991]. A shock-wave EOS, can be described by a linear shock velocity (U_S) - particle velocity (u_p) relation

$$U_S = C_0 + s u_p \tag{6.17}$$

where C_0 and s are parameters. The bulk modulus $K_0 = \rho_0 C_0^2$, and its pressure derivative, $K_0^{'} = 4s - 1$. Subscript 0 denotes ambient pressure. The Grüneisen parameter, γ, is assumed to be volume dependent only

$$\gamma(V) = \gamma_0(\frac{V}{V_0})^q \tag{6.18}$$

where $\gamma_0 = (162s^2 - 360s + 215)/18s$ [*Jeanloz and Grover*, 1987]. Given a reference state (P_c, T_c) resolved from shock melting experiments (Table 6.12), the melting curve can be calculated by integrating Clausius-Clapeyron equation. The Lindemann melting curves are plotted in Figures 6.8-6.13. ΔS_m and ΔV_m at certain pressure, *e.g.*, P_c can be readily calculated as shown in Table 6.12.

The Lindemann melting curves constructed via the above procedures demonstrate self-consistency and good agreement with DAC experiments with laser-heating techniques. The two Lindemann curves for stishovite obtained from fused and crystal quartz agree closely within 150 K. The Lindemann curve from fused quartz also agrees with the DAC data [*Shen and Lazor*, 1995] at $25 - 40$ GPa. There is excellent agreement between DAC experiments [*Boehler et al.*, 1997a, b] and Lindemann curves from shock-wave results for KBr and NaCl. Other tests of shock-induced melting data for porous metals and minerals should be conducted when there are sufficient data.

The above comparison illustrates the encouraging convergence between static and dynamic data. We must be aware of the fact that significant discrepancies exist for transition metals. A factor could alleviate the discrepancy: shock melting pressures are significantly higher than those achieved by conventional DAC-melting experiments, thus a comparison requires large extrapolation of the DAC melting curve to higher pressures. In other words, extrapolation could be problematic as phase changes could occur at higher pressures beyond DAC's reach. This could be especially true for Fe: although controversial, a possible phase chance near 200 GPa [*Brown*, 2001] could steepen the melting curve, thus bring the convergence of static and dynamic experiments. The bottom line is that given the uncertainties in shock temperature measurements and β variations at high pressures, an incautious extrapolation of DAC melting curve appears to be incompatible with superheating systematics, as transition metals cannot be superheated by $0.7-2.0T_m$ (Figures 6.13-6.16).

6.6 Concluding remarks

Catastrophic nucleation near the maximum superheating and undercooling (θ_c) dominates nucleation process. Such a catastrophe is free-energy-based and we can regard it as a kinetic limit. Previous efforts in MD simulations attempted to relate thermodynamic superheating to Lindemann's criterion and Born (shear) instability [*Phillpot et al.*, 1989; *Jin et al.*, 2001; *Wang et al.*, 1997]. In MD simulations of a Lennard-Jones fcc system, superheating of $\Theta^+_{md} \sim 0.20$ corresponds to Lindemann's parameter $\delta_L \sim 0.22$ (fractional root-mean-square displacement) and near zero shear moduli of bulk system [*Jin et al.*, 2001]. It is not surprising that both criteria are satisfied at the kinetic limit. We have validated the systematics of kinetic limit for melting and freezing at atomic level. But a universal relationship between kinetic limit, Lindemann's criterion and Born instability, needs to be established and quantified from first principles.

The maximum superheating and undercooling (θ_c), depend on material property β inherently and heating (or cooling) process (*i.e.*, Q) externally. The $\theta_c-\beta-Q$ systematics for maximum superheating and undercooling are established as $\theta_c=(A_0-blogQ)\theta_c(1-\theta_c)^2$, based on classical nucleation theory and undercooling experiments. Such systematics are validated at the level of interatomic interactions with systematic molecular dynamics simulations on superheating and undercooling. Heating rate is crucial to achieving appreciable superheating experimentally. We demonstrate that superheating achieved in ultrafast dynamic experiments such as planar shock-wave loading and intense laser irradiation, agrees the predictions of the $\theta_c-\beta-Q$ systematics.

We examined the shock superheating-melting data on silicates, alkali halides and metals against the superheating systematics, and validate the method of resolving equilibrium melting point (P_c, T_c) on Hugoniots. The agreement between shock-induced superheating and the superheating systematics indicates that the assumption

Table 6.12: Superheating achieved in shock-wave loading, and the deduced melting parameters based on the Lindemann law and $ln2$ rule for entropy of melting.

Starting Phase	Ending Phase	Superheating Θ_H^+	Θ_{ns}^+	T_c (K)	P_c (GPa)	ρ_0 (g/cm^3)	s[a]	C_0[a] (km/s)	γ_0[a]	q[b]	dT_m/dP (K/GPa)	$\Delta V/V$ (%)	ΔS (R)
NaCl (B1)	B2	0.20	0.18	3125	57.8	2.232	1.22	3.62	0.77	1.0	10.88	0.85	0.704
KBr (B1)	B2	0.20	0.18	3500	33.0	3.071	1.20	3.14	0.75	1.0	21.92	1.02	0.708
CsBr (B2)	B2	0.16	0.20	4260	43.0	4.440	1.25	2.25	0.81	1.0	22.09	0.91	0.705
SiO_2 (fused)	rutile	0.17	-	4500	70.0	4.310	1.08[c]	12.25[c]	1.35[d]	2.6[d]	10.87	1.58	0.744
SiO_2 (quartz)	rutile	0.30	-	4800	113.0	4.310	1.24[c]	9.66[c]	1.35[d]	2.6[d]	9.33	1.47	0.730
Fe (*bcc*)	unkown	0.25	0.23	5800	270.0	8.280[e]	1.47[e]	4.64[e]	1.70[f]	1.0[f]	8.53	1.19	0.732
V (*bcc*)	unkown	0.24	0.26	6150	220.0	6.110	1.23[g]	5.06[g]	2.00[h]	1.0	14.98	1.83	0.761

---

[a] Obtained from finite strain, linear $U_S - u_p$ relation *Jeanloz and Grover* [1987] unless stated otherwise.

[b] Assumed to be 1 unless stated otherwise.

[c] Metastable Hugoniot centered on the high-pressure phase.

[d] *Luo et al.* [2002d].

[e] *Brown and McQueen* [1982].

[f] *Brown* [2001].

[g] *Gathers et al.* [1983]

[h] *Dai et al.* [2001].

of homogeneous nucleation of melt upon shock-wave loading of single crystals, is viable.

We modified the $ln2$ rule for disordering entropy of melting as $\Delta S_D = xRln2$. $x = 0$ for quartz and lithium halides at ambient pressure. x is taken to be 1 for the high-pressure phases investigated. With (P_c, T_c) resolved from shock-wave experiments, the melting curves at high pressures, entropy and volume changes upon melting were obtained for stishovite, KBr, CsBr, NaCl (B2 phases), Fe and V based on the Lindemann law and $ln2$ rule. The volume change $(\Delta V_m/V)$ upon melting at high pressure, varies between $0.85 - 1.83\%$ for the materials investigated, thus ΔS_m is close to $Rln2$ due to the small changes in volume. For alkali halides and silica, the values for (P_c, T_c) and corresponding Lindemann melting curves, are in excellent agreement with the DAC results. For transition metals, significant discrepancies exist between shock-wave results and the extrapolation of DAC data. Given the uncertainties in shock temperature measurement and pressure-induced changes in β, assuming the extrapolated DAC melting curve predicts superheating of $\Theta_H^+ = 0.7 - 2.0$ for Fe, V, Mo, W and Ta far beyond the predictions of superheating systematics, thus it is not valid to extrapolate DAC results to the pressure range of shock melting for transition metals. Possible high-pressure solid-solid phase change thus a change in slope dT_m/dP could reconcile these discrepancies. For melting of Fe, this work suggests that Fe melts at $\sim$ 270 GPa upon shock melting, and equilibrium T_m is $\sim$6277 K at 330 GPa, and supports the view that a possible solid-solid phase change occurs at $\sim$200 GPa as previously suggested (*e.g.*, *Brown* [2001]).

Acknowledgement: We appreciate helpful discussions with Z. Gong, D. Stevenson, R. Boehler and R. Jeanloz. Molecular dynamics simulations were conducted at Materials and Process Simulation Center, Beckman Institute, Caltech (Goddard). T. J. Ahrens, T. Çağın , A. Strachan, W. A. Goddard III and D. Swift contributed partly to this work.

Bibliography

Ahrens, T. J., G. A. Lyzenga, and A. C. Mitchell, Temperature induced by shock waves in minerals, in *High-Pressure Research in Geophysics, Adv. Earth Planet. Sci. Vol. 12*, edited by S. Akimoto and M. H. Manghnani, pp. 579–594, Center for Academic Publications, Tokyo, 1982.

Akins, J. A., and T. J. Ahrens, Dynamic compression of SiO_2: A new interpretation, *Geophys. Res. Lett.*, *29*, 10.1029/2002GL014,806, 2002.

Allen, M., and D. Tildesley, *Computer Simulation of Liquids*, Clarendon Press, Oxford, 1987.

Al'tshuler, L. V., R. F. Trunin, and G. V. Simakov, Shock wave compression of periclase and quartz and the composition of the Earth's lower mantle, *Izv. Akad. Nauk USSR, Fiz. Zemli*, *10*, 1–6, 1965.

Anderson, O. L., A simplified method for calculating the Debye temperature from elastic constants, *J. Phys. Chem. Solids*, *24*, 909–917, 1963.

Anderson, O. L., *Equation of State of Solids for Geophysics and Ceramic Science*, Oxford Univ. Press, New York and Oxford, 1995.

Andrault, D., G. Fiquet, F. Guyot, and M. Hanfland, Pressure-induced Landau-type transition in stishovite, *Science*, *282*, 720–724, 1998.

Andrault, D., R. J. Angel, J. L. Mosenfelder, and T. L. Bihan, Equation of state of stishovite to lower mantle pressures, *Preprint*, 2002.

Bass, J. D., Elasticity of minerals, glasses and melts, in *Mineral Physics and Crystallography: A Handbook of Physical Constants*, edited by T. J. Ahrens, pp. 45–63, AGU, Washington, D.C., 1995.

Belonoshko, A. B., and L. S. Dubrovinsky, Molecular dynamics of stishovite melting, *Geochim. Cosmochim. Acta*, *59*, 1883–1889, 1995.

Belonoshko, A. B., R. Ahuja, and B. Johansson, Quasi-ab inito molecular dynamics study of Fe melting, *Phys. Rev. Lett.*, *84*, 3638–3641, 2000.

Birch, F., Elasticity and constitution of the Earth's interior, *J. Geophys. Res.*, *57*, 277–286, 1952.

Birch, F., Finite strain isotherm and velocities for single-crystal and polycrystalline NaCl at high pressures and 300 K, *J. Geophys. Res.*, *95*, 1257–1268, 1978.

Boehler, R., Temperatures in the Earth's core from melting-point measurements of iron at high static pressures, *Nature*, *363*, 534–536, 1993.

Boehler, R., M. Ross, and D. B. Boercker, High-pressure melting curve of alkali halides, *Phys. Rev. B*, *53*, 556–573, 1997a.

Boehler, R., M. Ross, and D. B. Boercker, Melting of LiF and NaCl to 1 mbar: Systematics of ionic solids at extreme conditions, *Phys. Rev. Lett.*, *78*, 4589–4592, 1997b.

Boness, D. A., *Shock-wave Experiments and Electronic Band-strusture Calculations of Materials at High Temperature and Pressure*, Ph.D. Thesis, Univ. Washington, 1991.

Boness, D. A., and J. M. Brown, Bulk superheating of solid KBr and CsBr with shock-waves, *Phys. Rev. Lett.*, *71*, 2931–2934, 1993.

Born, M., Thermodynamics of crystal melting, *J. Chem. Phys.*, *7*, 591–603, 1939.

Boslough, M. B., Postshock temperatures in silica, *J. Geophys. Res.*, *93*, 6477–6484, 1988.

Brandon, A. D., M. D. Norman, R. J. Walker, and J. W. Morgan, $^{186}O_s$ - $^{187}O_s$ systematics of Hawaiian picrites, *Earth Planet. Sci. Lett.*, *174*, 25–42, 1999.

Brazhkin, V. V., R. N. Voloshin, and S. V. Popova, The kinetics of the transition of metastable phases of SiO_2, stishovite and coesite to the amorphous state, *J. Non-crystal. Solids*, *136*, 241–248, 1991.

Breger, L., and B. Romanowicz, Three-dimensional structure at the base of the mantle beneath the central Pacific, *Science*, *282*, 718–720, 1998.

Breger, L., B. Romanowicz, and H. Tkalcic, PKP(BC-DF) travel time residuals and short scale heterogeneity in the deep earth, *Geophys. Res. Lett.*, *26*, 3169–3172, 1999.

Breger, L., H. Tkalcic, and B. Romanowicz, The effect of D" on PKP(AB-DF) travel time residuals and possible implications for inner core structure, *Earth Planet. Sci. Lett.*, *175*, 133–143, 2000.

Brown, J. M., The equation of state of iron to 450 GPa: another high pressure solid phase?, *Geophys. Res. Lett.*, *28*, 4339–4342, 2001.

Brown, J. M., and R. G. McQueen, The equation of state for iron and the Earth's core, in *High-Pressure Research in Geophysics, Adv. Earth Planet. Sci. Vol. 12*, edited by S. Akimoto and M. H. Manghnani, pp. 611–623, Center for Academic Publications, Tokyo, 1982.

Brown, J. M., and R. G. McQueen, Phase-transitions, Grüneisen-parameter, and elasticity for shocked iron between 77 GPa and 400 GPa, *J. Geophys. Res.*, *91*, 7485–7494, 1986.

Brown, J. M., and T. J. Shankland, Thermodynamic parameters in the Earth as determined from seismic profiles, *Geophys. J. Roy. Astro. Soc.*, *66*, 579–596, 1981.

Buffett, B. R., R. Jeanloz, and E. Garnero, Sediments at the top of the Earth's core, *Science*, *290*, 1338, 2000.

Chao, E. C. T., J. J. Fahey, J. Littler, and D. Milton, Stishovite, a new mineral from Meteor Crater, *J. Geophys. Res.*, *67*, 419–421, 1962.

Chhabildas, L. C., and D. E. Grady, Dynamic material response of quartz at high strain rates, *Mat. Res. Soc. Symp. Proc.*, *22*, 147–150, 1984.

Chhabildas, L. C., and J. M. Miller, Release-adiabat measurements in crystalline quartz, *Sandia Report*, *SAND85-1092*, 1985.

Choy, G. L., and V. Cormier, The structure of the inner core from short-period and broadband GDSN data, *Geophys. J. R. Astro. Soc.*, *72*, 1–21, 1983.

Choy, G. L., and P. Richards, Pulse distortion and Hilbert transformation by a frequency-dependent full wave theory, and their interpretation, *J. Roy. Astro. Soc.*, *51*, 275–311, 1975.

Christian, J. W., *The Theory of Transformations in Metals and Alloys*, Pergamon Press, 1965.

Cohen, R., O. Gülseren, and R. Hemley, Accuracy of equation-of-state formulations, *Am. Mineral.*, *85*, 338–344, 2000.

Cohen, R. E., First-principle theory of crystalline SiO_2, in *Silica: physical behavior, geochemistry and materials applications, Rev. Mineral. Vol 29*, edited by P. Heaney, C. Prewitt, and G. Gibbs, pp. 369–402, Mineral. Soc. Am., Washington, D.C., 1994.

Cormier, V. F., and G. L. Choy, A search for lateral heterogeneity in the inner core from differential travel times near PKP-D and PKP-C, *Geophys. Res. Lett.*, *13*, 1553–1556, 1986.

Creager, K. C., Anisotropy of the inner core from differential travel times of the phases PKP and PKIKP, *Nature*, *356*, 309–314, 1992.

Cygan, R. T., Molecular modeling in Mineralogy and Geochemistry, in *Rev. Mineral. Geoch. Vol. 42*, edited by R. T. Cygan and J. D. Kubicki, pp. 1–35, Mineral. Soc. Am., Washington, D.C., 2001.

Dai, C., X. Jin, X. Zhou, J. Liu, and J. Hu, Sound velocity variations and melting of vanadium under shock compression, *J. Phys. D: Appl. Phys.*, *34*, 3064–3070, 2001.

Davidchack, R. L., and B. B. Laird, Direct calculation of the hard-sphere crystal/melt interfacial energy, *Phys. Rev. Lett.*, *85*, 4751–4754, 2000.

DeCarli, P., and J. C. Jamieson, Formation of an amorphous form of quartz under shock conditions, *J. Chem. Phys.*, *31*, 1675–1676, 1959.

DeCarli, P. S., and D. J. Milton, Stishovite: Synthesis by shock wave, *Science*, *147*, 144, 1965.

Demiralp, E., T. Cagin, and W. A. Goddard, Morse-Stretch potential charge equilibrium force field for ceramics: application to the quartz-stishovite phase transition and to silica glass, *Phys. Rev. Lett.*, *82*, 1708–1711, 1999.

Dziewonski, A. M., and D. L. Anderson, Preliminary reference Earth model, *Phys. Earth Planet. Int.*, *25*, 297, 1981.

Dziewonski, A. M., and J. H. Woodhouse, Global images of the Earth's interior, *Science*, *236*, 37–48, 1987.

ElGoresy, A., L. Dubrovinsky, T. G. Sharp, S. K. Saxena, and M. Chen, A momoclinic post-stishovite polymorph of silica in the Shergotty Meteorite, *Science*, *288*, 1632–1634, 2000.

Endo, S., T. Akai, Y. Akahama, M. Wakatsuki, T. Nakamura, Y. Tomii, K. Koto, Y. Ito, and M. Tokonami, High temperature X-ray study of single crystal stishovite synthesized with Li_2WO_4 as flux, *Phys. Chem. Minerals*, *13*, 146–151, 1986.

Errandonea, D., B. Schwager, R. Ditz, C. Gessmann, R. Boehler, and M. Ross, Systematics of transition-metal melting, *Phys. Rev. B*, *63*, 132,104, 2001.

Fabricius, N., P. Hermes, D. von der Linde, A. Pospieszczyk, and B. Stritzker, Observation of superheating during laser melting, *Solid State Comm.*, *58*, 239–242, 1986.

Fecht, H. J., and W. L. Johnson, Entropy and enthalpy catastrophe as a stability limit for crystalline material, *Nature*, *334*, 50–51, 1983.

Fei, Y., Thermal expansion, in *Mineral Physics and Crystallography, A Handbook of Physical Constants*, edited by T. J. Ahrens, pp. 29–44, AGU, Washington, D.C., 1995.

Fei, Y., S. K. Saxena, and A. Navrotsky, Internally consistent thermodynamic data and equilibrium phase relations for compounds in the system MgO-SiO_2 at high pressure and high temperature, *J. Geophys. Res.*, *95*, 6915–6928, 1990.

Frenkel, D., and B. Smit, *Understanding Molecular Simulation*, Academic Press, San Diego, 1996.

Furnish, M. D., and E. Ito, Experimental measurements of the hugoniot of stishovite, *Sandia Report*, *SAND95-2342*, 1995.

Garnero, E. J., and D. V. Helmberger, A very slow basal layer underlying large-scale low-velocity anomalies in the lower mantle beneath the Pacific-evidence from core phases , *Phys. Earth Planet. Int.*, *91*, 161–176, 1995.

Gathers, G. R., A. C. Mitchell, and N. C. Holmes, Hugoniot measurements in Vanadium using the LLNL two-state light-gas gun, in *Shock Compression of Condensed Matter*, edited by J. R. Asay, R. A. Graham, and G. K. Straub, pp. 89–90, Elsvier, 1983.

Grady, D. E., Shock deformation of brittle solids, *J. Geophys. Res.*, *85*, 913–924, 1980.

Grady, D. E., W. J. Murri, and G. R. Fowles, Quartz to stishovite: Wave propagation in the mixed phase region, *J. Geophys. Res.*, *79*, 332–338, 1974.

Grand, S. P., R. D. van der Hilst, and S. Widiyantoro, Global seismic tomography: A snapshot of convection in the Earth, *GSA Today*, *7*, 1–7, 1997.

Helffrich, G., and S. Sacks, Scatter and bias in differential PKP travel times and implications for mantle and core phenomena , *Geophys. Res. Lett.*, *21*, 2167–2170, 1994.

Helmberger, D. V., Numerical seismograms of long-period body waves from seventeen to forty degrees, *Bullet. Seism. Soc. Am.*, *63*, 633–646, 1973.

Helmberger, D. V., E. J. Garnero, and X.-M. Ding, Modeling two-dimensional structure at the core-mantle boundary, *J. Geophys. Res.*, *101*, 13,963–13,972, 1996.

Helmberger, D. V., S. Ni, X.-M. Ding, and J. Ritsema, Seismic evidence for ultralow-velocity zone beneath Africa and eastern Atlantic, *J. Geophys. Res.*, *105*, 23,865–23,878, 2000.

Hemley, R. J., A. P. Jephcoat, H.-K. Mao, L. C. Ming, and M. H. Manghnani, Pressure-induced amorphization of crystalline silica, *Nature*, *334*, 52–54, 1988.

Hemley, R. J., C. T. Prewitt, and K. J. Kingma, High-pressure behavior of silica, in *Silica : physical behavior, geochemistry and materials applications, Rev. Mineral. Vol 29*, edited by P. Heaney, C. Prewitt, and G. Gibbs, pp. 41–81, Mineral. Soc. Am., Washington, D.C., 1994.

Hemley, R. J., J. F. Shu, M. A. Carpenter, J. Hu, and K. J. Kingma, Solid/order parameter coupling in the ferroelastic transition in dense SiO_2 , *Solid State Commun.*, *114*, 527–532, 2000.

Herman, J. W., and H. E. Elsayed-Ali, Superheating of Pb(111), *Phys. Rev. Lett.*, *69*, 1228–1231, 1992.

Hill, R., The elastic behavior of a crystalline aggregate, *Proc. Phys. Soc. London, Ser. A*, *65*, 349–354, 1952.

Hixson, R. S., and J. N. Fritz, Shock compression of tungsten and molybdenum, *J. Appl. Phys.*, *71*, 1721–1728, 1992.

Hixson, R. S., D. A. Boness, J. W. Shaner, and J. A. Moriaty, Acoustic velocities and phase transitions in molyedenum under strong shock compression, *Phys. Rev. Lett.*, *62*, 637–640, 1989.

Holland, K. G., and T. J. Ahrens, Melting of $(Mg,Fe)_2SiO_4$ at the core-mantle boundary of the Earth, *Science*, *275*, 1623–1625, 1997.

Hoover, W. G., Canonical dynamics: equilibrium phase-space distributions, *Phys. Rev. A*, *31*, 1695–1697, 1985.

Hoover, W. G., and F. H. Ree, Melting transition and communal entropy for hard spheres, *J. Chem. Phys.*, *49*, 3609–3617, 1968.

Ishii, M., and J. Tromp, Normal-mode and free-air gravity constraints on lateral variations in velocity and density of Earth's mantle , *Science*, *285*, 1231–1234, 1999.

Ito, H., K. Kawada, and S.-I. Akimoto, Thermal expansion of stishovite, *Phys. Earth Planet. Int.*, *8*, 227–281, 1974.

Jackson, I., Melting of the silica isotypes SiO_2, BeF_2 and GeO_2 at elevated pressures, *Phys. Earth Planet. Int.*, *13*, 218–231, 1976.

Jackson, I., Melting of some alkali-earth and transition-metal fluorides and alkali fluoroberyllates at elevated pressures: a search for melting systematics, *Phys. Earth Planet. Int.*, *14*, 143–164, 1977.

Jeanloz, R., and R. Grover, Birch-Murnaghan and$U_S - u_p$ equations of state, in *Shock Compression of Condensed Matter*, edited by S. C. Schmidt and N. C. Holmes, pp. 69–72, Elsevier Sci., 1987.

Jin, Z. H., and K. Lu, Melting of surface-free bulk single crystals, *Phil. Mag. Lett.*, *78*, 29–35, 1998.

Jin, Z. H., P. Gumbsch, K. Lu, and E. Ma, Melting mechanisms at the limit of superheating, *Phys. Rev. Lett.*, *87*, 055,703, 2001.

Kaneshima, S., Mapping heterogeneity of the uppermost core using two pairs of core phases, *Geophys. Res. Lett.*, *23*, 3075–3078, 1996.

Kanzaki, M., Melting of silica up to 7 GPa, *J. Am. Ceram. Soc.*, *73*, 3706–3707, 1990.

Karki, B. B., L. Stixrude, and J. Crain, *Ab initio* elasticity of three high-pressure polymorphs of silica, *Geophys. Res. Lett.*, *24*, 3269–3272, 1997.

Karki, B. B., L. Stixrude, and R. M. Wentzcovich, High-pressure elastic properties of major materials of Earth's mantle from first principles, *Rev. Geophys.*, *39*, 507–534, 2001.

Kelton, K. F., Crystal nucleation in liquids and glasses, *Solid State Phys.*, *45*, 75–177, 1991.

Kimura, Y., Y. Qi, T. Çağın , and W. A. Goddard III , The quantum Sutton-Chen many-body potential for properties of *fcc* metals, *preprint*, 1998.

Kingma, K. J., R. E. Cohen, R. Hemley, and H.-K. Mao, Transformation of stishovite to a denser phase at lower-mantle pressures, *Nature*, *374*, 243–245, 1995.

Kleeman, J. D., and T. J. Ahrens, Shock-induced transition of quartz to stishovite, *J. Geophys. Res.*, *78*, 5954–5960, 1973.

Knittle, E., and R. Jeanloz, Earth's core-mantle boundary: Results of experiments at high pressures and temperature, *Science*, *251*, 1438–1443, 1991.

Kormer, S. B., Optical study of the characteristics of shock-compressed dielectrics, *Sov. Phys. Usp.*, *21*, 689–700, 1965.

Langenhorst, F., A. Deutsch, D. Stöffler, and U. Hornemann, Effect of temperature on shock metamorphism of single-crystal quartz, *Nature*, *356*, 507–509, 1992.

Leger, J. M., J. Haines, M. Schmidt, J. P. Petitet, A. Pereira, and J. A. H. deJornada, Discovery of hardest known oxide, *Nature*, *383*, 401, 1996.

Li, B. S., S. M. Rigden, and R. C. Liebermann, Elasticity of stishovite at high pressure, *Phys. Earth Planet. Int.*, *96*, 113–127, 1996.

Li, X.-D., and B. Romanowicz, Global mantle shear velocity model developed using nonlinear asymptotic coupling theory, *J. Geophys. Res.*, *101*, 22,245–22,272, 1996.

Lindemann, F. A., Über die berechnung molecularer eigeenfrequenzen, *Physik. Zeits.*, *11*, 609–612, 1910.

Liu, L.-G., and A. E. Ringwood, Synthesis of a perovskite-type polymorph of $CaSiO_3$, *Earth Planet. Sci. Lett.*, *28*, 209–211, 1975.

Liu, X.-F., W.-J. Su, and A. M. Dziewonski, Improved resolution of the lowermost mantle shear velocity structure obtained using SKS-S data, *EOS (Spring Suppl.)*, *75*, 232, 1994.

Lu, K., and Y. Li, Homogeneous nucleation catastrophe as kinetic stability limit for superheated crystal, *Phys. Rev. Lett.*, *80*, 4474–4477, 1998.

Luo, S. N., Thermodynamic and seismic phase changes, *preprint*, 2000.

Luo, S. N., and T. J. Ahrens, Superheating systematics of crystalline solids, *Appl. Phys. Lett.*, *82*, 1836–1838, 2003a.

Luo, S. N., and T. J. Ahrens, Application of shock-induced superheating to the melting of geophysically important minerals, *In press, Phys. Earth Planet. Interior*, 2003b.

Luo, S. N., S. Ni, and D. V. Helmberger, Evidence for a sharp lateral variation of velocity at the core-mantle boundary from multipathed PKPab, *Earth Planet. Sci. Lett.*, *189*, 155–164, 2001.

Luo, S. N., T. J. Ahrens, and P. D. Asimow, Polymorphism, superheating and amorphization of silica upon shock wave loading and release, *In press, J. Geophys. Res.*, 2002a.

Luo, S. N., T. J. Ahrens, T. Çağın , A. Strachan, and W. A. Goddard III , Superheating of crystalline solids: Theory, experiment, simulation, and application to static and dynamic high-pressure melting, *EOS Trans. AGU*, *83*, MR62B–1080, 2002b.

Luo, S. N., T. Cagin, A. Stranchan, W. A. Goddard, and T. J. Ahrens, Molecular dynamics modeling of stishovite, *Earth Planet. Sci. Lett.*, *202*, 147–157, 2002c.

Luo, S. N., J. L. Mosenfelder, P. D. Asimow, and T. J. Ahrens, Direct shock wave loading of stishovite to 235 GPa: Implications for perovskite stability relative to an oxide assemblage at lower mantle conditions, *Geophys. Res. Lett.*, *29*, 10.1029/2002GRL015,627, 2002d.

Luo, S. N., J. L. Mosenfelder, P. D. Asimow, and T. J. Ahrens, Stishovite and its implications in Geophysics: new results from shock-wave experiments and theoretical modeling, *Physics-Uspekhi*, *45*, 435–439, 2002e.

Luo, S. N., S. Ni, and D. V. Helmberger, Relationship of D” structure with the velocity variations near the inner-core boundary, *Geophys. Res. Lett.*, *29*, 10.1029/2002GRL015,627, 2002f.

Luo, S. N., T. J. Ahrens, T. Çağın , A. Strachan, W. A. Goddard III , and D. Swift, Maximum superheating and undercooling: systematics, molecular dynamics simulations and dynamic experiments, *Submitted to Phys. Rev. B*, 2003a.

Luo, S. N., O. Tschauner, J. L. Mosenfelder, P. D. Asimow, and T. J. Ahrens, New ultra-dense phase of silica from shock recovery experiments, *Joint AIRAPT 19th-41st EHPRG, International Conference on High Pressure Science and Technology,*, pp. July 7–11, 2003b.

Lyzenga, G. A., and T. J. Ahrens, The relation between the shock-induced free-surface velocity and the postshock specific volume of solids, *J. Appl. Phys.*, *49*, 201–204, 1978.

Lyzenga, G. A., T. J. Ahrens, and A. C. Mitchell, Shock temperatures of SiO_2 and their geophysical implications, *J. Geophys. Res.*, *88*, 2431–2444, 1983.

Malcolm, W. C., *NIST-JANAF Thermochemical Tables*, American Chemical Society and American Institute of Physics for the National Institute of Standards and Technology, 1998.

Mao, H.-K., G. Shen, and R. J. Shen, Multivariable dependence of Fe-Mg Partitioning in the lower mantle, *Science*, *278*, 2098–2100, 1997.

Marsh, S. P., *LASL Shock Hugoniot Data*, Univ. California Press, Berkeley, 1980.

Masters, G., S. Johnson, G. Laske, and H. Bolton, A shear velocity model of the mantle, *Phil. Trans. R. Soc. Lond.*, *354*, 1385–1411, 1996.

Masters, G., G. Laske, H. Bolton, and A. M. Dziewonski, Seismic tomography: Relative behavior of shear velocity, bulk sound speed, and compressional velocity in the mantle: implications for chemical and thermal structure, *Geophys. Monograph*, *117*, 63–82, 2000.

McQueeen, R. G., Shock waves in condensed matter: their properties and the equation of state of materials derived from them, in *High-pressure Equation of State: Theory and Applications*, edited by S. Eliezer and R. A. Ricci, pp. 101–216, North Holland, 1991.

McQueen, R. G., The velocity of sound behind strong shocks in SiO_2, in *Shock Compression of Condensed Matter*, edited by S. C. Schmidt, R. D. Dick, and D. G. Tasker, pp. 75–78, Elsevier Sci., 1992.

McSweeny, T. J., K. C. Creager, and R. T. Merrill, Depth extent of inner-core seismic anisotropy and implications for geomagnetism, *Phys. Earth Planet. Int.*, *101*, 131–156, 1997.

Meade, C., H.-K. Mao, and J. Hu, High-temperature phase transition and dissociation of (Mg,Fe)SiO_3 perovskite at lower mantle pressures, *Science*, *268*, 1743–1745, 1995.

Mishima, O., L. D. Calvert, and E. Whalley, Melting of Ice-I at 77-K and 10-Kbar - A new method of making amorphous solids, *Nature*, *310*, 393–395, 1984.

Mori, J., and D. V. Helmberger, Localized boundary layer below the mid-Pacific velocity anomaly identified from a PcP precursor, *J. Geophys. Res.*, *100*, 20,359–20,365, 1995.

Morris, J. R., C. Z. Wang, K. M. Ho, and C. T. Chan, Melting line of aluminum from simulations of coexisting phases, *Phys. Rev. B*, *49*, 3109–3115, 1994.

Morse, P. M., *Thermal Physics*, W. A. Benjamin, Inc., New York, 1964.

Motorin, V. I., and S. L. Musher, Kinetics of the volume melting: nucleation and superheating of metals, *J. Chem. Phys.*, *81*, 465–469, 1984.

Murphy, E. A., H. E. Elsayed-Ali, and J. W. Herman, Superheating of Bi(1000), *Phys. Rev. B*, *48*, 4921–4924, 1993.

Navrotsky, A., Thermochemistry of silica, in *Silica: physical behavior, geochemistry and materials applications, Rev. Mineral. Vol. 29*, edited by P. Heaney, C. Prewitt, and G. Gibbs, pp. 309–329, Mineral. Soc. Am., Washington, D.C., 1994.

Ni, S., and D. V. Helmberger, Horizontal transition from fast to slow structures at the core-mantle boundary; South Atlantic, *Earth Planet. Sci. Lett.*, *187*, 301–310, 2001.

Ni, S., X.-M. Ding, and D. V. Helmberger, Constructing synthetics from deep earth tomographic models, *Geophys. J. Int.*, *140*, 71–82, 2000.

Niu, F., and L. Wen, Hemispherical variations in seismic velocity at the top of the Earth's inner core, *Nature*, *410*, 1081–1084, 2001.

Ono, S., Phase boundary between rutile-type and $CaCl_2$-type in SiO_2 and GeO_2 determined by in situ X-ray observations, *Eos. Trans. AGU, Fall Meet. Suppl.*, *82*, F1157, 2001.

Oriani, R. A., The entropies of melting of metals, *J. Chem. Phys.*, *19*, 93–97, 1951.

Panero, W. R., L. B. Benedetti, and R. Jeanloz, Equation of state of stishovite and interpretation of SiO_2 shock compression data, *Preprint*, 2001.

Pankov, V. L., V. A. Kalinin, and A. A. Kalachnikov, Phase relations of the MgO-SiO_2 and FeO-SiO_2 systems and their implication for the properties and composition of the mantle, *Izvestiya, Physics of the Solid Earth*, *32*, 484–495, 1996.

Parrinello, M., and A. Rahman, Polymorphic transitions in single crystal: A new molecular dynamics method, *J. App. Phys.*, *52*, 7182–7190, 1981.

Phillpot, S. R., S. Yip, and D. Wolf, How do crystals melt?, *Computers in Physics*, *3*, 20–31, 1989.

Podurets, M. A., G. V. Simakov, and R. F. Trunin, On the phase equilibrium in shock-compressed quartz and on the kinetics of phase transitions, *Izv. Earth Phys.*, *7*, 3–11, 1976.

Podurets, M. A., G. V. Simokov, G. S. Telegin, and R. F. Trunin, Polymorphism of silica in shock waves and equation of state of coesite and stishovite, *Izvestiya, Physics of the Solid Earth*, *17*, 9–15, 1981.

Poirier, J. P., *Introduction to the Physics of the Earth's Interior*, Cambridge Univ. Press, 1991.

Porter, D. A., and K. E. Easterling, *Phase Transformations in Metals and Alloys*, Wokingham, 1981.

Rappe, A. K., and W. A. Goddard, Charge equilibration for molecular dynamics simulations, *J. Phys. Chem.*, *95*, 3358–3363, 1991.

Rethfeld, B., K. Sokolowski-Tinten, D. von der Linde, and S. I. Anisimow, Ultrafast thermal melting of laser-excited solids by homogeneous nucleation, *Phys. Rev. B*, *65*, 092,103, 2002.

Richards, M. A., and D. Engebreston, Large-scale mantle convection and the history of subduction, *Nature*, *355*, 437–440, 1992.

Richet, P., Superheating, melting, and vitrification upon decompression of high-pressure minerals, *Nature*, *331*, 56–58, 1988.

Richet, P., and Y. Bottinga, Rheology and configurational entropy of silicate melts, in *Structure, dynamics and properties of silicate melts, Rev. Mineral. Vol. 32*, edited by J. F. Stebbins, P. F. McMillan, and D. B. Dingwell, pp. 676–32, Mineral. Soc. Am., Washington, D.C., 1995.

Richet, P., and P. Gillet, Pressure-induced amorphization of minerals: a review, *Eur. J. Mineral.*, *9*, 907–933, 1997.

Ritsema, J., and H. van Heijst, Seismic imaging of structural heterogeneity in Earth's mantle: evidence for large-scale mantle flow, *Science Progress*, *83*, 243–259, 2000.

Ritsema, J., E. Garnero, and T. Lay, A strongly negative shear velocity gradient and lateral variability in the lower most mantle beneath the Pacific, *J. Geophys. Res.*, *102*, 20,395–20,411, 1997.

Ritsema, J., H. van Heijst, and J. H. Woodhouse, Complex shear velocity structure imaged beneath Africa and Iceland, *Science*, pp. 1925–1928, 1999.

Rivier, N., and D. M. Duffy, On the topological entropy of atomic liquids and the latent heat of fusion, *J. Phys. C*, *15*, 2867–2874, 1982.

Robertson, G. S., and J. H. Woodhouse, Evidence for proportionality of P and S heterogeneity in the lower mantle, *Geophys. J. Int.*, *123*, 85–116, 1995.

Robie, R. A., B. S. Hemingway, and J. R. Fisher, *Thermodynamic properties of minerals and related substances at 298.15 K and 1 bar (10^5 pascals) pressure and at higher temperatures*, U.S. Govt. Print. Off., 1978.

Rubie, D. C., Characterizing the sample environment in multianvil high-pressure experiments, *Phase Transitions*, *68*, 431–451, 1999.

Russell, S. A., and T. Lay, Small-scale lateral shear velocity and anisotropy heterogeneity near the core-mantle boundary beneath central Pacific imaged using broadband ScS waves, *J. Geophys. Res.*, *104*, 13,183–13,199, 1999.

Saxena, S. K., N. Chatterjee, Y. Fei, and G. Shen, *Thermodynamic Data on Oxides and Silicates: an Assessed Data Set Based on Thermochemistry and High Pressure Phase Equilibrium*, Springer-Verlag, 1993.

Saxena, S. K., L. Dubrovinsky, P. Lazor, Y. Cerenius, P. Haggkvist, M. Hanfland, and J. Hu, Stability of perovskite ($MgSiO_3$) in the Earth's mantle, *Science*, *274*, 1357–1359, 1996.

Saxena, S. K., L. S. Dubrovinsky, F. Tutti, and T. L. Bihan, Equation of state of $MgSiO_3$ with perovskite structure based on experimental measurement , *Am. Mineral.*, *84*, 226–232, 1999.

Serghiou, G., A. Zerr, and R. Boehler, (Mg,Fe)SiO_3-perovskite stability under lower mantle conditions, *Science*, *280*, 2093–2095, 1998.

Shaner, J. W., J. M. Brown, and R. G. McQueen, Melting of metals above 100 GPa, *Mat. Res. Soc. Symp. Proc.*, *22*, 137–141, 1984.

Shao, Y., and F. Spaepen, Undercooling of bulk liquid silicon in an oxide flux, *J. Appl. Phys.*, *79*, 2981–2985, 1996.

Sharma, S. M., and S. K. Sikka, Pressure induced amorphization of materials, *Prog. Mater. Sci.*, *40*, 1–77, 1996.

Shearer, P. M., and K. M. Toy, PKP(BC) versus PKP(DF) differential travel times and aspherical structure in the Earth's inner core, *J. Geophys. Res.*, *96*, 2233–2247, 1991.

Shen, G., and P. Lazor, Measurement of melting temperatures of some minerals under lower mantle pressures, *J. Geophys. Res.*, *100*, 17,699–17,713, 1995.

Shim, S.-H., T. S. Duffy, and G. Shen, Stability and structure of $MgSiO_3$ perovskite to 2300-kilometer depth in Earth's mantle, *Science*, *293*, 2437–2440, 2001.

Sidorin, I., M. Gurnis, D. V. Helmberger, and X.-M. Ding, Interpreting D" seismic structure using synthetic waveforms computed from dynamic models, *Earth Planet. Sci. Lett.*, *163*, 31–41, 1998.

Simha, N., and L. Truskinovsky, Shear-induced transformation toughening in ceramics, *Acta Metallurgica et Materialia*, *42*, 3827–3836, 1994.

Singh, H. B., and A. Holz, Stability limit of supercooled liquids, *Solid State Commun.*, *45*, 985–988, 1983.

Skinner, B. J., and J. J. Fahey, Observations on the inversion of stishovite to silica glass, *J. Geophys. Res.*, *68*, 5595–5604, 1963.

Song, X., and T. J. Ahrens, Pressure-temperature range of reactions between liquid iron in the outer core and mantle silicates, *Geophys. Res. Lett.*, *21*, 153–156, 1994.

Song, X.-D., and D. V. Helmberger, Effect of Velocity Structure in D" on PKP Phases, *Geophys. Res. Lett.*, *20*, 285–288, 1993.

Song, X.-D., and D. V. Helmberger, A P wave velocity of Earth's core, *J. Geophys. Res.*, *100*, 9805–9816, 1995.

Song, X.-D., and D. V. Helmberger, PKP differential travel times: Implications for 3-D lower Mantle, *Geophys. Res. Lett.*, *24*, 9817–9830, 1997.

Stacey, F. D., *Physics of the Earth*, 3rd ed., Brookfield Press, Kenmore, 1992.

Stacey, F. D., and R. D. Irvine, Theory of melting: Thermodynamic basis of Lindemann law, *Aus. J. Phys.*, *30*, 631–640, 1977.

Stishov, S. M., The thermodynamics of melting of simple substances, *Sov. Phys. Usp.*, *117*, 625–643, 1975.

Stöffler, D., Progressive metamorphism and classification of shocked and breciated crystalline rocks at impact craters, *J. Geophys. Res.*, *76*, 5541–5551, 1971.

Strachan, A., T. Çağın , and W. A. Goddard III , Phase diagram of MgO from density-function theory and molecular-dynamics simulation, *Phys. Rev. B*, *60*, 15,084–15,093, 1999.

Stranchan, A., T. Çağın , and W. A. Goddard III , Phase diagram of MgO from density-function theory and molecular dynamics simulation, *Phys. Rev. B*, *60*, 15,094–15,093, 1999.

Stranchan, A., T. Çağın , O. Gülseren, S. Mukherjee, R. E. Cohen, and W. A. Goddard III , First-principles force-field for metallic Tantalum, *preprint*, 2001.

Sumita, I., and P. Olson, A laboratory model for convection in Earth's core driven by a thermally heterogeneous mantle, *Science*, *286*, 1547–1549, 1999.

Sutton, A. P., and J. Chen, Logn-range Finnis-Sinclair potentials, *Phil. Mag. Lett.*, *61*, 139–146, 1990.

Swegle, J. W., Irreversible phase transitions and wave propagation in silicate geologic materials, *J. Appl. Phys.*, *68*, 1563–1579, 1990.

Tallon, J. L., A hierarchy of catastrophes as a succession of stability limits for the crystalline state, *Nature*, *342*, 658–660, 1989.

Tallon, J. L., and W. H. Robinson, A model-free elasticity theory of melting, *Phys. Lett.*, *87A*, 365–368, 1982.

Tan, E., and M. Gurnis, Slab dynamics at the core-mantle boundary, *AGU Fall meeting*, 2000.

Tan, H., and T. J. Ahrens, Shock-induced polymorphic transition in quartz, carbon, and boron nitride, *J. Appl. Phys.*, *67*, 217–224, 1990.

Thomas, C., The fine structure of the earth's deep mantle determined with scattered seismic core phases, *Ph.D. Thesis*, 1999.

Thompson, P. F., and P. J. Tackley, Generation of mega-plumes from the core-mantle boundary in a compressible mantle with temperature-dependent viscosity, *Geophys. Res. Lett.*, *25*, 1999–2002, 1998.

Trunin, R. F., G. V. Simakov, M. A. Podurets, B. N. Moiseev, and L. V. Popov, Dynamic compressibility of quartz and quarzite under high pressure, *Izv. Akad. Nauk USSR, Fiz. Zemli*, *1*, 13, 1971.

Turnbull, D., Kinetics of solidification of supercooled liquid mercury droplets, *J. Chem. Phys.*, *20*, 411–424, 1952.

Turnbull, D., Phase Changes, *Solid State Phys.*, *3*, 225–306, 1956.

Uhlmann, D. R., On the internal nucleation of melting, *J. Non-cryst. Solids*, *41*, 347–357, 1980.

Vidale, J., and M. Hedlin, Evidence for partial melt at the core-mantle boundary north Tonga from the strong scattering of seismic waves, *Nature*, *391*, 682–685, 1998.

Vinet, P., J. H. Rose, J. Ferrante, and J. R. Smith, Compressibility of solids, *J. Geophys. Res.*, *92*, 9319–9325, 1989.

Wackerle, J., Shock-wave compression of quartz, *J. Appl. Phys.*, *33*, 922–937, 1962.

Walton, A. G., Nucleation in liquids and solutions, in *Nucleation*, edited by A. Zettlemoyer, pp. 225–307, Marcel Dekker, Inc., 1969.

Wang, J. H., J. Li, S. Yip, D. Wolf, and S. R. Phillpot, Unifying two criteria of Born: Elastic instability and melting of homogeneous crystals, *Physica A*, *240*, 396–403, 1997.

Watanabe, H., Thermochemical properties of synthetic high-pressure compounds relevant to the Earth's mantle, in *High-pressure Research in Geophysics*, edited by S. Akimoto and M. H. Manghnani, pp. 441–464, 1982.

Watt, J. P., T. J. Shankland, and N. Mao, Uniformity of mantle composition, *Geology*, *3*, 92–97, 1975.

Weidner, D., J. D. Bass, A. E. Ringwood, and W. Sinclair, The single-crystal elastic moduli of stishovite, *J. Geophys. Res.*, *87*, 4740–4746, 1982.

Weinberg, M. C., On the location of the maximum homogeneous crystal nucleation teperature, *J. Non-cryst. Solids*, *98*, 98–113, 1986.

Wen, L. X., and D. V. Helmberger, A two-dimensional P-SV hybrid method and its application to modeling localized structures near the core-mantle boundary, *J. Geophys. Res.*, *103*, 17,901–17,918, 1998a.

Wen, L. X., and D. V. Helmberger, Ultra-low velocity zones near the core-mantle boundary from broadband PKP precursors, *Science*, *279*, 1701–1703, 1998b.

Williams, Q., R. Jeanloz, J. Bass, B. Svendsen, and T. J. Ahrens, The melting curve of iron to 250 gigapascals: a constraint on the temperature at Earth's center, *Science*, *236*, 181–182, 1987.

Williamson, S., G. Mourou, and J. C. M. Li, Time-resolved laser-induced phase transition is aluminum, *Phys. Rev. Lett.*, *52*, 2364–2367, 1984.

Wysession, M. E., Large-scale structure at the core-mantle boundary from core-diffracted phases, *Nature*, *382*, 244–248, 1996.

Wysession, M. E., T. Lay, J. Revenaugh, Q. Williams, E. J. Garnero, R. Jeanloz, and L. H. Kellogg, The D" discontinuities and its implications, in *The Core-Mantle*

Boundary Region, edited by M. Gurnis, M. E. Gurnis, E. Knittle, and B. A. Buffet, pp. 273–298, AGU, Washington, D. C., 1998.

Yoo, C. S., N. C. Holmes, M. Ross, D. J. Webb, and C. Pike, Shock temperatures and melting of iron at Earth core conditions, *Phys. Rev. Lett.*, *70*, 3931–3934, 1993.

Zel'dovich, Y. B., and Y. P. Raizer, *Physics of Shock Waves and High-temperature Hydrodynamic Phenomena*, Dover Publications, Mineola, New York, 2002.

Zhang, J., R. C. Liebermann, T. Gasparik, C. T. Herzberg, and Y. Fei, Melting and subsolidus relations of SiO_2 at 9-14 GPa, *J. Geophys. Res.*, *98*, 19,785–19,793, 1993.

Zhang, S., and D. A. Yuen, Various influences on plumes and dynamics in time-dependent, compressible mantle convection in 3-D spherical shell, *Phys. Earth Planet. Int.*, *94*, 241–267, 1997.

Zhugin, Y. N., K. K. Krupnikov, N. P. Voloshin, and Y. A. Shoidin, Phase transformations in quartz, induced by shock waves from underground nuclear explosions, *Izv., Phys. Solid Earth*, *35*, 478–483, 1999.